



JUSTUS-LIEBIG-
UNIVERSITÄT
GIESSEN

MASTER-THESIS

**Search for new bottomonium(-like) states
in $e^+e^- \rightarrow B^{(*)}\bar{B}^{(*)}(\pi)(\pi)$
at the BELLE experiment**

Suche nach neuen Bottomonium(-artigen) Zuständen
in $e^+e^- \rightarrow B^{(*)}\bar{B}^{(*)}(\pi)(\pi)$ am BELLE-Experiment

MARCEL WERNER

November 22, 2010

II. PHYSIKALISCHES INSTITUT
Arbeitsgruppe Prof. Dr. Wolfgang Kühn

ABSTRACT

Since many theoretically predicted bottomonium states have not been experimentally discovered yet, a search for new bottomonium(-like) states in $e^+e^- \rightarrow B^{(*)}\bar{B}^{(*)}(\pi)(\pi)$ reactions is accomplished. An inclusive dilepton approach is used for tagging B mesons from energy scan data between $\Upsilon(4S)$ and $\Upsilon(6S)$ collected at BELLE. Additional pions are considered to enhance the contributions of states with quantum numbers $J^{PC} = 1^{+\pm}$. The $\Upsilon(5S)$ lineshape parameters are determined to $\phi_{\Upsilon 5S} = -1.512 \pm 0.066$, $\mu_{\Upsilon 5S} = 10.838 \pm 0.067$ GeV and $\Gamma_{\Upsilon 5S} = 0.106 \pm 0.0087$ GeV. First evidence for B production in $\Upsilon(6S)$ decays has been found. The consideration of additional pions brought no evidence for new $J^{PC} = 1^{+\pm}$ bottomonium(-like) states between the $\Upsilon(4S)$ and the $\Upsilon(6S)$ resonance. The branching fraction $\mathcal{B}(\Upsilon(5S) \rightarrow X_b \pi^0 (\gamma) \rightarrow B^{(*)0} \bar{B}^{(*)0} \pi^0 (\gamma))$ was estimated to be smaller than 5.05 ± 0.14 % at 90% confidence level.

Contents

Introduction	9
1. Physics Principles	11
1.1. The Standard Model	11
1.2. Heavy Quark-Antiquark Potentials and Bottomonium Eigenstates . . .	14
1.2.1. Schroedinger Equation	14
1.2.2. The Cornell Potential	15
1.2.3. Perturbative QCD and Breit Interaction	16
1.2.4. The Spin Interactions	19
1.2.4.1. Spin-Spin Coefficient	20
1.2.4.2. Spin-Orbit Coefficient	20
1.2.4.3. Tensor Coefficient	21
1.2.5. From Potential To Mass	21
1.2.6. Bottomonium Wavefunctions and Eigenstates	22
1.3. The $X(3872)$ -Resonance	27
1.3.1. Quantum numbers of the $X(3872)$	27
1.3.2. Interpretations of the $X(3872)$	29
1.3.2.1. Charmonium Interpretation	29
1.3.2.2. Charm Meson Molecule Interpretation	31
1.3.2.3. Other Interpretations	31
1.4. Searching for a bottom counterpart of $X(3872)$	32
2. Experimental Setup	34
2.1. Basic Principles	34
2.2. Luminosity	36
2.3. KEKB Accelerator	36

2.4. BELLE detector	38
2.4.1. Silicon Vertex Detector	39
2.4.2. Central Drift Chamber	39
2.4.3. Aerogel Cherenkov Counter	40
2.4.4. Time Of Flight Measurement	40
2.4.5. Electromagnetic Calorimeter	41
2.4.6. The K_L^0 and μ Detection System	41
3. Analysis and Results	43
3.1. Energy Scan Data	43
3.2. Inclusive Dilepton Analysis	43
3.2.1. Dilepton Event Selection	49
3.2.2. Results on Dilepton Production in Dependence of \sqrt{s}	52
3.3. Analysis of $B^{(*)}\bar{B}^{(*)}\pi^0$ Events	58
3.3.1. π^0 Selection	59
3.3.2. Results on $B^{(*)}\bar{B}^{(*)}\pi^0$ events	62
3.4. $B^{(*)}\bar{B}^{(*)}\pi^+\pi^-$ events	71
4. Summary and Conclusion	73
5. Deutsche Zusammenfassung	75
A. Monte Carlo Data	78
A.1. Efficiencies of the Momentum Cuts	78
A.2. J/ψ lepton momenta	78
A.3. Determination of the Correction Factors	82
B. Energy Scan Datasets	85
C. Mathematics	86
C.1. Kinematics	86
C.2. Calculation Of The Complex Fit Function	87
C.3. π^0 Recoilmass Background Fit Using Higher Order Polynomials	88
Acknowledgements	89
List of Figures	93
List of Tables	95
Bibliography	96

Note:

As common in the field of high energy physics all equations are presented in natural units

$$\hbar = c = 1 \quad .$$

This implies that all masses, energies and momenta are measured in GeV.

Introduction

The discovery of the charm-quark [1][2] with a mass of approximately 1.2 GeV in November 1974 at the SLAC accelerator led to a new era in particle physics: it established the quark model and non-Abelian gauge field theories, which are the fundament of the actual understanding of particle physics. A few years later, the next heavier quark was discovered: the bottom-quark [3] with a mass of approximately 4.8 GeV. Since then the physics of charm and bottom quarks has aroused interest of both theoreticians and experimentalists and much effort was put in the investigation of the underlying flavor physics. With the installation and commissioning of two B-factories in the 1990s, namely BaBar at the PEP-II collider at SLAC laboratory in California and BELLE at the KEKB collider in Tsukuba, Japan, the investigation of C and B physics reached a climax and the research of very rare events and strongly suppressed decays became possible. The B-factories have yielded a rich harvest of results, including the first observation of CP violation outside the Kaon-system and measurements of the Cabibbo-Kobayashi-Maskawa (CKM) parameters, which contain information on the strength of flavor-changing weak decays. Overconstraining measurements of the unitarity triangle, which is determined by the CKM parameters, may reveal physics beyond the Standard Model.

In this thesis a search for new bottomonium(-like) states in the $e^+e^- \rightarrow B^{(*)}\bar{B}^{(*)}(\pi)(\pi)$ channel with an inclusive approach is presented. Energyscan data between $\Upsilon(4S)$ and $\Upsilon(6S)$, which was taken between 6th of October and 17th of December 2007 at the BELLE detector, and $\Upsilon(1S)$, $\Upsilon(2S)$, $\Upsilon(3S)$, $\Upsilon(4S)$, $\Upsilon(5S)$ data from BELLE was used as the basis of this analysis. One main emphasis is the search for a bottom counterpart of the recently discovered $X(3872)$ resonance with quantum numbers $J^{PC} = 1^{++}$ which is speculated to be a hadronic molecule (see section 1.3).

1

Physics Principles

Three quarks for Muster Mark!
Sure he has not got much of a bark
And sure any he has it's all beside
the mark.

Finnegans Wake
James Joyce

The aim of hadron and particle physics is to understand nature on the level of its fundamental constituents, the elementary particles, which are (as far as we know yet) the fermions (spin 1/2 particles) and the bosons (spin 1 particles). The fundamental fermions are the quarks and the leptons, of which each has its antiparticle¹ and together with the group of bosons, which mediate the interactions, they form the basis for all known matter in the universe.

1.1. The Standard Model

Oh gravity, thou art a heartless
bitch.

Sheldon Cooper, PhD [4]

The Standard Model (SM) is a theoretical framework which describes the elementary particles and their strong, weak, and electromagnetic interactions in terms of “gauge-field theories”, which possess invariance under certain transformations. These transformations go along with the exchange of gauge bosons, which are related to the

¹Because antineutrinos and neutrinos are neutral particles it is possible that they are actually the same particle. Particles which have this property are known as Majorana particles. If neutrinos are indeed Majorana particles then the neutrinoless double beta decay process is allowed. Several experiments have been proposed to search for this process.

	1st generation	2nd generation	3rd generation	electromag. charge	color
Leptons	e	μ	τ	-1	-
	ν_e	ν_μ	ν_τ	0	-
Quarks	u	c	t	+2/3	r, g, b
	d	s	b	-1/3	r, g, b

Table 1.1.: Fundamental fermions in the SM

gauge symmetries of the fields. The SM brings all these three interactions into one big formalism with which many aspects of the complex matter of hadron and particle physics can be described. The standard model of physics is based on a combination of three internal symmetries

$$\underbrace{U(1)}_{\text{electromagnetic force}} \times \underbrace{SU(2)}_{\text{weak force}} \times \underbrace{SU(3)}_{\text{strong force}} \quad (1.1.1)$$

relating to the mathematical symmetry groups which describe the interactions.

In the SM there are six types of quarks, known as flavors *up* (u), *down* (d), *strange* (s), *charm* (c), *bottom* (b) and *top* (t) and six types of leptons ($e, \nu_e, \mu, \nu_\mu, \tau, \nu_\tau$) which are grouped into three generations of doublets (see Tab. 1.1).

The electromagnetic interaction is described by the theory of quantum electrodynamics (QED), where massless photons (γ) which couple to electric charge, mediate the interaction. Its range is infinite, but since it can be attractive and repulsive its impact is negligible on very large scales as in cosmology. QED is the first theory where full agreement between quantum mechanics and special relativity is achieved. Its extremely accurate predictions of quantities like the anomalous magnetic moment of the electron and the Lamb shift of the energy levels of hydrogen made QED the best tested theory in science history.

The weak interaction couples to all left-handed leptons and quarks and goes along with the exchange of massive W^\pm ($m_{W^\pm} = 80.4$ GeV) and Z bosons ($m_{Z^0} = 91.2$ GeV). Because quantum field theories only allow massless gauge bosons, the so-called Higgs mechanism was introduced to explain this feature of the weak interaction, but it is not yet experimentally proven. The weak interaction is unique in a number of respects: it can change the quark flavor and it violates parity symmetry, since it almost exclusively couples to left-handed particles. CP violation, the violation of CP symmetry under combined parity and charge conjugation, is also exclusively observed in weak processes. The weak interaction is also very short ranged ($\sim 10^{-18}$ m) because of its heavy gauge bosons. Weak decays are therefore much slower than strong or electromagnetic decays and appear much weaker than electromagnetic decays, although the coupling constants of both interactions are approximately alike. It is due to this “weakness” of the weak

interaction that the neutron, which can only decay weakly, is the unstable subatomic particle with the longest known mean life which is approximately 15 minutes.

The strong interaction is characterized by its color-charge and can be described by the exchange of colored gluons (g) which couple only to colored objects, which are the gluons themselves and the quarks. It is this selfcoupling of the gluons which makes the theory of the strong interaction (QCD) so complicated and hardly calculatable. The range of the strong interaction is limited to scales of nuclei ($\sim 10^{-15}\text{m}$). Particles that feel the strong interaction are called hadrons. QCD can explain why isolated quarks and gluons have never been directly observed in experiments, since it predicts that an isolated quark or gluon has infinite energy. Combinations of quarks, antiquarks and gluons can have finite energy only if their overall color charge is neutral. A combination of a quark and an antiquark is called a meson. A combination of three quarks (antiquarks) is called a baryon (antibaryon). However, one could also think of more exotic combinations: glueballs with constituents ggg , hybrid mesons with constituents $q\bar{q}g$, tetraquarks with constituents $qq\bar{q}\bar{q}$ and pentaquarks with constituents $qqq\bar{q}q$. Hadronic molecules, with two color neutral mesons, which are bound by a color force between its colored constituents, would also be allowed by QCD. Baryonic molecules exist in many forms, since any nucleus with two or more baryons can be called a baryonic molecule.

Another remarkable unique feature of QCD is that the potential between two colored constituents rises linearly with increasing distance of the constituents (Fig. 1.1). If the distance between colored constituents is very small they almost behave as free particles with no interaction in between, this is known as the so-called asymptotic freedom of QCD.

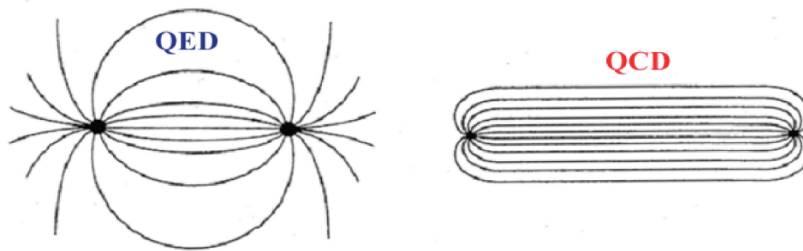


Figure 1.1.: Difference between QED and QCD forces: The QED force between two charged particles decreases with increasing distance whereas the QCD force between two colored particles remains constant with increasing distance.

Gravity is negligible regarding microscopic scales but it is the dominating force on large scales, since its range is infinite and it is always attractive. Unfortunately there is no appropriate quantum field theory which describes the gravitational interactions of matter yet, since standard techniques of quantum field theories are not applicable due to gravity's weakness. Hence the SM can not be the ultimate theory of nature.

The best theoretical description of gravity is Einstein's classical theory of general relativity, which does not include any quantum effects. Several promising theories like loop quantum gravity or string theory try to solve this problem, but it is not clear yet, if their predictions are experimentally provable.

1.2. Heavy Quark-Antiquark Potentials and Bottomonium Eigenstates

The discoveries of the heavy c and b quarks led to many theoretical approaches in order to give detailed descriptions of heavy quark-antiquark spectra. One of the more phenomenological ways to describe the experimental data is to solve the nonrelativistic Schroedinger equation for these quark-antiquark states with an appropriate potential. Since the characteristic QCD-scale $\Lambda_{\text{QCD}} \approx 0.2$ GeV is small compared to the charm and bottom quark masses, a systematic expansion in powers of $1/m_q$ is possible and the nonrelativistic description with the Schroedinger equation gives acceptable results, at least for states below the $D\bar{D}^- / B\bar{B}^-$ threshold respectively.

1.2.1. Schroedinger Equation

Where did we get that from?
 Nowhere. It's not possible to derive it from anything you know. It came out of the mind of Schroedinger, invented in his struggle to find an understanding of the experimental observations of the real world.

Richard P. Feynman [5]

In order to calculate the wave functions and eigenstates of the quarkonium states, one starts with the time-independent Schroedinger equation with a central potential and a Hamiltonian of the form

$$H = \frac{\vec{p}_1^2}{2m_1} + \frac{\vec{p}_2^2}{2m_2} + V(|\vec{r}_1 - \vec{r}_2|) \quad , \quad (1.2.1)$$

which can be separated into center-of-mass (CM) motion and relative motion via

$$\begin{aligned} H_{\text{CM}} &= \frac{\vec{P}^2}{2M} \quad , & H_{\text{rel}} &= \frac{\vec{p}^2}{2\mu} + V(|\vec{r}|) \quad , \\ \vec{P} &= \vec{p}_1 + \vec{p}_2 \quad , & \vec{p} &= \frac{m_2\vec{p}_1 - m_1\vec{p}_2}{m_1 + m_2} \quad , \\ \vec{R} &= \frac{m_1\vec{r}_1 + m_2\vec{r}_2}{m_1 + m_2} \quad , & \vec{r} &= \vec{r}_1 - \vec{r}_2 \quad , \\ M &= m_1 + m_2 \quad , & \mu &= \frac{m_1m_2}{m_1 + m_2} \end{aligned} \quad (1.2.2)$$

leading to

$$H = \underbrace{\frac{\vec{P}^2}{2M}}_{H_{CM}} + \underbrace{\frac{\vec{p}^2}{2\mu} + V(|\vec{r}|)}_{H_{rel}} . \quad (1.2.3)$$

With the correspondence principle

$$\vec{p} \rightarrow -i\vec{\nabla} \quad (1.2.4)$$

the resulting Schroedinger equation in the CM-frame is

$$\left[-\frac{\Delta}{2\mu} + V(r) \right] \Psi(\vec{r}) = E\Psi(\vec{r}) . \quad (1.2.5)$$

Assuming that the potential is radially symmetric, the wave function can be separated into radius dependent and angular dependent terms via a product ansatz of the form

$$\Psi(r, \theta, \varphi) = R_{kl}(r) \cdot Y_l^m(\theta, \varphi) . \quad (1.2.6)$$

This yields in the radial differential equation

$$\left[-\frac{1}{2\mu} \left(\frac{\partial^2}{\partial r^2} + \frac{2}{r} \frac{\partial}{\partial r} \right) + \frac{l(l+1)}{2\mu r^2} + V(r) \right] R_{kl}(r) = E_{kl} R_{kl}(r) . \quad (1.2.7)$$

The equation can be simplified by introducing the reduced radial wave function

$$u_{kl}(r) = r \cdot R_{kl}(r) \quad (1.2.8)$$

and one arrives at

$$\left[-\frac{1}{2\mu} \frac{d}{dr^2} + \frac{l(l+1)}{2\mu r^2} + V(r) \right] u_{kl}(r) = E_{kl} u_{kl}(r) . \quad (1.2.9)$$

For physically reasonable statements the wave functions have to be normalized with the condition

$$\int d^3r |\Psi(\vec{r})|^2 = \int d\Omega \, dr \, r^2 [R_{kl}(r)]^2 |Y_l^m(\theta, \varphi)|^2 = 1 .$$

Since the $d\Omega$ -integral over $|Y_l^m(\theta, \varphi)|^2$ is already normalized to 1, one arrives at

$$\int dr \, r^2 [R_{kl}(r)]^2 = \int dr [u_{kl}(r)]^2 = 1 . \quad (1.2.10)$$

1.2.2. The Cornell Potential

There are several ways to introduce a potential-model in order to describe quarkonium bound states: one can either use a purely phenomenological potential with various parameters, which are then optimized to fit the data or one can use perturbative QCD as a guide for the short range part of the potential and use a phenomenological long range part to account for confinement.

The Cornell potential is derived via the second method. It is a Coulomb-plus-Linear potential of the form

$$V(r)_{\text{Cornell}} = \underbrace{-\frac{4\alpha_s}{3r}}_{V_{\text{pert.}}} + \underbrace{\sigma r}_{V_{\text{conf.}}} . \quad (1.2.11)$$

Since no way has been found to derive the quark confinement from basic QCD rules yet, the confinement term has to be added by hand. At least this linear term comes from lattice gauge theory calculations, which observe a linear behavior of the potential for large r values. The derivation of the perturbative Coulomb-like term and the spin-dependencies is summarized in the following section, for details I refer to [6].

1.2.3. Perturbative QCD and Breit Interaction

As noticed above, the short range part of the potential can be dealt with via perturbative QCD. The Breit interaction had first been introduced by Gregory Breit [7][8][9] in order to describe electron-electron scattering. The according potential includes a leading Coulomb term, relativistic corrections arising from the one-photon exchange process and an expansion of the propagator, leading to retardation. Likewise we can rederive the Breit interaction for the quark-antiquark scattering process

$$q_i(p_A, s_A) + \bar{q}_j(p_B, s_B) \rightarrow q_k(p'_A, s'_A) + \bar{q}_l(p'_B, s'_B) \quad (1.2.12)$$

with q_x (\bar{q}_x) representing the properties of the quarks (antiquarks) with four-momenta p_x, p'_x and spins s_x, s'_x as indicated, and $i, j, k, l = 1, 2, 3$ being color indices. In this case the potential arising from one-gluon exchange, including retardation corrections, is equivalent to the Breit interaction. At lowest order perturbative QCD the scattering process in Eq. (1.2.12) is described by two Feynman-diagrams, a s-channel diagram (Fig. 1.2) and a t-channel-diagram (Fig. 1.3).

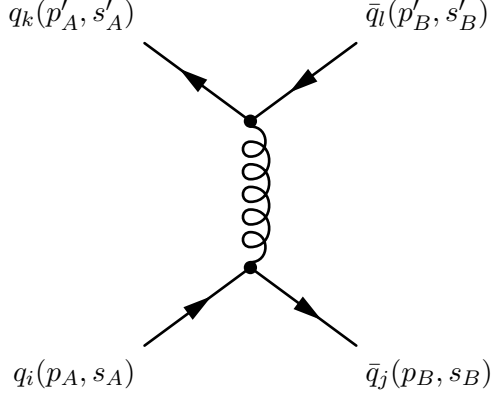


Figure 1.2.: One-gluon exchange s-channel diagram for $q\bar{q}$ -annihilation

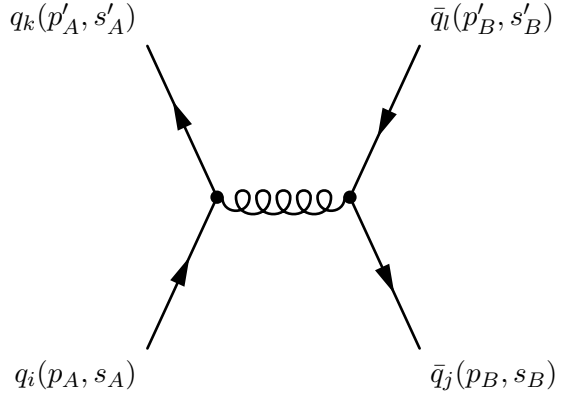


Figure 1.3.: One-gluon exchange t-channel diagram for $q\bar{q}$ -scattering

With our knowledge that mesons are color neutral objects, the color wave function

$$|\text{Meson}\rangle \propto \frac{1}{\sqrt{3}} \sum_{i=1}^3 |\bar{q}_i q_i\rangle \quad (1.2.13)$$

for Eq. (1.2.12) results in the conditions

$$\frac{1}{\sqrt{3}}\delta_{ij} \quad \text{and} \quad \frac{1}{\sqrt{3}}\delta_{kl} \quad . \quad (1.2.14)$$

The net-color of the gluons forbids the s-channel quark antiquark annihilation process from Fig. 1.2, since the annihilating meson has to be colorless. That means that the s-channel contribution from Fig. 1.2 vanishes and the only thing to be dealt with is the t-channel process.

Employing Feynman rules the t-channel amplitude in Feynman gauge is given by

$$\begin{aligned} \mathcal{M}_{fi} &= \left[\bar{u}(p'_A, s'_A) \underbrace{\left(ig\gamma^\mu \frac{\lambda_{ki}^a}{2} \right)}_{\text{vertex}} u(p_A, s_A) \right] \underbrace{\frac{g_{\mu\nu}}{q^2 + i\epsilon}}_{\text{propagator}} \left[\bar{v}(p_B, s_B) \underbrace{\left(ig\gamma^\nu \frac{\lambda_{jl}^a}{2} \right)}_{\text{vertex}} v(p'_B, s'_B) \right] \\ &= -\frac{g^2}{q^2 + i\epsilon} \frac{\lambda_{ki}^a}{2} \frac{\lambda_{jl}^a}{2} \bar{u}(p'_A, s'_A) \gamma_\mu u(p_A, s_A) \bar{v}(p_B, s_B) \gamma^\mu v(p'_B, s'_B) \quad , \quad (1.2.15) \end{aligned}$$

with $q^2 = (p_A - p'_A)^2 = (p_B - p'_B)^2$.

Using the conditions for colorless initial and final states from Eq. (1.2.14) yields the factor

$$\frac{1}{\sqrt{3}} \sum_{i,j=1}^3 \delta_{ij} \frac{1}{\sqrt{3}} \sum_{k,l=1}^3 \delta_{kl} \sum_{a=1}^8 \frac{\lambda_{ki}^a}{2} \frac{\lambda_{lk}^a}{2} = \frac{1}{12} \sum_{i,k=1}^3 \sum_{a=1}^8 \lambda_{ki}^a \lambda_{ik}^a = \frac{1}{12} \sum_{a=1}^8 \text{tr} [(\lambda^a)^2] = \frac{4}{3} \quad (1.2.16)$$

and the process Eq. (1.2.12) leads to the amplitude

$$\mathcal{M}_{fi} = \frac{4}{3} \frac{g^2}{q^2 + i\epsilon} \bar{u}(p'_A, s'_A) \gamma_\mu u(p_A, s_A) \bar{v}(p_B, s_B) \gamma^\mu v(p'_B, s'_B) \quad (1.2.17)$$

The normalized Dirac spinors for an arbitrary frame of reference are given by

$$\begin{aligned} u(p_A, s_A) &= \sqrt{\frac{E_A + m_A}{2m_A}} \begin{pmatrix} \chi_{s_A} \\ \frac{\vec{\sigma} \cdot \vec{p}_A}{E_A + m_A} \chi_{s_A} \end{pmatrix}, \\ \bar{u}(p'_A, s'_A) &= \sqrt{\frac{E'_A + m_A}{2m_A}} \left(\chi_{s'_A}^\dagger, -\chi_{s'_A}^\dagger \frac{\vec{\sigma} \cdot \vec{p}'_A}{E'_A + m_A} \right), \\ v(p'_B, s'_B) &= \sqrt{\frac{E'_B + m_B}{2m_B}} \begin{pmatrix} \frac{\vec{\sigma} \cdot \vec{p}'_B}{E'_B + m_B} \chi_{s'_B}^c \\ \chi_{s'_B}^c \end{pmatrix}, \\ \bar{v}(p_B, s_B) &= \sqrt{\frac{E_B + m_B}{2m_B}} \left(\chi_{s_B}^c \dagger, \frac{\vec{\sigma} \cdot \vec{p}_B}{E_B + m_B}, -\chi_{s_B}^c \dagger \right), \end{aligned} \quad (1.2.18)$$

with quark masses m_x and energies $E_x = \sqrt{\vec{p}_x^2 + m_x^2}$.

Calculating the Dirac currents is nontrivial and lengthy, so only the final expression for the amplitude is given here, for more details see [6].

$$\begin{aligned} \mathcal{M}_{fi} &= \frac{4}{3} \frac{g^2}{q^2 + i\epsilon} (\mathcal{A} + \mathcal{B}), \\ \mathcal{A} &= \delta_{s_1 s'_1} \delta_{s_2 s'_2} \left(1 + \frac{2\vec{p}_1^2 - 2i\vec{s}_1 \cdot (\vec{q} \times \vec{p}_1^2)}{4m_1^2} + \frac{2\vec{p}_2^2 + 2i\vec{s}_2 \cdot (\vec{q} \times \vec{p}_2^2)}{4m_2^2} \right) + \mathcal{O}\left(\frac{1}{m_i^3}\right), \\ \mathcal{B} &= \frac{\delta_{s_1 s'_1} \delta_{s_2 s'_2}}{4m_1 m_2} \left(-4\vec{p}_1 \cdot \vec{p}_2 + 4i\vec{s}_1 \cdot (\vec{q} \times \vec{p}_2) - 4i\vec{s}_2 \cdot (\vec{q} \times \vec{p}_1) \right. \\ &\quad \left. - 4\vec{q}^2 (\vec{s}_1 \cdot \vec{s}_2) + 4(\vec{q} \cdot \vec{s}_1)(\vec{q} \cdot \vec{s}_2) \right) + \mathcal{O}\left(\frac{1}{m_i^3}\right). \end{aligned} \quad (1.2.19)$$

To find the potential corresponding to \mathcal{M}_{fi} , we have to relate the nonrelativistic cross section from Schroedinger theory

$$d\sigma_{\text{non relat.}} = \frac{d^3 p'_1 d^3 p'_2}{(2\pi)^3 (2\pi)^2} (2\pi)^4 \delta^{(4)} \left(\sum_f p_f - \sum_i p_i \right) \frac{|f_B|^2}{|v_{\text{relative}}|}, \quad (1.2.20)$$

which is related to the Born scattering amplitude f_B , with the relativistic cross section

$$d\sigma_{\text{relat.}} = d^3 p'_1 d^3 p'_2 \frac{m_1^2 m_2^2}{E_A E'_A E_B E'_B} (2\pi)^4 \delta^{(4)} \left(\sum_f p_f - \sum_i p_i \right) \frac{|\mathcal{M}_{fi}|^2}{|v_{\text{relative}}|}. \quad (1.2.21)$$

Because the Born scattering amplitude is equal to the Fourier transform of the potential,

$$f_B = \int \frac{d^3 r}{(2\pi)^3} \exp[-i\vec{p}' \cdot \vec{r}] V(\vec{r}) \exp[i\vec{p} \cdot \vec{r}], \quad (1.2.22)$$

the relation between potential and amplitude reads

$$\begin{aligned} \frac{1}{(2\pi)^3} \tilde{V}(\vec{q}; \vec{p}_1, \vec{p}_2) &= \pm \frac{m_1 m_2}{\sqrt{E_A} \sqrt{E_B} \sqrt{E'_A} \sqrt{E'_B}} \mathcal{M}_{fi} \\ &= \pm \left(1 - \frac{\vec{p}_1^2}{2m_1^2} - \frac{\vec{q}^2}{8m_1^2} - \frac{\vec{p}_2^2}{2m_2^2} - \frac{\vec{q}^2}{8m_2^2} + \mathcal{O}\left(\frac{1}{m_i^3}\right) \right) \mathcal{M}_{fi} . \end{aligned} \quad (1.2.23)$$

After the expansion

$$\frac{1}{q^2} \approx -\frac{1}{\vec{q}^2} - \frac{1}{\vec{q}^4} \frac{(\vec{p}_1 \cdot \vec{q})(\vec{p}_2 \cdot \vec{q})}{m_1 m_2} + \mathcal{O}\left(\frac{1}{m^3}\right) \quad (1.2.24)$$

of the four-vector q in the propagator in order to obtain a nonrelativistic potential, some further calculations and a Fourier transformation back into space coordinates, one finally obtains the Breit interaction potential for quark-antiquark scattering

$$\begin{aligned} V^{\text{Breit}}(\vec{r}; \vec{p}_1, \vec{p}_2) &= -\frac{4\alpha_s}{3r} + \frac{2\pi\alpha_s}{3} \delta^{(3)}(\vec{r}) \left(\frac{1}{m_1^2} + \frac{1}{m_2^2} \right) + \frac{2\alpha_s}{3m_1 m_2} \left[\frac{\vec{p}_1 \cdot \vec{p}_2}{r} + \frac{(\vec{r} \cdot \vec{p}_1)(\vec{r} \cdot \vec{p}_2)}{r^3} \right] \\ &+ \frac{4\alpha_s}{3m_1 m_2} \left[\frac{8\pi}{3} \delta^{(3)}(\vec{r}) (\vec{s}_1 \cdot \vec{s}_2) + \frac{3(\vec{s}_1 \cdot \hat{r})(\vec{s}_2 \cdot \hat{r}) - \vec{s}_1 \cdot \vec{s}_2}{r^3} \right] \\ &+ \frac{2\alpha_s}{3r^3} \left[\frac{(\vec{r} \times \vec{p}_1) \cdot \vec{s}_1}{m_1^2} - \frac{(\vec{r} \times \vec{p}_2) \cdot \vec{s}_2}{m_2^2} + \frac{2}{m_1 m_2} \left((\vec{r} \times \vec{p}_1) \cdot \vec{s}_2 - (\vec{r} \times \vec{p}_2) \cdot \vec{s}_1 \right) \right]. \end{aligned} \quad (1.2.25)$$

The transformation into the CM-frame via

$$\begin{aligned} m_q &= m_1 = m_2 \quad (q = c, b \text{ respectively}) \\ \vec{p} &= \vec{p}_1 = -\vec{p}_2 \end{aligned} \quad (1.2.26)$$

and the addition of a linear confining term leads to the final potential

$$\begin{aligned} V(\vec{r}; \vec{p}) &= -\frac{4\alpha_s}{3r} + \sigma r - \frac{4\pi\alpha_s}{3m_q^2} \delta^{(3)}(\vec{r}) - \frac{2\alpha_s}{3m_q^2} \left[\frac{\vec{p} \cdot \vec{p}}{r} + \frac{(\vec{r} \cdot \vec{p})(\vec{r} \cdot \vec{p})}{r^3} \right] \\ &+ \frac{4\alpha_s}{3m_q^2} \left[\frac{8\pi}{3} \delta^{(3)}(\vec{r}) (\vec{s}_1 \cdot \vec{s}_2) + \frac{3(\vec{s}_1 \cdot \hat{r})(\vec{s}_2 \cdot \hat{r}) - \vec{s}_1 \cdot \vec{s}_2}{r^3} \right] + \frac{2\alpha_s}{m_q^2} \frac{(\vec{r} \times \vec{p}) \cdot (\vec{s}_1 + \vec{s}_2)}{r^3} . \end{aligned} \quad (1.2.27)$$

1.2.4. The Spin Interactions

As one can see, the potential in Eq. (1.2.27) is spin dependent, so the energy levels of the unperturbed eigenstates will split due to three interaction types: spin-spin, spin-orbit and tensor interaction. The spin dependence of the potential is expressed in terms of \vec{r} , \vec{p} , \vec{s}_1 and \vec{s}_2 , which is somehow not appropriate. In order to describe the spin dependence in more reasonable quantities, one introduces the total spin

$$\vec{S} = \vec{s}_1 + \vec{s}_2 , \quad (1.2.28)$$

the angular momentum

$$\vec{L} = \vec{r} \times \vec{p} \quad (1.2.29)$$

and the tensor operator

$$S_{12} = 12 \left[\frac{(\vec{s}_1 \cdot \vec{r})(\vec{s}_2 \cdot \vec{r})}{r^2} - \frac{1}{3}(\vec{s}_1 \cdot \vec{s}_2) \right] . \quad (1.2.30)$$

Because experiments provide us with information on the total angular momentum \vec{J} , the orbital angular momentum \vec{L} and the total spin \vec{S} , this is a reasonable choice, since the expectation values of $\langle \vec{s}_1 \cdot \vec{s}_2 \rangle$, $\langle \vec{L} \cdot \vec{S} \rangle$ and $\langle S_{12} \rangle$ can be expressed in terms of the eigenvalues j , l , S of \vec{J} , \vec{L} and \vec{S} .

1.2.4.1. Spin-Spin Coefficient

The equation

$$\vec{S}^2 = S(S+1) = (\vec{s}_1 + \vec{s}_2)^2 = s_1(s_1+1) + s_2(s_2+1) + 2\vec{s}_1 \cdot \vec{s}_2 , \quad (1.2.31)$$

yields

$$\vec{s}_1 \cdot \vec{s}_2 = \frac{1}{2} \left[\vec{S}^2 - s_1(s_1+1) - s_2(s_2+1) \right] . \quad (1.2.32)$$

With quark spin $s_1 = s_2 = 1/2$ one obtains

$$\vec{s}_1 \cdot \vec{s}_2 = \begin{cases} -\frac{3}{4} & \text{for spin singlet } S = 0 \\ +\frac{1}{4} & \text{for spin triplet } S = 1 \end{cases} \quad (1.2.33)$$

1.2.4.2. Spin-Orbit Coefficient

Employing

$$\begin{aligned} \vec{J}^2 = j(j+1) &= (\vec{L} + \vec{S})^2 = \vec{L}^2 + \vec{S}^2 + 2(\vec{L} \cdot \vec{S}) \\ &= l(l+1) + S(S+1) + 2(\vec{L} \cdot \vec{S}) \end{aligned} \quad (1.2.34)$$

leads to

$$\vec{L} \cdot \vec{S} = \frac{1}{2} \left[j(j+1) - l(l+1) - S(S+1) \right] . \quad (1.2.35)$$

Obviously there is no contribution for $l = 0$ or $S = 0$. Tab. 1.2 gives the matrix elements of $\vec{L} \cdot \vec{S}$ for eigenstates with a nonvanishing total spin.

j	$\vec{L} \cdot \vec{S}$
$l+1$	l
l	-1
$l-1$	$-(l+1)$

Table 1.2.: Spin-orbit coupling for $l \neq 0$ and $S = 1$

1.2.4.3. Tensor Coefficient

The tensor term can be expressed using

$$\begin{aligned} (\vec{S} \cdot \vec{r})^2 &= [(\vec{s}_1 + \vec{s}_2) \cdot \vec{r}]^2 = [(\vec{s}_1 \cdot \vec{r}) + (\vec{s}_2 \cdot \vec{r})]^2 \\ &= \frac{1}{2} \vec{r}^2 + 2(\vec{s}_1 \cdot \vec{r})(\vec{s}_2 \cdot \vec{r}) \end{aligned} \quad (1.2.36)$$

$$\Rightarrow (\vec{s}_1 \cdot \vec{r})(\vec{s}_2 \cdot \vec{r}) = \frac{1}{2} (\vec{S} \cdot \vec{r})^2 - \frac{1}{4} \vec{r}^2 . \quad (1.2.37)$$

With the expression

$$\vec{s}_1 \cdot \vec{s}_2 = \frac{1}{2} \vec{S}^2 - \frac{3}{4} \quad (1.2.38)$$

from Eq. (1.2.32) and Eq. (1.2.33) this leads to

$$S_{12} = 2 \left[3 \frac{(\vec{S} \cdot \vec{r})^2}{r^2} - \vec{S}^2 \right] . \quad (1.2.39)$$

For $S = 0$ the tensor term vanishes, as well as in the case of $l = 0$, since

$$\left\langle \frac{r_i r_j}{r^2} \right\rangle = \frac{1}{3} \delta_{ij} . \quad (1.2.40)$$

Further calculations lead to

$$S_{12} = \frac{4}{(2l-1)(2l+3)} \left[\vec{S}^2 \vec{L}^2 - \frac{3}{2} \vec{L} \cdot \vec{S} - 3(\vec{L} \cdot \vec{S})^2 \right] \quad (1.2.41)$$

for the diagonal elements of S_{12} , which are listed in Tab. 1.3.

j	S_{12}
$l+1$	$-\frac{2l}{2l+3}$
l	2
$l-1$	$-\frac{2(l+1)}{2l-1}$

Table 1.3.: Non-vanishing diagonal elements of S_{12}

1.2.5. From Potential To Mass

Since the Schroedinger equation is solved for the spin-independent Cornell potential (Eq. (1.2.11)), the spin-corrections are treated perturbatively:

$$V(\vec{r}) = V(r)_{\text{Cornell}} + \delta V(\vec{r})_{\text{pert.}} . \quad (1.2.42)$$

For the eigenstate masses this means

$$\begin{aligned} M(k^{2S+1}l_j) &= M_{0,kl} + \delta M_{kjlS} \quad \text{with} \\ \delta M_{kjlS} &= \int d^3r \psi^\dagger(\vec{r}) \delta V(\vec{r})_{\text{pert.}} \psi(\vec{r}) = \left\langle \delta V(\vec{r})_{\text{pert.}} \right\rangle . \end{aligned} \quad (1.2.43)$$

Calculating the expectation value $\langle \delta V(\vec{r})_{\text{pert.}} \rangle$ and evaluation of the spin-terms results in the final mass formula

$$\begin{aligned}
 M(k^{2S+1}l_j) = & M_{0,kl} + \frac{4\pi\alpha_s}{3m_q^2} |\psi(0)|^2 + \frac{32\pi\alpha_s}{9m_q^2} \left(\frac{1}{2}S(S+1) - \frac{3}{4} \right) |\psi(0)|^2 \\
 & + \alpha_s \frac{j(j+1) - l(l+1) - S(S+1)}{m_q^2} \left\langle \frac{1}{r^3} \right\rangle + \alpha_s \frac{S_{12}}{3m_q^2} \left\langle \frac{1}{r^3} \right\rangle \\
 & + \frac{2\alpha_s}{3m_q^2} \int d^3r \psi^*(\vec{r}) \left(\frac{1}{r} \vec{\nabla}^2 + \frac{1}{r} \frac{\partial^2}{\partial r^2} \right) \psi(\vec{r}) . \quad (1.2.44)
 \end{aligned}$$

The expectation value $\langle 1/r^3 \rangle$ can be calculated via

$$\left\langle \frac{1}{r^3} \right\rangle = \int d^3r \psi^*(\vec{r}) \frac{1}{r^3} \psi(\vec{r}) = \int dr \frac{1}{r^3} u(r)^2 . \quad (1.2.45)$$

The last term can be evaluated by separating the $\vec{\nabla}^2$ -operator into radius- and angle-dependent operators

$$\vec{\nabla}^2 = \Delta_r + \frac{1}{r^2} \Delta_{\theta,\varphi} . \quad (1.2.46)$$

Knowing the eigenvalue

$$\Delta_{\theta,\varphi} Y_l^m(\theta, \varphi) = -l(l+1) Y_l^m(\theta, \varphi) \quad (1.2.47)$$

and the orthogonal relation

$$\langle Y_l^m | Y_{l'}^{m'} \rangle = \delta_{ll'} \delta_{mm'} \quad (1.2.48)$$

the last term is given by

$$2 \int dr u(r) \left[\frac{1}{r} \frac{d^2}{dr^2} - \frac{1}{r^2} \frac{d}{dr} + \frac{1}{r^3} - \frac{1}{2r^3} l(l+1) \right] u(r) . \quad (1.2.49)$$

1.2.6. Bottomonium Wavefunctions and Eigenstates

The parameters for calculating the bottomonium spectrum were

$$\begin{aligned}
 \alpha_s &= 0.388 \\
 m_b &= 4.7645 \text{ GeV} \\
 \sigma &= 1.02 \text{ GeV/fm} . \quad (1.2.50)
 \end{aligned}$$

They were obtained in [6] with the input states $\Upsilon(1S)$, $\Upsilon(2S)$ and the center of gravity for the $1P$ triplet states $C(1P)$ defined as

$$C(1P) = \frac{1}{9} [5M(\chi_{b_2}) + 3M(\chi_{b_1}) + M(\chi_{b_0})] \approx 9900 \text{ MeV} . \quad (1.2.51)$$

The values for m_b and σ are in the region which one would expect from QCD predictions, but the α_s value is much larger than experimentally measured ($\alpha_s \approx 0.2$). This is due to special properties of the $1S$ state. This method of fitting the parameters to

the mass states was used to see which are the best possible bottomonium mass values one can obtain with this relatively simple model. Using the correct α_s value from experiment, which is measured quite precisely, would nevertheless be the better and more physical way of determining how good this model is.

The wave functions, eigenstates and the radial densities can be seen in figures 1.4, 1.5, 1.6, 1.7 and 1.8 [10]. Tab. 1.4 shows the obtained results in comparison with actual experimental values.

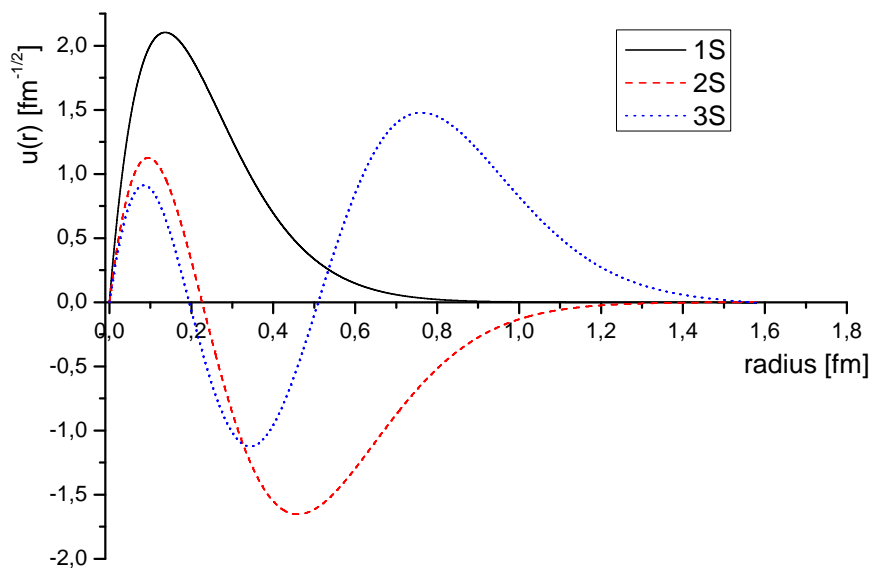


Figure 1.4.: S-wave reduced radial wave functions of $b\bar{b}$ -states ($\alpha_s = 0.388$, $m_b = 4.7645$ GeV, $\sigma = 1.02$ GeV/fm)

Looking at Fig. 1.4, one can see a significant difference between the slope of $\Upsilon(1S)$ and the slopes of the other S-states, which can be explained by keeping in mind that the $\Upsilon(1S)$ state is lying way deeper in the potential funnel than the other states (see Fig. 1.8) and is therefore strongly influenced by the Coulomb term of the potential. This is also the reason for the large value of α_s obtained from the fit to the mentioned mass states.

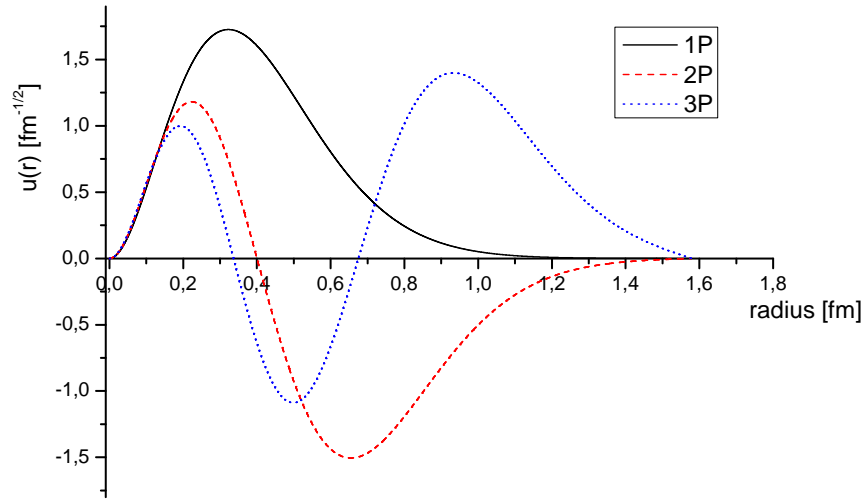


Figure 1.5.: P-wave reduced radial wave functions of $b\bar{b}$ -states ($\alpha_s = 0.388$, $m_b = 4.7645$ GeV, $\sigma = 1.02$ GeV/fm)

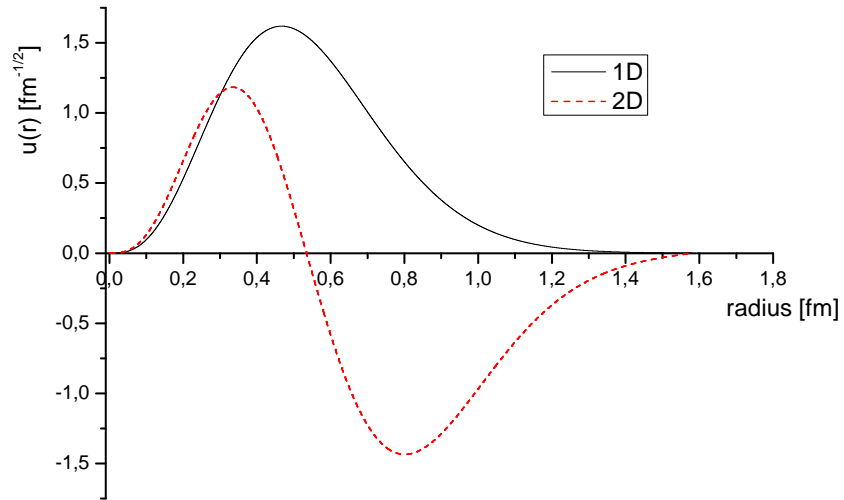


Figure 1.6.: D-wave reduced radial wave functions of $b\bar{b}$ -states ($\alpha_s = 0.388$, $m_b = 4.7645$ GeV, $\sigma = 1.02$ GeV/fm)

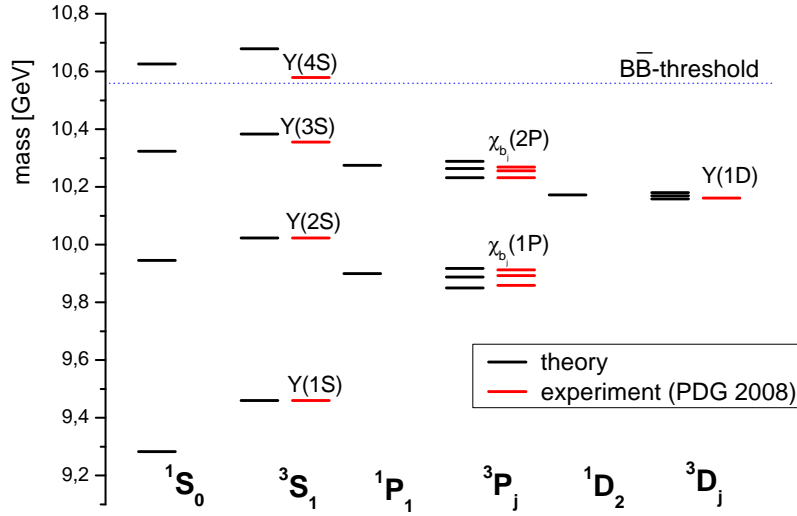


Figure 1.7.: Theoretical predictions for $b\bar{b}$ -states in comparison with experimental data ($\alpha_s = 0.388$, $m_b = 4.7645$ GeV, $\sigma = 1.02$ GeV/fm)

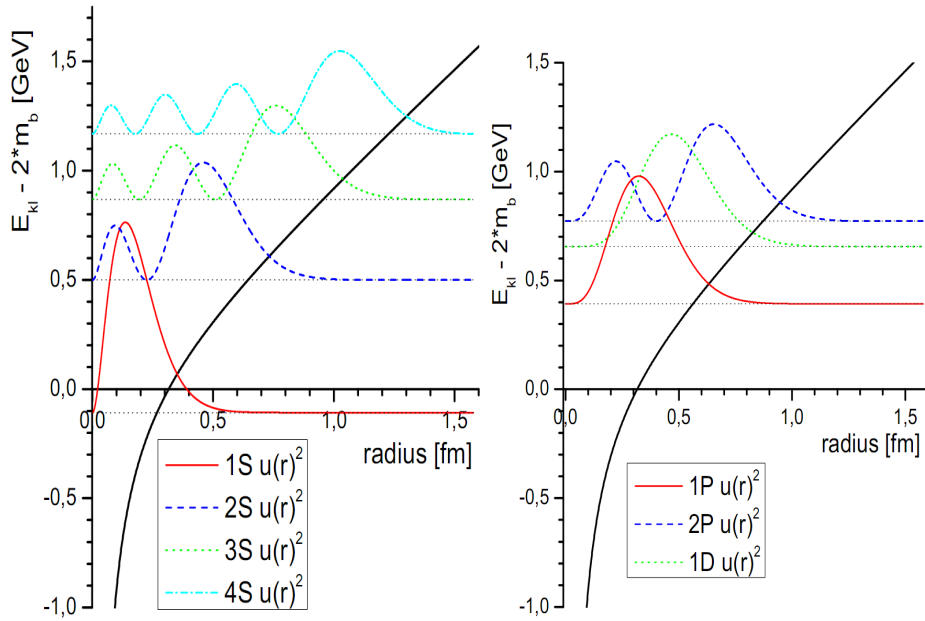


Figure 1.8.: Radial densities of bottomonium plotted together with the used Cornell potential ($\alpha_s = 0.388$, $m_b = 4.7645$ GeV, $\sigma = 1.02$ GeV/fm)

State	Candidate	Mass (theory) [MeV]	Mass (experiment) [MeV]
1^1S_0	(η_b)	9283.0	$(9300 \pm 20 \pm 20)$
1^3S_1	$\Upsilon(1S)$	9460.4	9460.3 ± 0.26
1^1P_1		9900.2	
1^3P_0	$\chi_{b_0}(1P)$	9849.9	$9859.44 \pm 0.42 \pm 0.31$
1^3P_1	$\chi_{b_1}(1P)$	9887.7	$9892.78 \pm 0.26 \pm 0.31$
1^3P_2	$\chi_{b_2}(1P)$	9917.8	$9912.21 \pm 0.26 \pm 0.31$
2^1S_0		9945.6	
2^3S_1	$\Upsilon(2S)$	10023.1	10023.26 ± 0.31
1^1D_2		10172.2	
1^3D_1		10158.0	
1^3D_2	$\Upsilon(1D)$	10169.4	$10151.1 \pm 0.6 \pm 1.6$
1^3D_3		10180.3	
2^1P_1		10274.3	
2^3P_0	$\chi_{b_0}(2P)$	10232.5	$10232.5 \pm 0.4 \pm 0.5$
2^3P_1	$\chi_{b_1}(2P)$	10263.9	$10255.46 \pm 0.22 \pm 0.50$
2^3P_2	$\chi_{b_2}(2P)$	10289.0	$10268.65 \pm 0.22 \pm 0.50$
3^1S_0		10323.7	
3^3S_1	$\Upsilon(3S)$	10383.3	10355.2 ± 0.5
4^1S_0		10626.2	
4^3S_1	$\Upsilon(4S)$	10678.9	10580.0 ± 3.5

Table 1.4.: $b\bar{b}$ -states from theory and experiment in comparison ($\alpha_s = 0.388$, $m_b = 4.7645$ GeV, $\sigma = 1.02$ GeV/fm)

As one can see in Fig. 1.7, the Breit interaction generally describes the bottomonium spectrum quite well, but considering that three mass-states were used to fit the parameters to the spectrum, the obtained spectrum is rather disappointing. The predictive power near the $B\bar{B}$ -threshold is rather unsatisfactory and the predictions for the triplet P-state splittings are unsatisfactory, since

$$\Phi_b^{\text{theory}}(1P) = \left(\frac{M(\chi_{b_2}) - M(\chi_{b_1})}{M(\chi_{b_1}) - M(\chi_{b_0})} \right) \Big|_{\text{theory}} = \frac{4}{5} = \Phi_b^{\text{theory}}(2P) \quad (1.2.52)$$

differ significantly from the experimental found values

$$\Phi_b^{\text{experiment}}(1P) = \left(\frac{M(\chi_{b_2}) - M(\chi_{b_1})}{M(\chi_{b_1}) - M(\chi_{b_0})} \right) \Big|_{\text{experiment}} = 0.58 \pm 0.03 \quad (1.2.53)$$

$$\Phi_b^{\text{experiment}}(2P) = \left(\frac{M(\chi'_{b_2}) - M(\chi'_{b_1})}{M(\chi'_{b_1}) - M(\chi'_{b_0})} \right) \Big|_{\text{experiment}} = 0.57 \pm 0.05 \quad (1.2.54)$$

The main aspect which can be learned from Fig. 1.7 is that there are a lot of predicted states, which have not been discovered in experiments yet. Therefore a search for new particles in the bottomonium region should be promising and worth the effort.

1.3. The $X(3872)$ -Resonance

The $X(3872)$ is a narrow resonance discovered by the BELLE collaboration in summer 2003 [11]. The invariant mass distribution for $J/\psi \pi^+ \pi^-$ in exclusively reconstructed $B^\pm \rightarrow J/\psi \pi^+ \pi^- K^\pm$ events has a peak at about 3872 MeV, implying the $X(3872)$ is produced via $B^\pm \rightarrow X K^\pm$ and is then decaying into $J/\psi \pi^+ \pi^-$. The upper limit on its width is very narrow, meaning the lifetime of the X is much longer than expected. CDF, DØ and BaBar soon confirmed the existence of the $X(3872)$ resonance in the discovery channel [12][13][14]. The situation that the X mass and its narrow width do not agree well with quark model expectations has led to speculation that the X could be a novel charmonium state such as a hybrid, a tetraquark or a molecule.

The discovery mode mentioned above can be expressed schematically in terms of the quark contents of the hadrons:

$$\underbrace{(\bar{b}u)}_{B^+} \rightarrow X + \underbrace{(\bar{s}u)}_{K^+}, \quad X \rightarrow \underbrace{(c\bar{c})}_{J/\psi} + \underbrace{(u\bar{d})}_{\pi^+} + \underbrace{(\bar{u}d)}_{\pi^-} \quad (1.3.1)$$

The first sequence of the decay chain is a weak decay, where the \bar{b} quark decays into the 3 quark state $\bar{c} + c + \bar{s}$, involving QCD interactions, which can create additional $q\bar{q}$ -pairs of the same quark flavor. Since both c and \bar{c} are too heavy to be created in the X decay, they must have already existed as constituents of the X . The X could also have additional constituents such as a gluon or an $u\bar{u}$ - or a $d\bar{d}$ -pair created by QCD interactions.

Soon after the discovery of the $X(3872)$, people noticed a curious fact: its mass is extremely close to the sum of D^0 and \bar{D}^{*0} mass. Several physicists immediately investigated the possibility that $X(3872)$ is a weakly bound molecule of the charmed mesons D^0 and \bar{D}^{*0} . Since the mass of this constituents is slightly higher than the mass of $X(3872)$, the difference in mass could be the binding energy which holds $D^0 \bar{D}^{*0}$ together.

1.3.1. Quantum numbers of the $X(3872)$

The experimental determination of the J^{PC} quantum numbers of the $X(3872)$ can be used to narrow down its possible interpretations.

The mass of the $X(3872)$ is about 140 MeV above the $D^0 \bar{D}^0$ threshold at 3729.68 ± 0.34 MeV and the $D^+ D^-$ threshold at 3739.24 ± 0.4 MeV. Its width of $3.0^{+2.1}_{-1.7}$ MeV [15]

is narrow compared to the width of other charmonium states like $\Gamma(\psi_{3770}) = 27.3 \pm 1.0$ MeV and $\Gamma(\psi_{4040}) = 80 \pm 10$ MeV, which are also above the $D\bar{D}$ threshold. An overview of important masses concerning the $X(3872)$ is given in Tab. 1.5.

	mass [MeV]	width [MeV]
$\psi(3770)$	3772.92 ± 0.35	27.3 ± 1.0
$X(3872)$	3872.2 ± 0.8^2	$3.0^{+2.1}_{-1.7}$
$\psi(4040)$	4039 ± 1	80 ± 10
$D^0\bar{D}^0$	3729.68 ± 0.34	–
$D^0\bar{D}^{*0}$	3871.81 ± 0.36	–
D^+D^-	3739.24 ± 0.40	–

Table 1.5.: Overview of important masses concerning the $X(3872)$ [15]

Since the decay into $D\bar{D}$ dominate the width of ψ_{3770} and ψ_{4040} , the decay mode $X \rightarrow D\bar{D}$ must be either forbidden by its quantum numbers or suppressed by some dynamical mechanism, for example an angular momentum barrier. If the X consists of two constituents with orbital angular momentum L , the wavefunction for the constituents to have small separation r would be suppressed by a factor r^L and so would be the decay, if it required these constituents to come close together.

D and \bar{D} have quantum numbers $J^P = 0^-$, parity and charge conjugation quantum numbers for a $D\bar{D}$ system with orbital angular momentum $L = 0, 1, 2, \dots$ are $P = (-1)^L$ and $C = (-1)^L$. Thus a $D\bar{D}$ system can have quantum numbers in the sequence

$$J^{PC} = 0^{++}, 1^{--}, 2^{++}, \dots \quad (1.3.2)$$

If the quantum numbers of X were in the sequence

$$J^{PC} = 0^{-\pm}, 1^{+\pm}, 2^{-\pm}, \dots \quad (1.3.3)$$

the decay $X \rightarrow D\bar{D}$ would be forbidden by parity conservation of the strong interaction. If the quantum numbers of X were in the sequence

$$J^{PC} = 0^{+-}, 1^{-+}, 2^{+-}, \dots \quad (1.3.4)$$

it would be allowed by parity but forbidden by charge conjugation symmetry of the strong interaction. The narrow width of the X and the nonobservation of the $D\bar{D}$ decay mode can be explained if its quantum numbers are either in the sequence (1.3.3) or in the sequence (1.3.4) or else in the sequence (1.3.2) with the condition, that the X has sufficiently large internal orbital angular momentum L which suppresses the decay by a factor r^L as explained above.

²The latest pdg mass value from the Review of Particle Physics 2010 is 3871.56 ± 0.22 MeV, which is indeed slightly below the latest value for the $D^0\bar{D}^{*0}$ mass ($m(D^0\bar{D}^{*0}) = 3871.79 \pm 0.30$ MeV).

Experimental evidence for the radiative decay mode $X \rightarrow J/\psi \gamma$ verifies that the X has positive charge conjugation [16], since J/ψ and γ both have quantum numbers $J^{PC} = 1^{--}$ and a system of $J/\psi \gamma$ can have quantum numbers $J^{PC} = 0^{\pm+}, 1^{\pm+}, 2^{\pm+}, \dots$. Studies of the angular distributions of $X(3872)$ decays ruled out all J^{P+} assignments with $J \leq 2$ other than 1^{++} and 2^{++} , with $J^{PC} = 1^{++}$ being the favorable choice [17].

1.3.2. Interpretations of the $X(3872)$

The charmonium state interpretation with constituents $c\bar{c}$ and the hadronic molecule interpretation with constituents DD^* are the most predictive ones for the $X(3872)$ resonance.

1.3.2.1. Charmonium Interpretation

Since the observed decay modes of X include J/ψ , an interpretation as a charmonium state with constituents $c\bar{c}$ seems logical. This option has been extensively investigated in [18] [19] [20]. Figure 1.9 shows the theoretical prediction for the charmonium spectrum in comparison with experimental observed data and possible $X(3872)$ candidates [10]. Of course all the charmonium states that have already been observed are ruled out as candidates for the $X(3872)$. The possible charmonium candidates for the X include members of the multiplet of the first radial excitation of P -wave charmonium, $h_c(2P)$ and $\chi_{cJ}(2P)$, $J = 0, 1, 2$ and members of the multiplet of the ground-state D -wave charmonium, $\eta_{c2}(1D)$ and $\psi_J(1D)$, $J = 1, 2, 3$, see Tab. 1.6.

State	$n^{2S+1}L_J$	J^{PC}
$h_c(2P)$	2^1P_1	1^{+-}
$\chi_{c0}(2P)$	2^3P_0	0^{++}
$\chi_{c1}(2P)$	2^3P_1	1^{++}
$\chi_{c2}(2P)$	2^3P_2	2^{++}
$\eta_{c2}(1D)$	1^1D_2	2^{-+}
$\psi_1(1D)$	1^3D_1	1^{--}
$\psi_2(1D)$	1^3D_2	2^{--}
$\psi_3(1D)$	1^3D_3	3^{--}

Table 1.6.: Quantum numbers of the charmonium states, which are possible candidates for the $X(3872)$.

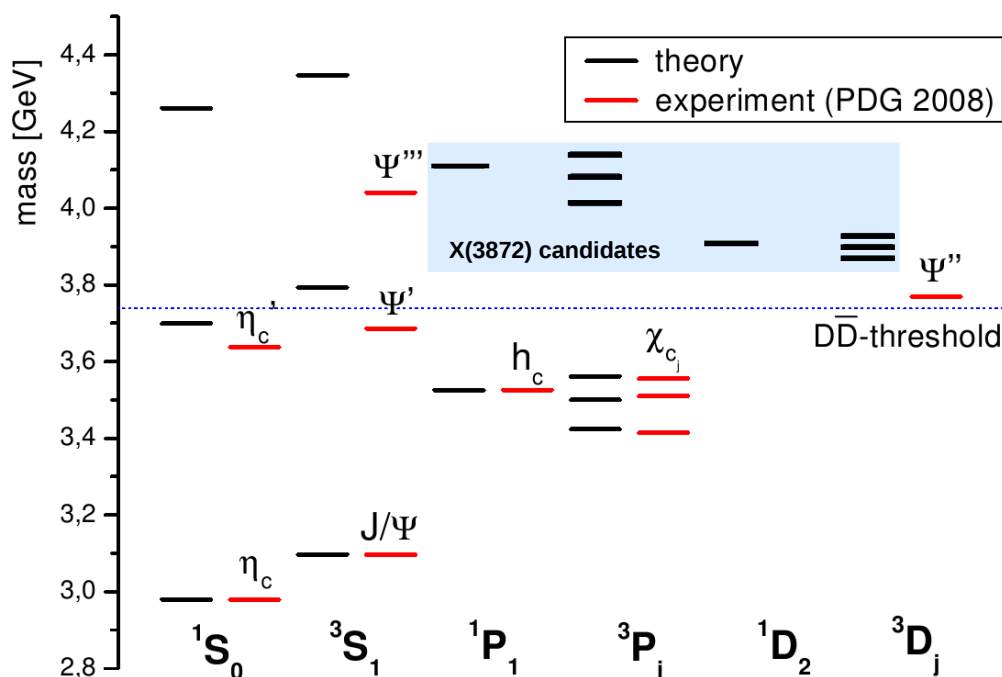


Figure 1.9.: Theoretical predictions from Breit interaction for the $c\bar{c}$ spectrum in comparison with experimental data ($\alpha_s = 0.29$, $m_c = 1.2185$ GeV, $\sigma = 1.306$ GeV/fm), the blue region marks possible $X(3872)$ candidates.

The experimental observation of $X \rightarrow J/\psi \gamma$ unambiguously eliminates all $C = -$ candidates and since the $X(3872)$ most likely has quantum numbers 1^{++} , the best possible candidate would be $\chi_{c1}(2P)$. The narrow line shape of the X could be explained by parity or charge conjugation symmetry of the strong interaction, so the remaining quantum numbers are listed in Eq. (1.3.3) and Eq. (1.3.4). Therefore the remaining candidates are $\eta_{c2}(1D)(J^{PC} = 2^{-+})$ and $\chi_{c1}(2P)(J^{PC} = 1^{++})$. Since measurements of the angular distribution of $X \rightarrow J/\psi \pi^+\pi^-$ rule out $\eta_{c2}(1D)$ [17], the only remaining charmonium candidate is $\chi_{c1}(2P)$. Evidence against the charmonium interpretation comes from the approximate isospin symmetry of the strong interaction [21]. Measurements of the invariant mass distribution for the discovery mode J/ψ imply that the $\pi^+\pi^-$ pair comes from a virtual ρ resonance with isospin 1. Therefore the system $J/\psi \rho$ has isospin 1, since all charmonium states have isospin 0. Therefore the discovery mode would be isospin violating and should at least be suppressed compared to isospin conserving modes. However, the branching fraction of the isospin conserving mode $X \rightarrow J/\psi \omega^* \rightarrow J/\psi \pi^+\pi^-\pi^0$ is approximately equal to that of the isospin violating mode $X \rightarrow J/\psi \rho^* \rightarrow J/\psi \pi^+\pi^-$. A more likely interpretation would be that the $X(3872)$ is a charm meson molecule.

1.3.2.2. Charm Meson Molecule Interpretation

The proximity of the $X(3872)$ mass to the threshold for the charm mesons D^0 and \bar{D}^{*0} motivated the option of a charm meson molecule. Since the X has charge conjugation $C = +$, it could be a hadronic molecule with constituents DD^* . First quantitative studies of the possibility of charmed meson molecules were carried out by Tornqvist 1993 using a one-pion exchange potential model, see Tab. 1.7.

Constituents	J^{PC}	Mass [MeV]
$D\bar{D}^*$	0^{-+}	≈ 3870
$D\bar{D}^*$	1^{++}	≈ 3870
$D^*\bar{D}^*$	0^{++}	≈ 4015
$D^*\bar{D}^*$	0^{-+}	≈ 4015
$D^*\bar{D}^*$	1^{+-}	≈ 4015
$D^*\bar{D}^*$	2^{++}	≈ 4015

Table 1.7.: Possible weakly-bound states of charmed mesons coming from an one-pion exchange potential [22].

After the discovery of the $X(3872)$ a potential model that includes both one-pion-exchange and quark-exchange potentials was considered and the possibility that the $C = +$ superposition of $D^0\bar{D}^{*0}$ and $D^{*0}\bar{D}^0$ could form a weakly-bound state in the S-wave 1^{++} channel was justified [23]. Its particle content is

$$|X\rangle = \frac{1}{\sqrt{2}} \left(|D^0\bar{D}^{*0}\rangle + |D^{*0}\bar{D}^0\rangle \right) \quad , \quad (1.3.5)$$

which means that the $X(3872)$ exists half of its lifetime as a $|D^0\bar{D}^{*0}\rangle$ molecule and the other half of its lifetime as a $|D^{*0}\bar{D}^0\rangle$ molecule. The large $X(3872)$ branching fraction into $D^0\bar{D}^{*0}$ compared to the branching fraction into the discovery mode ($f_{D^0\bar{D}^{*0}}/f_{J/\psi\pi^+\pi^-} \approx 10$) would also be explained by such a composition³. Another mechanism for generating a $D\bar{D}^*$ molecule could be an accidental fine-tuning of the mass of $\chi_{c1}(2P)$ or $h_c(2P)$ to the $D^0\bar{D}^{*0}/D^{*0}\bar{D}^0$ threshold which creates a DD^* molecule with quantum number 1^{++} or 1^{-+} , respectively [24]. All experimental data seem to be compatible with the interpretation of $X(3872)$ being a S-wave $D^0\bar{D}^{*0}$ molecule with quantum numbers 1^{++} and this model is very predictive [25], but it is not unambiguously approved yet.

1.3.2.3. Other Interpretations

Several other interpretations of the $X(3872)$ have been proposed but have not been as established as the charmed meson molecule interpretation and are mentioned for

³The width of the $X(3872)$ resonance is broad enough to allow the decay $X(3872) \rightarrow D^0\bar{D}^{*0}$ without violating energy conservation.

completeness only: The $X(3872)$ could also be a

- **hybrid charmonium** state with two charm quarks and one valence-gluon $c\bar{c}g$ [26] [27] or a
- **glueball** with constituents ggg [28] or a
- **tetraquark** with constituents $c\bar{c}q\bar{q}$ [29] or a diquark-antidiquark bound state with constituents $cu + \bar{c}\bar{u}$ [30].

1.4. Searching for a bottom counterpart of $X(3872)$

Since the $X(3872)$ has rather unusual properties and its nature is not unambiguously identified yet, a discovery of a bottom counterpart X_b should shed more light on the issue. An analogue search $X_b \rightarrow \Upsilon \pi^+ \pi^-$ as in the $X(3872)$ discovery channel was proposed in [31]. A search for states with $J^P = 1^+$ at electron-positron colliders is nontrivial since the initial state quantum numbers are always $J^P = 1^-$. The analogue state $X(3872)$ can be 1^+ since it is produced in a weak, parity violating B decay (Eq. (1.4.1))

$$\begin{array}{ccc}
 B^0 & \rightarrow & X(3872) + K^0 \\
 0^- & & \underbrace{1^+ \quad 0^-}_{L=1}
 \end{array} \tag{1.4.1}$$

The production of X_b in e^+e^- collisions would need additional pions to conserve parity and charge conjugation symmetry:

$$\begin{array}{ccc}
 \underbrace{e^+e^-}_{1^{--}} & \not\rightarrow & \underbrace{X_b}_{1^{++}} \\
 & & \rightarrow \underbrace{X_b + \pi^0 + \gamma}_{\substack{1^{++} \quad 0^{-+} \quad 1^{--} \\ L=1 \\ 1^{--}}}
 \end{array} \tag{1.4.2}$$

$$\begin{array}{ccc}
 & & \rightarrow \underbrace{X_b + \pi^+ + \pi^-}_{\substack{1^{++} \quad 0^- \quad 0^- \\ L=1 \\ 1^{--}}} \\
 & & \underbrace{\quad \quad \quad}_{1^{--}}
 \end{array} \tag{1.4.3}$$

The analysis with the π^0 (1.4.2) needs an additional γ to conserve charge conjugation symmetry. Since this is a threebody decay, the kinematics allows to create one particle at rest, whereas the other two particles share the available kinetic energy. This analysis is performed at the limit where $E_\gamma \approx 0$ by demanding that the photon is the particle which is created “at rest” and therefore cannot be detected. The X_b and the π^0 share the available energy as in a two body decay. If the X_b had quantum numbers

$J^{PC} = 1^{+-}$, the additional γ in Eq. (1.4.2) would not be necessary. This method is therefore sensitive to new particles with quantum numbers 1^{++} and 1^{+-} .

If the X_b would be a bottom meson molecule of the form

$$|X_b\rangle = \frac{1}{\sqrt{2}} \left(|B^0 \bar{B}^{*0}\rangle + |B^{*0} \bar{B}^0\rangle \right) \quad (1.4.4)$$

(equivalent to the $X(3872)$ in the charm sector), it should decay into $B^0 \bar{B}^{*0}$ or $B^{*0} \bar{B}^0$ with a larger branching fraction than into $X_b \rightarrow \Upsilon(1S) \pi^+ \pi^-$. A search in

$$e^+ e^- \rightarrow B^{(*)} \bar{B}^{(*)} (\pi) (\pi) \quad (1.4.5)$$

might reveal such new states like the X_b .

2

Experimental Setup

What type of computer do you have?
And please don't say a white one.

Sheldon Cooper, PhD [32]

High energy physics requires a complex and expensive experimental setup. Usually a set of accelerators is used to accelerate stable particles (electrons, positrons, protons, antiprotons) through an electric field to a desired energy. Additional magnetic fields, bending and focussing systems are needed to bring these particles to collision at a specific location which is called the interaction region. Around this interaction region a detector is build for the purpose of detecting and recording properties of the collision products.

2.1. Basic Principles

Highly accelerated particles with almost the speed of light have to be described by relativistic variables, which satisfy the relativistic energy conditions

$$E_0 = m \tag{2.1.1}$$

$$E = \sqrt{m^2 + \vec{p}^2} \quad . \tag{2.1.2}$$

Particles with four-momenta p_1 and p_2 are often described with the Mandelstam-variable

$$s = (p_1 + p_2)^2 = (E_1 + E_2)^2 - (\vec{p}_1 + \vec{p}_2)^2 \quad . \tag{2.1.3}$$

\sqrt{s} is the available energy in the center of mass system (CMS) of the two particles. Since energy is equivalent to mass, new particles can be created, if \sqrt{s} is higher than the threshold energy of the new particle, which is its mass (Eq. (2.1.1)).

Accelerators can be divided into three groups:

Electron-positron colliders such as BEPC II or KEKB. Electron positron colliders are built for precision measurements, since the colliding particles have no substructure and therefore the initial state and the center of mass energy are well known. When built as a circular collider their maximal beam energy is limited due to energy loss coming from synchrotron radiation. The synchrotron radiation energy loss ΔE is proportional to $1/m^4$ and therefore light particles like electrons and positrons have much larger energy loss than heavy particles like protons. Therefore the next high energy electron-positron collider is supposed to be a linear collider, prohibiting large energy loss from synchrotron radiation.

Hadron colliders usually collide protons with protons (LHC) or protons with antiprotons (Tevatron). Since their energy loss due to synchrotron radiation is much smaller, hadron colliders achieve the highest possible energies. Due to the substructure of the colliding particles only constituents of the hadron, which just carry a fraction of the hadron's momentum, interact with each other. Therefore the initial state is not well known and due to fragmentation in the strong interaction, the multiplicity in the events is much higher. Figure 2.1 shows the typical event shapes for hadronic pp collisions (recorded by ALICE, LHC 2010) and leptonic e^+e^- events recorded by BELLE.

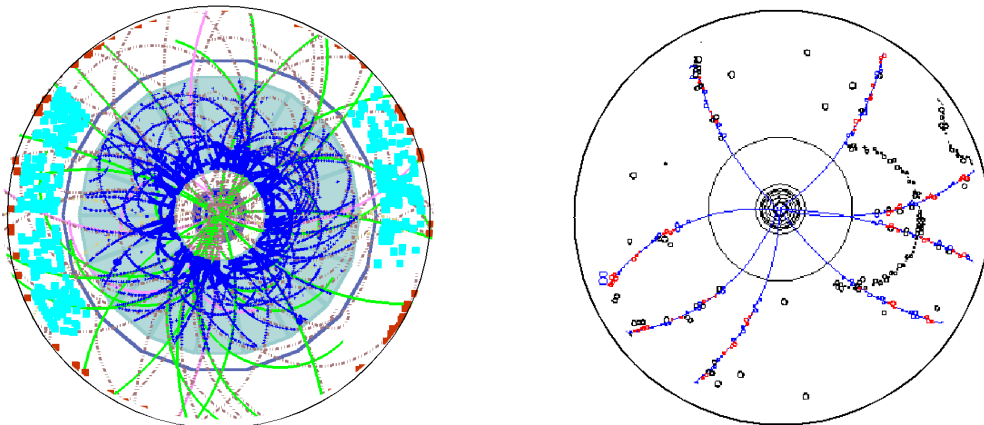


Figure 2.1.: Typical pp event (left) compared to typical e^+e^- event (right).

Hadron-electron colliders are rare and mainly fix target experiments. The HERA experiment at DESY, Hamburg, was the only hadron-electron collider ever built. This experiment made important contributions to the substructure of the proton.

2.2. Luminosity

Energy determines whether a certain production mechanism is possible at all, but yet there is no information about how often a certain process occurs. The cross section σ gives the probability of a physical process at a given energy. After a certain time of data taking, the process of interest can be found N times recorded in the data. The production rate dN/dt of a certain process is given by

$$\frac{dN}{dt} = \mathcal{L} \cdot \sigma \quad (2.2.1)$$

with \mathcal{L} being the luminosity of the accelerator, depending only on the properties of the beam and given by

$$\mathcal{L} = \frac{N_1 N_2 f}{4\pi\sigma_x\sigma_y} \quad (2.2.2)$$

N_1, N_2 are the numbers of particles per bunch, σ_x, σ_y are the spatial dimensions of the bunches and f is the bunch collision rate.

2.3. KEKB Accelerator

The KEKB accelerator is an asymmetric high luminosity electron-positron collider [33] [34] at Tsukuba, Japan. It was designed as a B-factory whose main goal is the investigation of B-physics and therefore to produce a maximum number of B meson pairs (mesons which contain one b or \bar{b} quark). The asymmetry in the beam energies causes B mesons from Υ decays to have a non-zero Lorentz boost in the laboratory frame. A boost of

$$\beta\gamma = \frac{E_{e^-} - E_{e^+}}{\sqrt{s}} = 0.425 \quad (2.3.1)$$

was chosen to optimize the detector acceptance for Belle. Figure 2.2 shows a schematic layout of the KEKB accelerator complex. The electrons are generated by an electron gun and are then accelerated up to 8 GeV in a linear accelerator (LINAC) before they get injected into the high energy ring (HER). Positrons are produced by shooting an electron beam on a tungsten target. A LINAC is used to accelerate the positrons up to an energy of 3.5 GeV before they get injected into the low energy ring (LER).

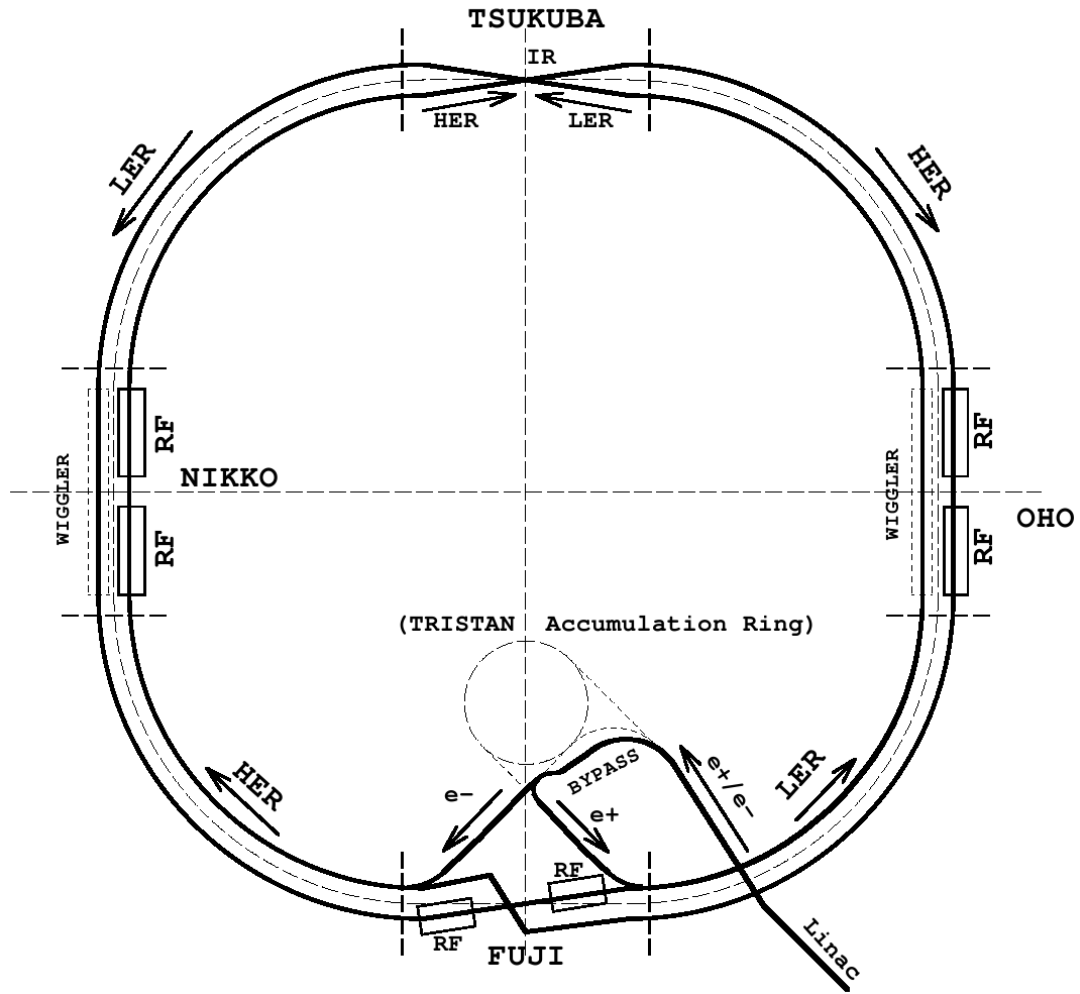


Figure 2.2.: Configuration of the KEKB accelerator system.

The circumference of each ring is 3016 m. With 1584 bunches per beam, the beams cross each other inside the BELLE detector with a crossing rate of 509 MHz at a finite angle of 22 mrad. Crab cavities are used to keep the effective crossing area $4\pi\sigma_x\sigma_y$ as small as possible by rotating each bunch in the interaction region shortly before the collision to get head-on collisions (Fig. 2.3). It is notable that the KEKB accelerator achieved a world record in luminosity of $2.11 \cdot 10^{34} \text{cm}^{-2}\text{s}^{-1}$ in June 2009. This is more than twice its design luminosity and is mostly due to the use of crab cavities. Since BELLE started to take data the integrated luminosity has passed the 1000fb^{-1} threshold.

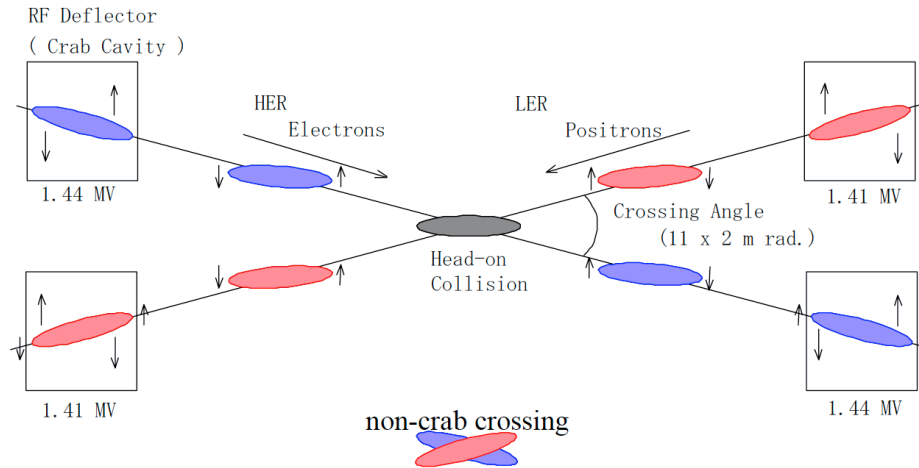


Figure 2.3.: Bunch rotating through crab cavities in order to get head-on collisions.

2.4. BELLE detector

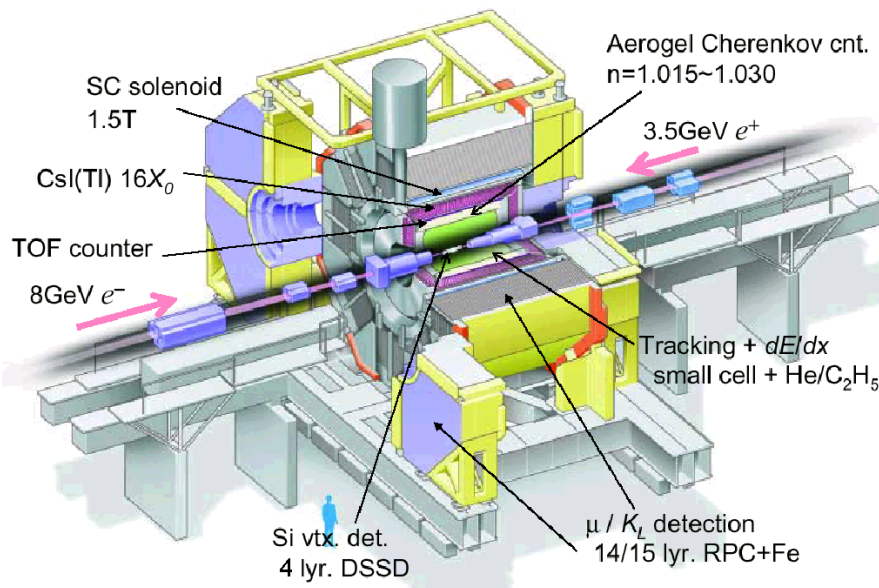


Figure 2.4.: Schematic overview of the BELLE detector

Figure 2.4 shows the layout of the BELLE detector. The detector is constructed around the KEKB beam pipe. It has an iron structure, which is used as a yoke for a superconducting solenoid, which provides a magnetic field of 1.5 T. As every large particle detector BELLE has an onion peel like structure with different kinds of subdetectors to identify the particles and measure their properties.

2.4.1. Silicon Vertex Detector

In the innermost region to the beam pipe the silicon vertex detector (SVD) is located to measure B-decay vertices and the tracks of charged particles inside the magnetic field. The first SVD version, SVD1, was composed of three layers of double sided silicon strip detectors (DSSD). Due to massive radiation damage it got replaced by SVD2, which is more resistant against radiation damage and has an even better performance. SVD2 was installed in 2003 and it has four layers of DSSD which cover the region $17^\circ < \theta < 150^\circ$. The four layers are composed of 6, 12, 18 and 18 ladders in the first, second, third and fourth layers respectively. A schematic view of SVD2 can be seen in Fig. 2.5. The z -vertex resolution of $\sigma_{\Delta z} \sim 80 \mu\text{m}$ covers the full nominal angular coverage of the Belle detector.

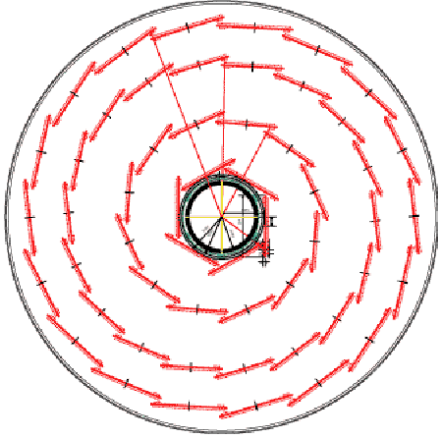


Figure 2.5.: Schematic view of the SVD2 at BELLE. The four layers have the radii $r_1 = 20.0 \text{ mm}$, $r_2 = 43.5 \text{ mm}$, $r_3 = 70.0 \text{ mm}$, $r_4 = 88.0 \text{ mm}$

2.4.2. Central Drift Chamber

Outside of the silicon vertex detector a central drift chamber (CDC) measures three dimensional trajectories and momenta of charged particles. It is filled with helium and ethane (50:50) with ethane serving as quench gas. By precise measurements of the energy loss dE/dx of the particle inside the CDC, important information for the trigger system and the particle identification is given. The CDC has 50 layers of either axial or stereo wires that are cylindrically arranged around the beam axis. This configuration creates drift cells with a maximum drift distance of 8 – 10 mm and a radial thickness of 15.5 – 17mm. The CDC resolution parameters are:

$$\sigma_{r\phi} = 130 \mu\text{m}, \quad \sigma_z = 200 - 1400 \mu\text{m}, \quad \frac{\sigma_{p_T}}{p_T} = 0.3\% \sqrt{p_T^2 [\text{GeV}] + 1}, \quad \frac{\sigma_{dE/dx}}{dE/dx} = 6\%$$

2.4.3. Aerogel Cherenkov Counter

When a charged particle passes matter it causes polarization in the medium's atomic structure. If the particle's velocity is faster than the speed of light inside this medium

$$c_{\text{medium}} = \frac{c_{\text{vacuum}}}{n_{\text{medium}}}, \quad (2.4.1)$$

Cherenkov radiation is emitted. This Cherenkov light can be used for particle identification purposes, since it provides information on the particle's velocity. Additional momentum measurements from the CDC are used to extract information about the particle's mass. BELLE uses threshold Cherenkov counters, which are used to see whether a particle's velocity is above the threshold velocity of Cherenkov light production. The Cherenkov light is detected by fine-mesh photomultipliers (FM-PMT), which are designed to operate in strong magnetic fields (1.5 T). The refractive index of the aerogel Cherenkov counters (ACC) ranges from $n = 1.015$ in the barrel part to $n = 1.030$ in the endcap part of the detector (Fig. 2.6).

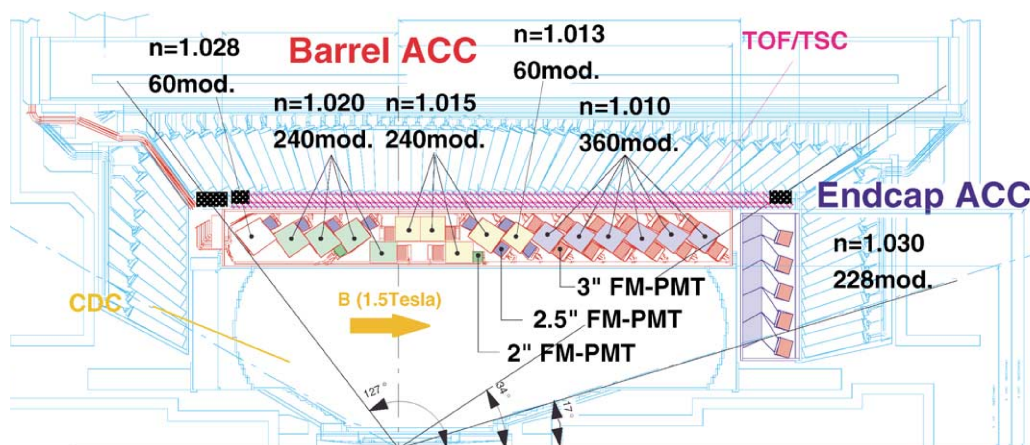


Figure 2.6.: Arrangement of the Belle aerogel Cherenkov counters.

The ACC provides π/K separation in the momentum region $1.1 \text{ GeV} \leq |\vec{p}| \leq 3.6 \text{ GeV}$. By detecting the light output of the Cherenkov counters the endcap ACC can be used for flavor tagging.

2.4.4. Time Of Flight Measurement

The time of flight (TOF) detector made of plastic scintillator bars is used to distinguish kaons from pions for momenta below 1.2 GeV and offers precise event timing to the Belle trigger system. The TOF detector has a time resolution of $\sigma_t \sim 100 \text{ ps}$. Knowing the travel time and the distance to the interaction point ($r_{\text{TOF}} = 1.2 \text{ m}$) the particle's mass can be calculated.

2.4.5. Electromagnetic Calorimeter

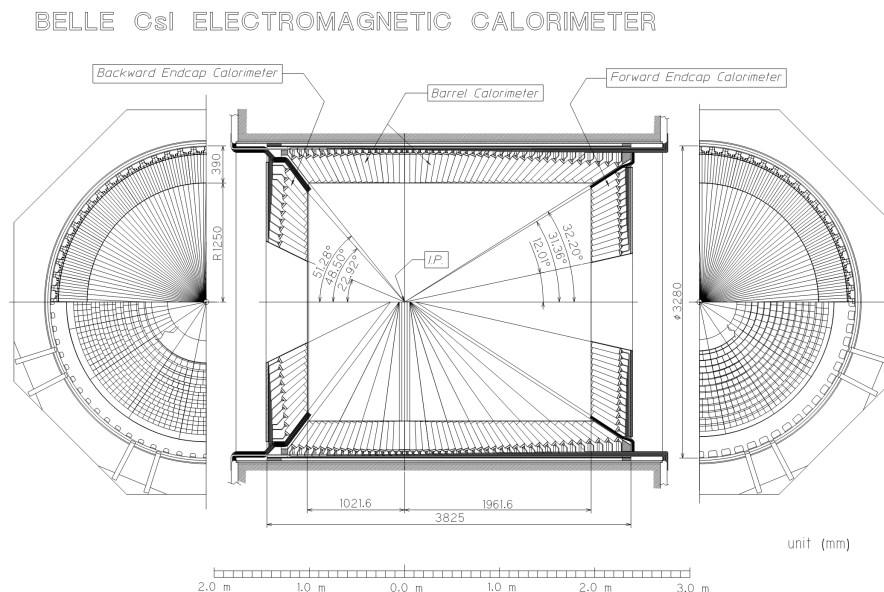


Figure 2.7.: Configuration of the Belle electromagnetic calorimeter

The electromagnetic calorimeter (ECL) is used for measuring the energy and position of electrons and photons with high efficiency and resolution. The overall configuration of the ECL is shown in Fig. 2.7. Most of the photons are products of decay cascades and have relatively low energy, therefore a good performance below 500 MeV is important. However, a good performance for high energy photons e.g. from two-body decay modes like $B \rightarrow K^*\gamma$ or $B \rightarrow \pi^0\pi^0$ is also necessary. Thus the calorimeter has a fine-grained segmentation, because high momentum π^0 detection needs high resolution of two close photons and precise determination of their opening angle. Thallium doped CsI crystals with dimensions $5\text{cm} \times 5\text{cm} \times 30\text{cm}$ ($16X_0$) are used for that purpose. The ECL is also used for electron identification by comparison of the charged particle track momentum and the deposited energy. The ECL resolution parameters are:

$$\frac{\sigma_E}{E[\text{GeV}]} = \frac{1.3\%}{\sqrt{E[\text{GeV}]}} \quad , \quad \sigma_{\text{position}} = \frac{0.5\text{cm}}{\sqrt{E[\text{GeV}]}} \quad . \quad (2.4.2)$$

2.4.6. The K_L^0 and μ Detection System

The iron structure outside the superconducting solenoid functions not only as a yoke for the magnet but also contains a system for detecting K_L^0 -mesons and muons (KLM). The iron structure is used as absorber material for the KLM system. The K_L^0 mesons and muons penetrate the iron layers and trigger hadronic and electromagnetic showers. The direction of the showers can be measured by 15 layers of glass-electrode-resistive counters, which detect charged particles (Fig. 2.8). This also allows to identify weakly

interacting muons. Muons get deflected by multiple scattering, but still travel much further without being absorbed than charged hadrons such as π^\pm or K^\pm . The KLM covers the polar angular range of $20^\circ < \theta < 155^\circ$ and has an angular resolution of 30 mrad in θ and ϕ direction.

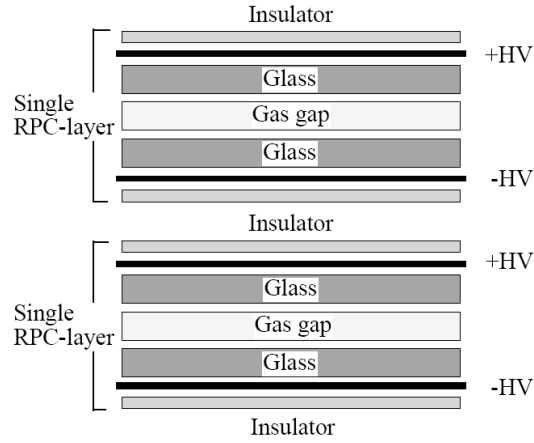


Figure 2.8.: Profile view of a resistive plate counter

Analysis and Results

Oh, there's my missing neutrino.
 You were hiding from me as an
 unbalanced charge, weren't you, you
 little subatomic Dickens?

Sheldon Cooper, PhD [35]

Analysing data from high energy physics experiments is very complex since the short-lived particles decay immediately and can only be reconstructed by their decay particles. Descriptions of the methods which were used for the analysis and the outcoming results are given in this chapter.

3.1. Energy Scan Data

As mentioned in the introduction, energy scan data between the $\Upsilon(4S)$ and the $\Upsilon(6S)$ resonances is used as a basis for the analysis. In addition data from $\Upsilon(1S)$, $\Upsilon(2S)$, $\Upsilon(3S)$, $\Upsilon(4S)$ and $\Upsilon(5S)$ runs was used to enhance the statistics and to crosscheck for known phenomena in this region (e.g. $B - \bar{B}$ oscillation in $\Upsilon(4S)$ decays). The data used for the analysis and the integrated luminosity for each data point is given in Tab. [B.1](#).

3.2. Inclusive Dilepton Analysis

Energy scans are usually not performed with a large integrated luminosity, therefore one should consider an inclusive approach for such an energy scan analysis. B mesons have a relatively large semileptonic branching fraction of $\Gamma_{sl} = 10.33\%$ [15]. Demanding both, B and \bar{B} meson, to decay semileptonically reduces the ratio by a factor of 10.33, resulting in a final branching fraction of $\Gamma_{slf} = 1.07\%$ for semileptonic B/\bar{B} meson decays. A highly inclusive analysis such as this provides large statistics thanks

to the large branching ratios and efficiencies at the cost of limited information about the dynamics of each event.

The inclusive analysis presented in this thesis is based on the selection of pairs of leptons from semileptonic B meson decays. In a semileptonic B decay the parent b quark emits a W boson which then decays into a lepton and a neutrino. The flavor of the parent B meson at decay time is revealed by the charge of the lepton (see Fig. 3.1).

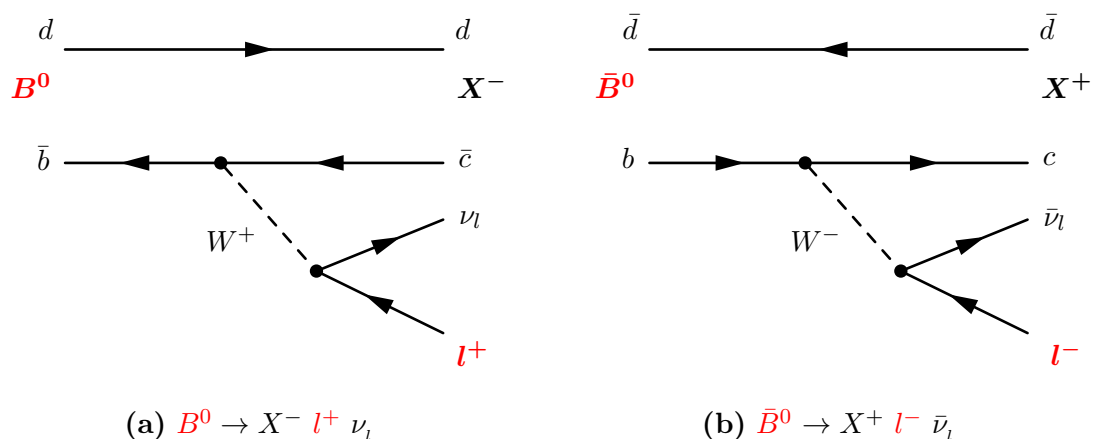


Figure 3.1.: Feynman diagrams for semileptonic B/\bar{B} decays: the charge of the lepton reveals the flavor of the parent B meson. Diagram (a) shows how a B^0 produces a positive lepton, while diagram (b) shows how a negative lepton is produced by a \bar{B}^0 .

Since semileptonic B decays are three-body decays, the energies E_l of the outgoing leptons in the B rest frame are spread over the whole allowed energy range

$$m_l \leq E_l \leq m_B - m_\nu - m_X \approx m_B - m_X \quad . \quad (3.2.1)$$

Additional criteria are needed to keep leptonic background from other particle decays (J/Ψ , Ψ' , $\Upsilon(nS)$, ...) under control.

There are three types of background which contribute to a sample of events:

1. **Secondary leptons** (e.g. from charmed meson decays). Since the mass of the charm quark is significantly less than the b mass, secondary leptons typically have lower momenta than primary leptons.
2. **Fake leptons:** hadrons which can be either primary decay products from B mesons or secondary products that mimic leptons. A proper setup of the particle identification devices on the software level of the detector should reduce contributions from fake leptons.

3. **Continuum events:** leptons or hadrons from non-resonant l^+l^- or $q\bar{q}$ production. The mass of the B meson results in an upper kinematic limit to the momenta of its decay products, the upper kinematic limit for continuum particle production is higher.

Using $|\vec{p}_{\text{cms}}|$ cuts for the leptons should reduce the background from secondary leptons and continuum events.

In order to get an idea how the dilepton spectra look like, the luminosity normalized invariant mass distribution

$$m_{ll'} = \sqrt{\left(\sum_l E_l\right)^2 - \left(\sum_l \vec{p}_l\right)^2} \quad (3.2.2)$$

of the dileptons was plotted for eight data samples with different \sqrt{s} (Fig. 3.2 - 3.9), for normalization see Eq. (3.2.6). The index ll' denotes every possible combination of electrons and muons, despite of their charge or their lepton flavor.

Noticable are the edges at ~ 4 GeV and ~ 8 GeV, which can be seen in all of the spectra. These edges are explained by two-photon QED background processes of the form $e^+e^- \rightarrow e^+e^-e^+e^- (+n\gamma)$ [36] and are related to the beam energies.

The enhancement at $m_{ll'} \approx 3.1$ GeV shows the J/ψ resonance. The zoom plots into the upper mass region show direct $\Upsilon(nS) \rightarrow \mu^+\mu^-$ decays (high energy e^+e^- pairs from $\Upsilon(nS) \rightarrow e^+e^-$ decays emit bremsstrahlung and therefore have a smaller invariant mass). The production of e.g. $\Upsilon(1S)$ can then originate from an initial state radiation process or from a decay of the form $\Upsilon(5S) \rightarrow \Upsilon(1S)\pi^+\pi^-$.

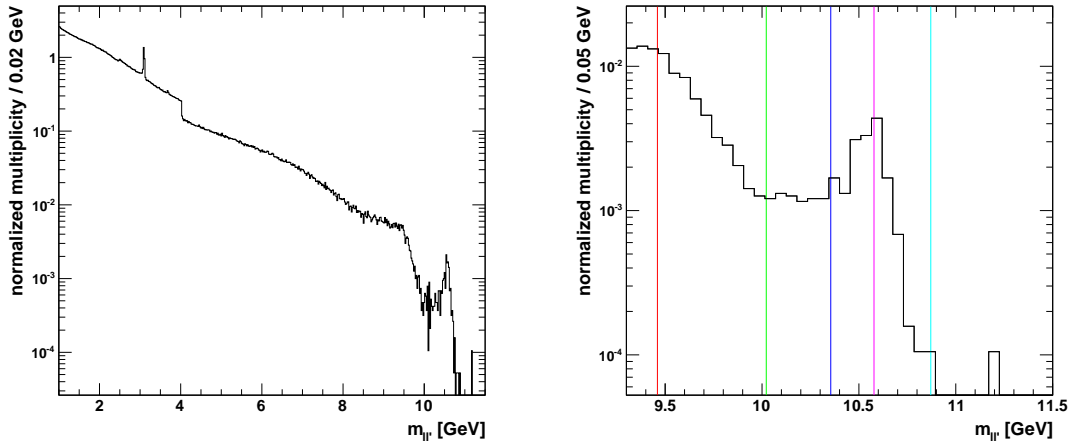


Figure 3.2.: Dilepton invariant mass spectrum of the $\Upsilon(4S)$ ($\sqrt{s} = 10.5779$ GeV) data sample. The right plot shows a zoom into the upper region of the mass spectrum, which is dominated by μ pairs, marked energies: $\Upsilon(1S)$, $\Upsilon(2S)$, $\Upsilon(3S)$, $\Upsilon(4S)$, $\Upsilon(5S)$.

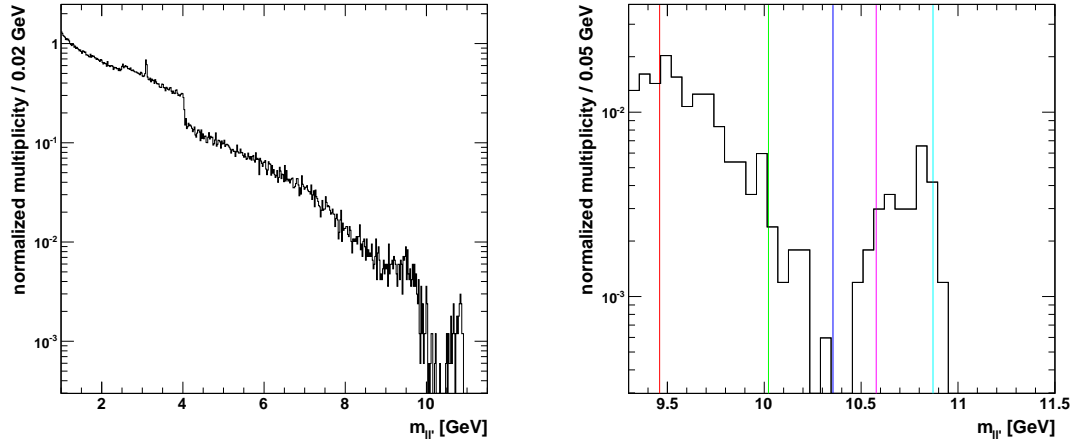


Figure 3.3.: Dilepton invariant mass spectrum of the $\sqrt{s} = 10.8275$ GeV data sample. The right plot shows a zoom into the upper region of the mass spectrum, which is dominated by μ pairs, marked energies: $\Upsilon(1S)$, $\Upsilon(2S)$, $\Upsilon(3S)$, $\Upsilon(4S)$, $\Upsilon(5S)$.

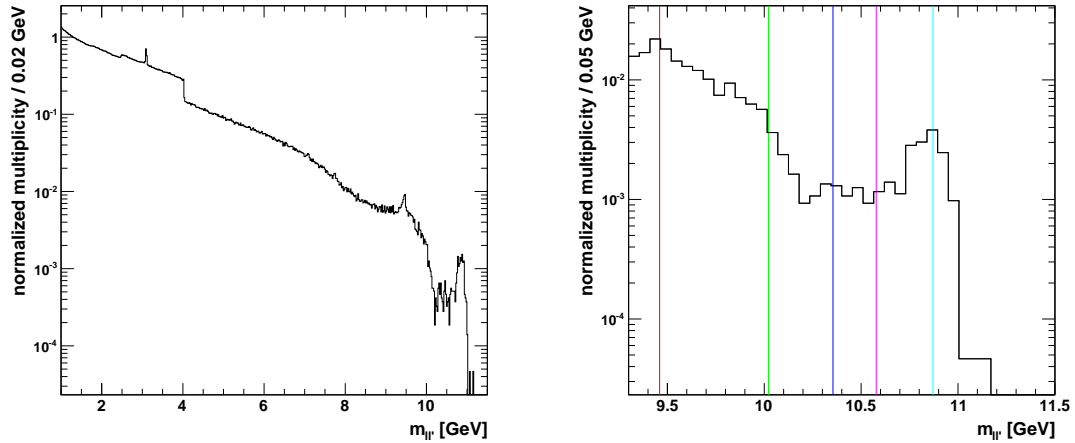


Figure 3.4.: Dilepton invariant mass spectrum of the $\Upsilon(5S)$ ($\sqrt{s} = 10.871$) GeV data sample. The right plot shows a zoom into the upper region of the mass spectrum, which is dominated by μ pairs, marked energies: $\Upsilon(1S)$, $\Upsilon(2S)$, $\Upsilon(3S)$, $\Upsilon(4S)$, $\Upsilon(5S)$.

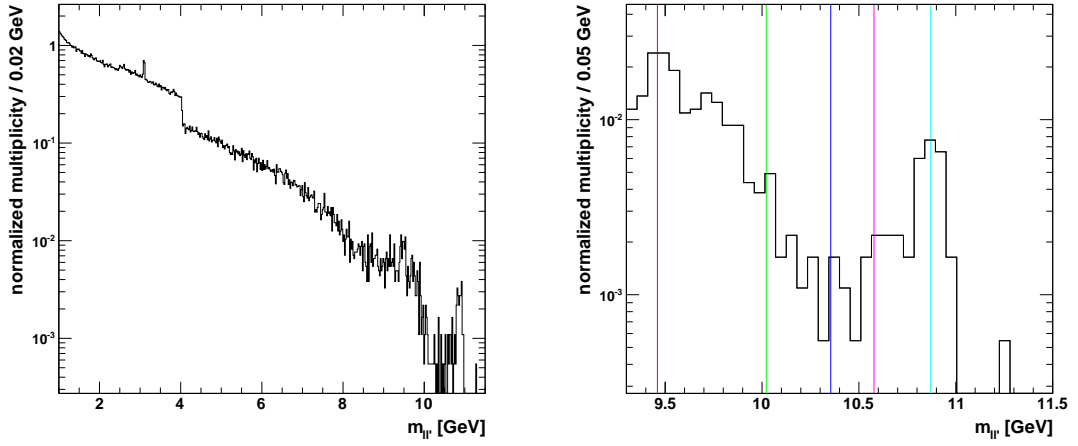


Figure 3.5.: Dilepton invariant mass spectrum of the $\sqrt{s} = 10.8825$ GeV data sample. The right plot shows a zoom into the upper region of the mass spectrum, which is dominated by μ pairs, marked energies: $\Upsilon(1S)$, $\Upsilon(2S)$, $\Upsilon(3S)$, $\Upsilon(4S)$, $\Upsilon(5S)$.

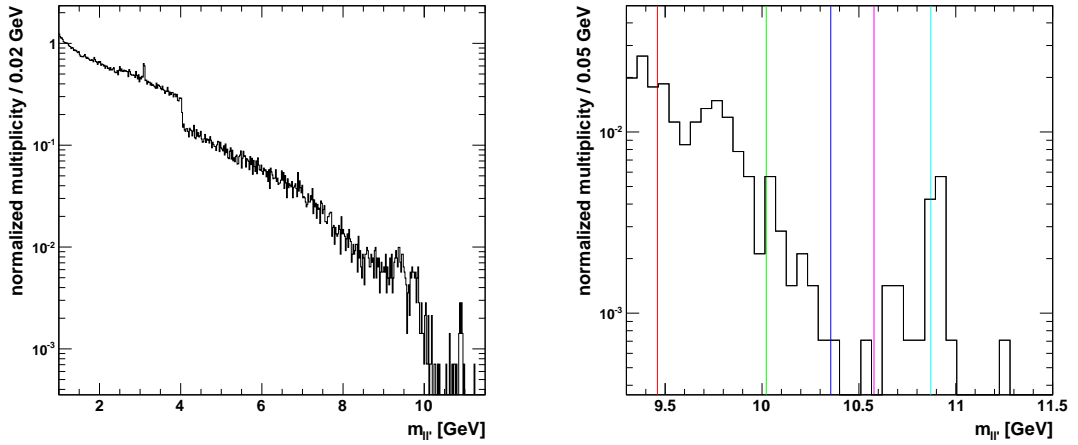


Figure 3.6.: Dilepton invariant mass spectrum of the $\sqrt{s} = 10.8975$ GeV data sample. The right plot shows a zoom into the upper region of the mass spectrum, which is dominated by μ pairs, marked energies: $\Upsilon(1S)$, $\Upsilon(2S)$, $\Upsilon(3S)$, $\Upsilon(4S)$, $\Upsilon(5S)$.

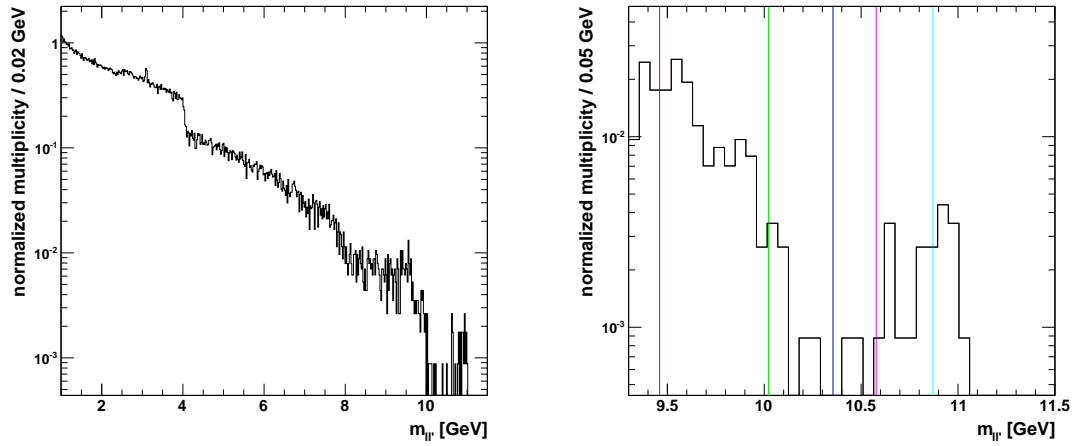


Figure 3.7.: Dilepton invariant mass spectrum of the $\sqrt{s} = 10.9275$ GeV data sample. The right plot shows a zoom into the upper region of the mass spectrum, which is dominated by μ pairs, marked energies: $\Upsilon(1S)$, $\Upsilon(2S)$, $\Upsilon(3S)$, $\Upsilon(4S)$, $\Upsilon(5S)$.

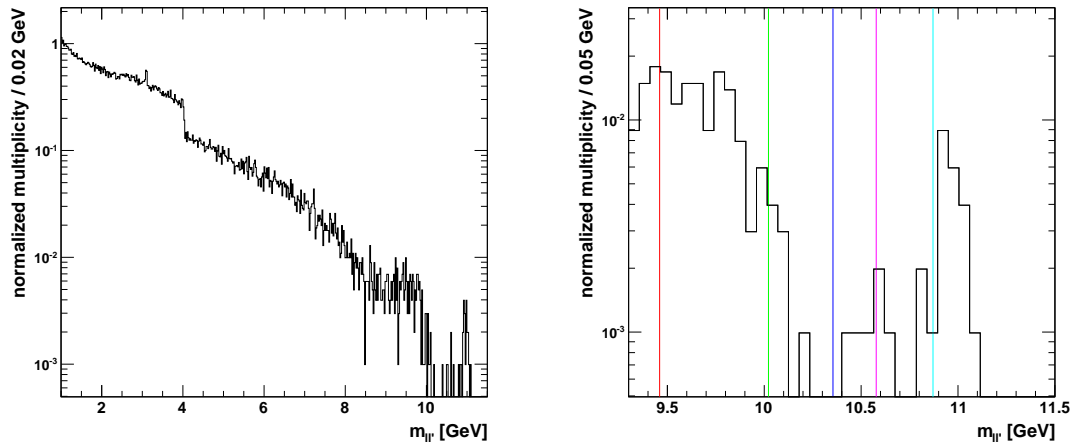


Figure 3.8.: Dilepton invariant mass spectrum of the $\sqrt{s} = 10.9575$ GeV data sample. The right plot shows a zoom into the upper region of the mass spectrum, which is dominated by μ pairs, marked energies: $\Upsilon(1S)$, $\Upsilon(2S)$, $\Upsilon(3S)$, $\Upsilon(4S)$, $\Upsilon(5S)$.

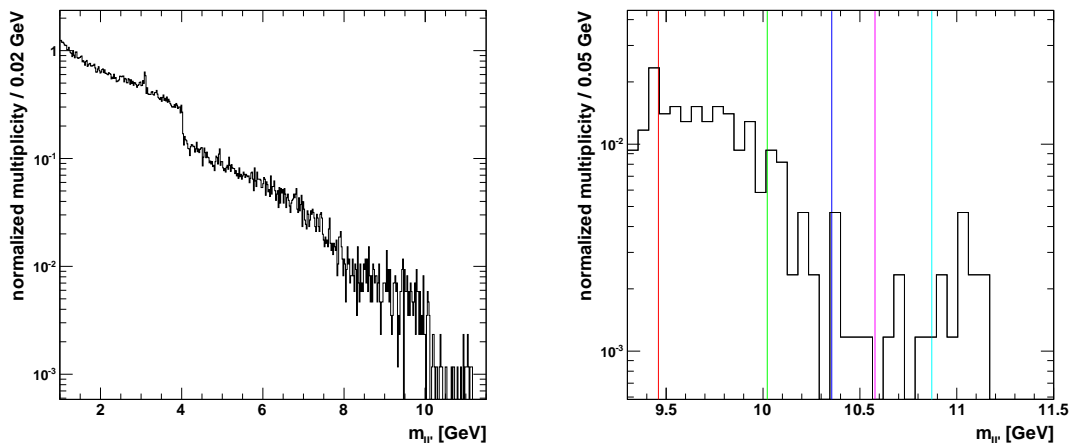


Figure 3.9.: Dilepton invariant mass spectrum of the $\sqrt{s} = 11.0175$ GeV data sample. The right plot shows a zoom into the upper region of the mass spectrum, which is dominated by μ pairs, marked energies: $\Upsilon(1S)$, $\Upsilon(2S)$, $\Upsilon(3S)$, $\Upsilon(4S)$, $\Upsilon(5S)$.

3.2.1. Dilepton Event Selection

If an event contains two or more lepton candidates, the analysis proceeds considering only the two leptons with the highest momentum in the center of mass system $|\vec{p}_{\text{cms}}|$. The CMS momentum of each lepton is required to meet

$$1.1 \text{ GeV} < |\vec{p}_{\text{cms}}| < 2.3 \text{ GeV} \quad . \quad (3.2.3)$$

These cuts were optimized for dilepton analysis from B decays in $\Upsilon(4S) \rightarrow B\bar{B}$ events in [37]. The lower cut reduces contributions from cascade or secondary (charm) decays, the upper cut reduces continuum contributions. Fig. 3.10 shows the momentum spectrum of the leptons, the applied cuts and a two dimensional plot, where the momentum spectrum is plotted against the invariant mass of the lepton pair.

Events which contain one or more J/ψ mesons can not be signal dilepton events. Therefore events in which J/ψ mesons can be reconstructed are rejected. The invariant mass of each candidate dilepton with oppositely charged tracks is calculated and if the invariant mass lies in the J/ψ region the event is rejected.

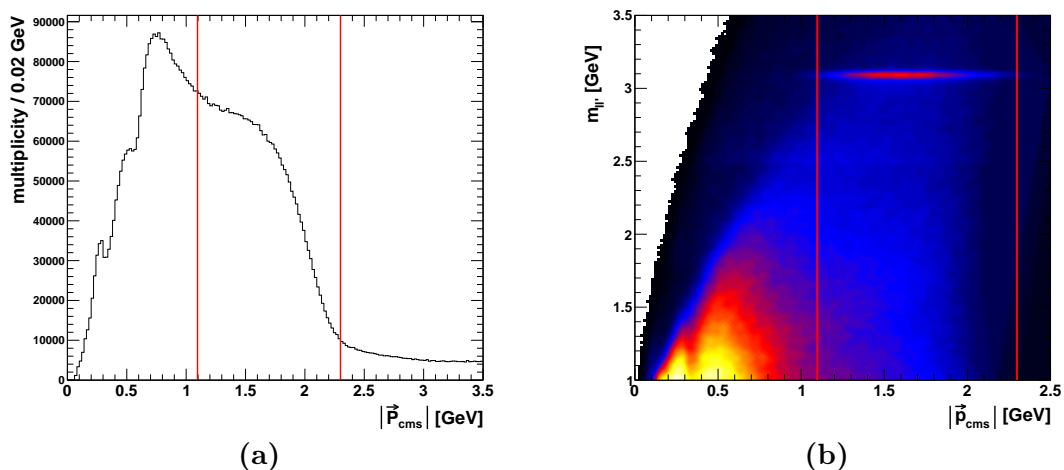


Figure 3.10.: Plot (a) shows the distribution of the lepton momenta from $\Upsilon(4S)$ data, plot (b) shows the momentum spectrum plotted against the invariant mass $m_{ll'}$ of the dilepton. The red lines indicate the edges of the momentum cuts. Plot (b) clearly points out the need for a J/ψ veto, since leptons from J/ψ decays lie directly in the allowed momentum range.

This region is defined as

$$-0.15 \text{ GeV} < (M_{e^+e^-} - M_{J/\psi}) < 0.05 \text{ GeV} \quad , \quad (3.2.4)$$

$$-0.05 \text{ GeV} < (M_{\mu^+\mu^-} - M_{J/\psi}) < 0.05 \text{ GeV} \quad . \quad (3.2.5)$$

The looser lower cut for the electron pair invariant mass is to reject J/ψ mesons whose calculated mass is low due to energy loss of the daughter electrons due to bremsstrahlung. Fig. 3.11 shows the J/ψ vetos for electrons and muons.

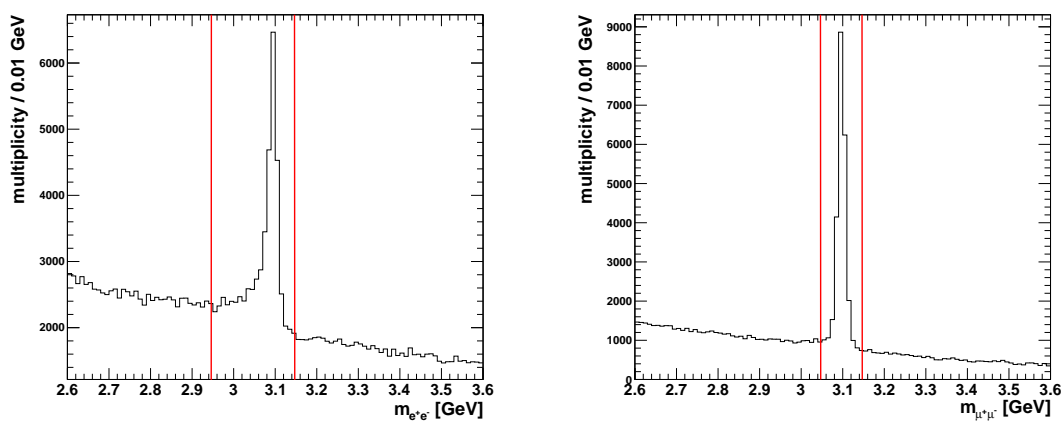


Figure 3.11.: The plot on the left shows the asymmetric J/ψ rejection region for e^+e^- pairs, the plot on the right shows the symmetric J/ψ veto in the $\mu^+\mu^-$ channel.

Furthermore it was required that the the ratio of the second and zero Fox-Wolfram moments R_2 is smaller than 0.8. Its value ranges from zero to one and its quantity is indicative of the collimation ("jettiness") of an event topology (closer to one); values of R_2 closer to zero indicate a more spherical event.

No further cuts were applied, although one could think of additional angle cuts on θ to reduce background (e.g. continuum events are more jet-like whereas signal events have a more spherical distribution), but due to the changing kinematics in the scan, this was not applied. The cuts were applied and tested with the large $\Upsilon(4S)$ dataset. With a branching fraction $> 96\%$ $\Upsilon(4S)$ decays into $B\bar{B}$ ($= B^0\bar{B}^0, B^+B^-$). In the case of neutral B meson production one should see $B - \bar{B}$ oscillation, since neutral B mesons oscillate between their matter and their antimatter forms (see Fig. 3.12).

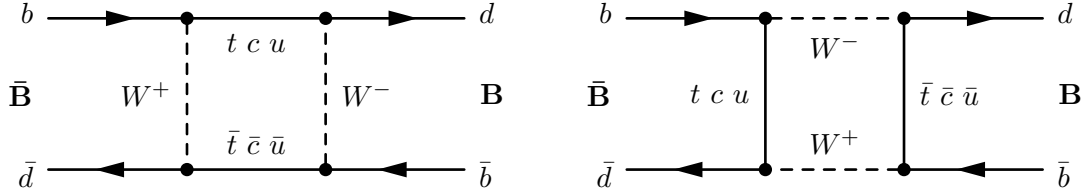


Figure 3.12.: $B - \bar{B}$ oscillation scheme: By the exchange of W bosons and heavy quarks B mesons oscillate between their matter and antimatter forms.

As long as both B mesons live, they oscillate in phase since both mesons are entangled and build a non-localized quantum system. If one B meson has decayed, the other one still oscillates until it decays. By measuring the production vertex of the leptons ($=$ decay vertex of the B) one can measure Δz , the difference of the decay vertices of both B mesons. An opposite sign signal dilepton (OS) occurs when the two B mesons decay in their original flavor form. Since the charge of the lepton reveals the flavor of the mother B meson, a same sign signal dilepton (SS) occurs when the remaining B meson oscillates into its antimatter form before it decays. By calculating the ratio

$$\frac{OS - SS}{OS + SS}$$

and plotting it in dependence of Δz , one should see an oscillation, since the oscillation probability rises with increasing Δz .

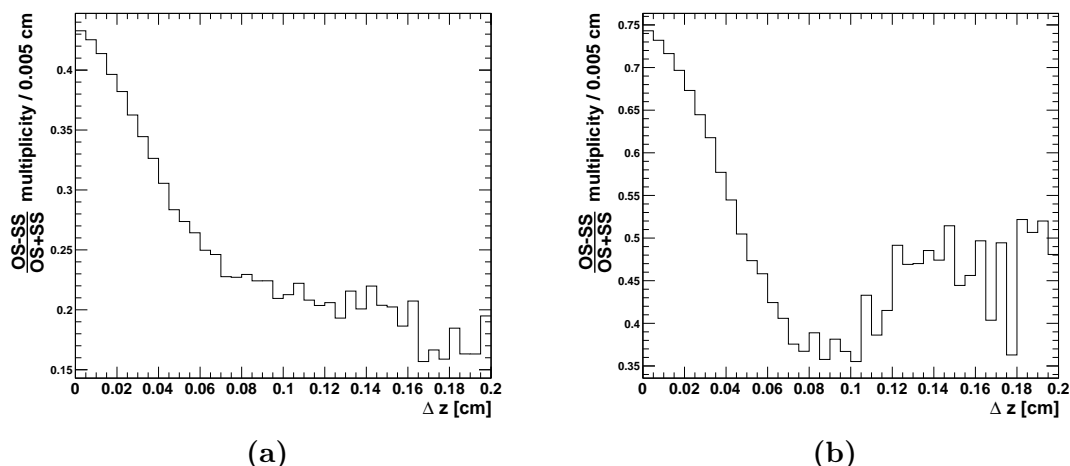


Figure 3.13.: Plot (a) shows $(OS-SS)/(OS+SS)$ plotted in dependence of Δz before the application of the cuts, no oscillation occurs. After the application of the cuts, plot (b) reveals a significant oscillation in B/\bar{B} meson decays.

The oscillation signal in Fig. 3.13 proves the efficiency of the momentum cuts, since the momentum cuts reveal the oscillation and enhance the contribution from primary B decay leptons. Such a clean B oscillation signal can only be seen in $\Upsilon(4S)$ decays, since in the $\Upsilon(5S)$ case the available phase space allows much more decay channels ($B^*\bar{B}$, $B\bar{B}\pi^0$, $B_s\bar{B}_s$, ...) and thus is a dirtier environment as in the $\Upsilon(4S)$ case.

The efficiency of the cuts was also tested for different decay channels. For this purpose MC studies with different decay channels were done (Tab. A.1) with the result that there is no significant decay channel dependence of the momentum cut efficiency, v.i.z. such an inclusive analysis does not prefer or penalize any decay channel and therefore is appropriate to search for new states without favoring any decay channel.

3.2.2. Results on Dilepton Production in Dependence of \sqrt{s}

At first a simple approach was made: the comparison of the number of measured signal dileptons in dependence of \sqrt{s} . Such an approach would not reveal the actual decay channel, but at least it could give hints for new states. Due to different integrated luminosities in the energy scan, a normalization of the data has to be made in order to have comparable results in such an analysis. The normalization for each data point was chosen as

$$\text{normalized counts} = \frac{\text{total counts}}{\int \mathcal{L} dt [\text{pb}^{-1}]} \quad . \quad (3.2.6)$$

Analysing and comparing data from different center of mass energies leads to another problem: In an $\Upsilon(4S)$ decay the $B\bar{B}$ pair is created approximately at rest, because the $\Upsilon(4S)$ mass is right above the $B\bar{B}$ threshold. In an energy scan with growing \sqrt{s} above

the $\Upsilon(4S)$ resonance this condition is not valid anymore since the additional energy in the CMS will increase the kinetic energy of the B mesons in the center of mass frame. This also changes the lepton momenta and the cuts should be adjusted. Fig. 3.10b shows the J/ψ lying directly in the allowed momentum region. Increasing \sqrt{s} should therefore also increase the momenta of the leptons coming from J/ψ decays. Hence an analysis of the momentum changes of J/ψ leptons in dependence of \sqrt{s} could be used to adjust the momentum cuts. The momentum spectra from J/ψ leptons from data with different \sqrt{s} showed no significant change of the observed momenta (see section A.2), hence an adjustment of the momentum cuts cannot be justified. To take into account the change of the lepton momenta (even though it is not significant in the J/ψ data), a correction factor was introduced leading to a final normalization

$$\text{normalized counts} = \frac{\text{total counts}}{\int \mathcal{L} dt [\text{pb}^{-1}]} \cdot \Xi \quad , \quad (3.2.7)$$

where $\Xi \geq 1$ is the correction factor.

For the estimation of Ξ , Monte Carlo studies were made to correct for the systematic error when the momentum cuts remain unchanged. The spectra of the lepton momenta from semileptonic B decays were exemplarily examined for five energy values (see section A.3). The total number of dileptons in relation to the number of dileptons after the momentum cuts lets us calculate the correction factor Ξ to account for the rising momenta of the leptons. The Ξ values for the data points are normalized to the $\Upsilon(4S)$ value of $\Xi_{\Upsilon(4S)} = 1$.

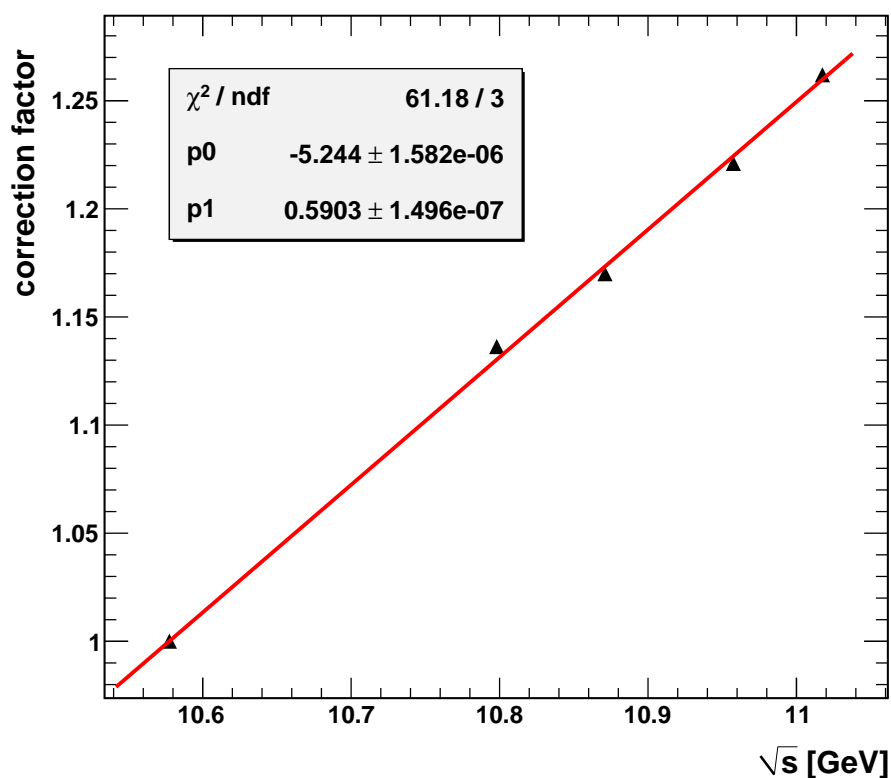
\sqrt{s} [GeV]	$\frac{\text{total counts}}{\text{counts after cuts}}$	normalized Ξ
$\Upsilon(4S)(10.5779)$	1.725	1
10.7985	1.960	1.136
$\Upsilon(5S)(10.871)$	2.018	1.170
10.9575	2.106	1.221
$\Upsilon(6S)(11.0175)$	2.177	1.262

Table 3.1.: MC results for the correction factor Ξ .

In order to obtain values for all scan points and to reduce statistical errors, a linear fit was performed, leading to the final values for Ξ (Fig. 3.14 and Tab. 3.2). The Ξ value for $\Upsilon(4S)$ was fixed to 1, since the momentum cuts were optimized for $\Upsilon(4S)$ data. The fit yielded

$$y = p_0 + p_1 \cdot x = -5.244 + 0.5903 \cdot x \quad . \quad (3.2.8)$$

\sqrt{s} [GeV]	Ξ	\sqrt{s} [GeV]	Ξ
$\Upsilon(4S)(10.5779)$	1	10.8895	1.184
10.7985	1.130	10.8975	1.189
10.8275	1.147	10.9275	1.207
10.8525	1.162	10.9575	1.224
$\Upsilon(5S)(10.871)$	1.173	10.9875	1.242
10.8825	1.180	$\Upsilon(6S)(11.0175)$	1.260

 Table 3.2.: Final values for the correction factor Ξ .

 Figure 3.14.: A linear fit to obtain the values for Ξ .

The data points for $\Upsilon(1S)$, $\Upsilon(2S)$ and $\Upsilon(3S)$ have no correction factor and are considered for background contributions only, since the $B\bar{B}$ channel is not open yet and therefore the dileptons must come from secondary decays or continuum lepton production. Fig. 3.15 shows the signal dilepton yields in dependence of the center of mass energy, a zoom into the interesting region between $\sqrt{s} = 10.7985$ GeV and $\sqrt{s} = 11.0175$ GeV in the $l'l'$ and in the $e\mu$ channel can be seen in Fig. 3.16 and in Fig. 3.17. The plots for $l'l'$ and $e\mu$ look very similar, nevertheless $e\mu$ should be the cleaner channel, since there is no background from other mesons than J/ψ which decay into

l^+l^- . For that reason the $e\mu$ channel is exclusively chosen in this inclusive dilepton analysis.

In order to understand the signal a fit with the contributions from $\Upsilon(4S)$, $\Upsilon(5S)$ and $\Upsilon(6S)$ was performed. The fit function was chosen to be a superposition of three Breit-Wigner curves:

$$f = \left| A_{nr} \right|^2 + \left| A_0 + A_{\Upsilon 4S} \exp [i\phi_{\Upsilon 4S}] \cdot \text{BW}(\mu_{\Upsilon 4S}, \Gamma_{\Upsilon 4S}) + A_{\Upsilon 5S} \exp [i\phi_{\Upsilon 5S}] \cdot \text{BW}(\mu_{\Upsilon 5S}, \Gamma_{\Upsilon 5S}) + A_{\Upsilon 6S} \exp [i\phi_{\Upsilon 6S}] \cdot \text{BW}(\mu_{\Upsilon 6S}, \Gamma_{\Upsilon 6S}) \right|^2, \quad (3.2.9)$$

with the Breit-Wigner function

$$\text{BW}(\mu, \Gamma) = \frac{1}{(E^2 - \mu^2) + i\mu\Gamma}. \quad (3.2.10)$$

This kind of fit function was also used in a recent BaBar paper [38]. Each of the resonances was given an amplitude A_{Υ_i} , a phase ϕ_{Υ_i} , a Breit-Wigner mean value μ_{Υ_i} and a Breit-Wigner width Γ_{Υ_i} , A_0 and A_{nr} describe non-resonant background.

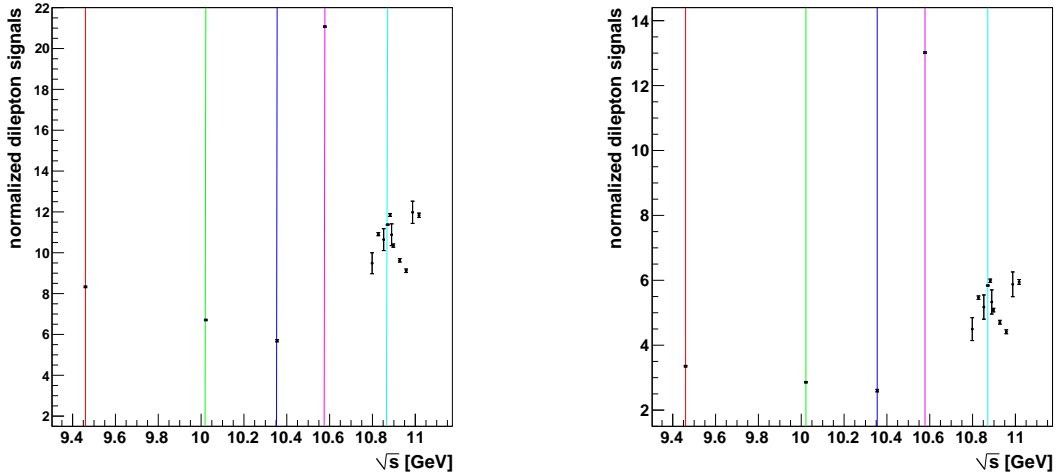


Figure 3.15.: Normalized dilepton counts as a function of \sqrt{s} , the left plot shows the counts in the $l'l'$ channel, whereas the right plot shows the signal dileptons in the $e\mu$ channel; marked energies: $\Upsilon(1S)$, $\Upsilon(2S)$, $\Upsilon(3S)$, $\Upsilon(4S)$, $\Upsilon(5S)$.

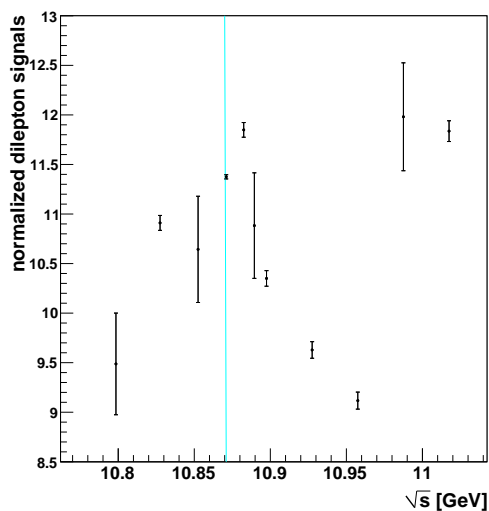


Figure 3.16.: Zoom into the data points between $\sqrt{s} = 10.7985$ GeV and $\sqrt{s} = 11.0175$ GeV (ll' channel)

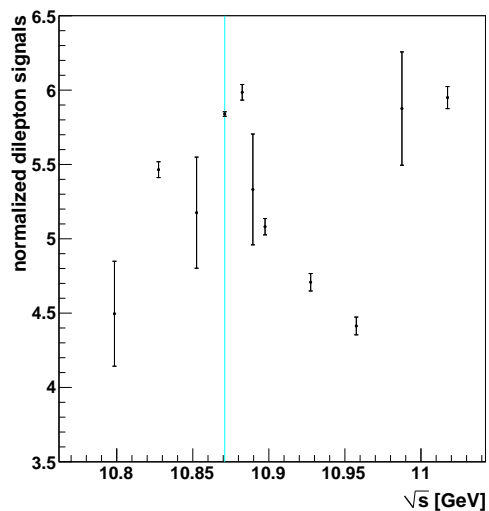


Figure 3.17.: Zoom into the data points between $\sqrt{s} = 10.7985$ GeV and $\sqrt{s} = 11.0175$ GeV ($e\mu$ channel)

Since we only have one data point for $\Upsilon(4S)$ and only two data points for the assignation of the $\Upsilon(6S)$ line shape, the parameters of $\Upsilon(4S)$ were fixed to the pdg values in [15] and the values for the $\Upsilon(6S)$ line shape were fixed to the values from BaBar measurements [38]. The measurements in [38] did not consider a phase from $\Upsilon(4S)$, therefore the phase for $\Upsilon(6S)$ is not fixed to this measurement, since the additional $\Upsilon(4S)$ phase has an impact on the phases of $\Upsilon(5S)$ and $\Upsilon(6S)$. The fit can be seen in Fig. 3.18 and Fig. 3.19, the obtained parameters can be seen in Tab. 3.3. This inclusive dilepton method for determining the $\Upsilon(5S)$ line shape is of course not competitive with direct scan methods, but at least the obtained results show that it is a powerful method for determining B meson production. Fig. 3.19 gives first evidence for $B\bar{B}$ production in $\Upsilon(6S)$ decays. Hardly explainable is the dilepton yield at $\sqrt{s} = 10.8525$ GeV, which is evidently below the expected value from the fit. The high dilepton yield at $\sqrt{s} = 10.8825$ GeV may be explained by a shifting of the position of the $\Upsilon(5S)$ peak, since other measurements with direct scan methods [38] determine the $\Upsilon(5S)$ peak lying around $\sqrt{s} = 10.88$ GeV.

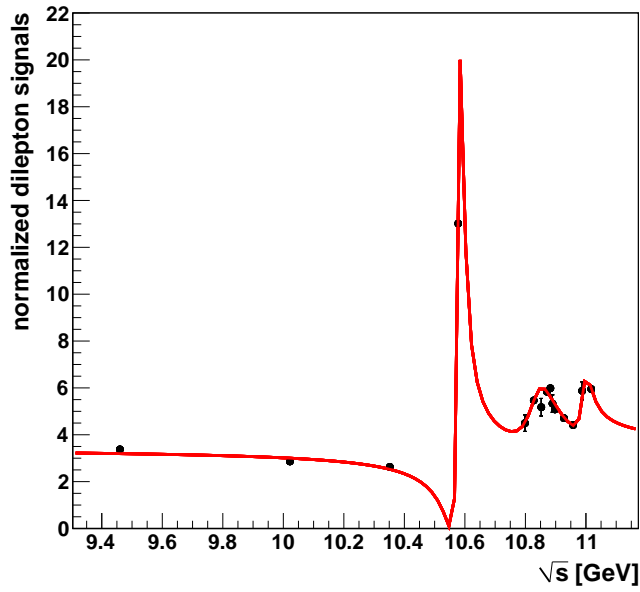


Figure 3.18.: Fit results for the normalized dilepton signal. The parameters of $\Upsilon(4S)$ were fixed to the pdg values, the line shape of $\Upsilon(6S)$ was fixed to the results from BaBar measurements.

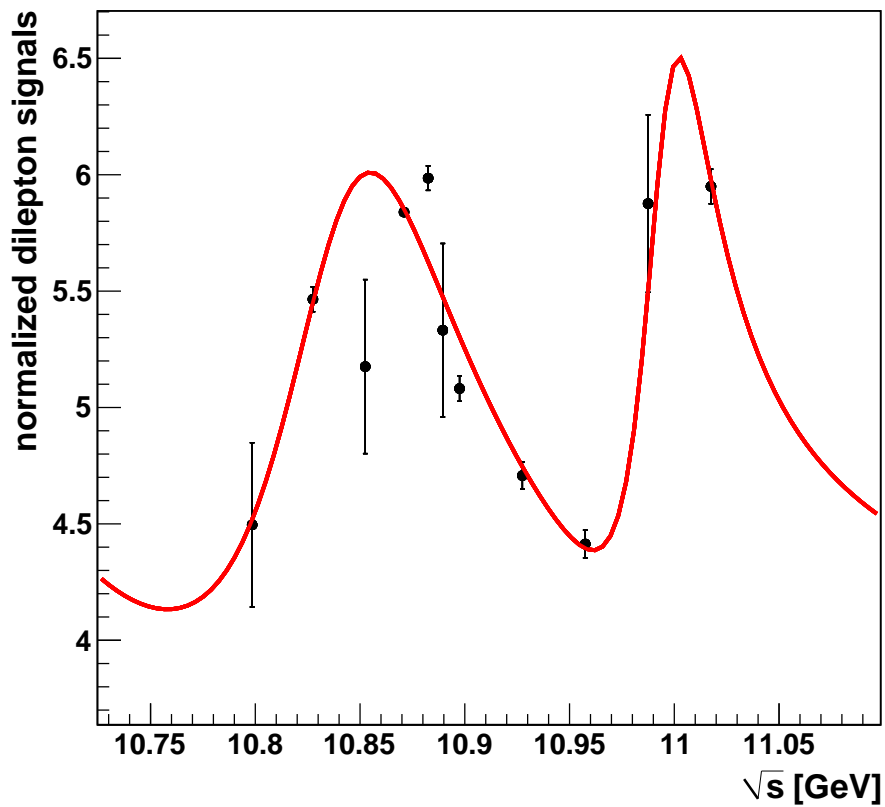


Figure 3.19.: Fit results zoomed into the region between $\sqrt{s} = 10.7985$ GeV and $\sqrt{s} = 11.0175$ GeV

parameter	fit results	constraints
A_{nr}	0 ± 0.517	–
A_0	1.854 ± 0.008	–
$A_{\Upsilon_{4S}}$	1.114 ± 0.263	$[0; \infty)$
$\phi_{\Upsilon_{4S}}$	0.0445 ± 0.5513 rad	$[-2\pi; 2\pi]$ rad
$\mu_{\Upsilon_{4S}}$	10.581 ± 0.002 GeV	10.5794 ± 0.0012 GeV
$\Gamma_{\Upsilon_{4S}}$	23 ± 3.1 MeV	20.5 ± 2.5 MeV
$A_{\Upsilon_{5S}}$	5.032 ± 0.425	$[0; \infty)$
$\phi_{\Upsilon_{5S}}$	-1.511 ± 0.066 rad	$[-2\pi; 2\pi]$ rad
$\mu_{\Upsilon_{5S}}$	10.838 ± 0.007 GeV	$[10.8; 10.95]$ GeV
$\Gamma_{\Upsilon_{5S}}$	106 ± 9 MeV	$[0; 500]$ MeV
$A_{\Upsilon_{6S}}$	0.252 ± 0.0182	$[0; \infty)$
$\phi_{\Upsilon_{6S}}$	-0.077 ± 0.125 rad	$[-2\pi; 2\pi]$ rad
$\mu_{\Upsilon_{6S}}$	10.994 ± 0.0008 GeV	10.996 ± 0.002 GeV
$\Gamma_{\Upsilon_{6S}}$	40 ± 6 MeV	37 ± 3 MeV

Table 3.3.: Fit results and parameter constraints

A comparison of the obtained fit results with these BaBar measurements and with the official pdg values can be seen in Tab. 3.4.

parameter	fit result	BaBar result	pdg ₂₀₀₈ value
$\phi_{\Upsilon_{5S}}$	-1.511 ± 0.066 rad	2.11 ± 0.12 rad	–
$\mu_{\Upsilon_{5S}}$	10.838 ± 0.007 GeV	10.876 ± 0.002 GeV	10.865 ± 0.008 GeV
$\Gamma_{\Upsilon_{5S}}$	106 ± 9 MeV	43 ± 4 MeV	110 ± 13 MeV

 Table 3.4.: Comparison of the obtained $\Upsilon(5S)$ fit results with measurements from BaBar and with the value from the particle data group

The phase difference between the fit result and the BaBar measurement can be explained with the additional consideration of $\phi_{\Upsilon_{4S}}$. The differences in μ and Γ cannot be explained, but in that case the BaBar result should give the better values since it used direct scan methods to determine the $\Upsilon(5S)$ line shape. Nevertheless the fit result of $\Gamma_{\Upsilon_{5S}}$ is closer to the world average value from the particle data group than the result from BaBar.

3.3. Analysis of $B^{(*)}\bar{B}^{(*)}\pi^0$ Events

As mentioned in 1.4 additional pions are needed to obtain quantum numbers $J^{PC} = 1^{+\pm}$. The simplest case would be the production of one additional π^0 . The threshold for a reaction $e^+e^- \rightarrow B^0\bar{B}^0\pi^0$ lies at $2M(B^0) + M(\pi^0) = 10.694$ GeV.

3.3.1. π^0 Selection

The measurement of low energy neutral pions is nontrivial, since they immediately decay into two soft photons (BR $\approx 100\%$), which do not leave a track in the detector and can only be measured by their energy deposition and their shower shapes inside the electromagnetic calorimeter. By reconstruction of the shower's center of gravity the four-vectors of the photons can be reconstructed, fit procedures help to pick out possible π^0 candidates. This complex reconstruction can cause uncertainties in the measurement of the properties of the pions. There is no way to determine the decay vertex of a neutral pion, so the only information to work with is the reconstructed four-vector of the π^0 . The following criteria have to be fulfilled to obtain a π^0 signal:

1. $E_{\gamma_1}, E_{\gamma_2}|_{\text{LAB}} > 70 \text{ MeV}$
2. $|\cos(\sphericalangle(\gamma_1, \gamma_2)_{\text{LAB}})| < 0.9$ [39]
3. $\sphericalangle(\gamma_1, \gamma_2)|_{\pi^0 \text{ rest frame}} > 174^\circ$
4. $\chi^2 < 5$.

The cut on the laboratory angle between the photons reduces the number of neutral pions which are detected in the endcap, where the ECL performance is usually worse than in the barrel section. Fig. 3.20 shows the $\sphericalangle(\gamma_1, \gamma_2)_{\text{LAB}}$ distribution of the π^0 candidates. In the pion rest frame the decay photons should have an angle of 180° between them due to momentum conservation; the limited reconstruction efficiency is taken into account by demanding the angle between the photons to be larger than 174° , the distribution of the angle between the photons from π^0 candidates in the π^0 rest frame can be seen in Fig. 3.21. The χ^2 cut sets demands on the quality of the π^0 fit procedure. Additionally the maximum number of neutral pion candidates in one event was set to a limit of 50, events with a larger number are rejected.

There is no simple way to discriminate $B\bar{B}$ from $B\bar{B}\pi^0$ events, because without exclusive reconstruction there is no way to discriminate primary pions from $e^+e^- \rightarrow B\bar{B}\pi^0$ events from secondary pions which come from other particle decays. What one can do is to calculate constraints for the π^0 momentum coming from the limited phase space. Assuming that the $B^{(*)}$ mesons build a mesonic molecule X_b (and the γ for $J^{PC} = 1^{++}$ quantum numbers is created "at rest"), the momentum constraints for the π^0 have to be calculated in two-body decay kinematics (see C.1) using the formula

$$|\vec{p}_{\text{cms}}(\pi^0)| = |\vec{p}_{\text{cms}}(X_b)| = \frac{\sqrt{(\sqrt{s}^2 - (m_1 + m_2)^2)(\sqrt{s}^2 - (m_1 - m_2)^2)}}{2\sqrt{s}}, \quad (3.3.1)$$

with $m_1 = m(B) + m(B^*) = 10.604 \text{ GeV}$ ¹ and $m_2 = m(\pi^0) = 0.13498 \text{ GeV}$.

\sqrt{s} [GeV]	$ \vec{p}_{\text{cms}}(\pi^0) $ [GeV]	\sqrt{s} [GeV]	$ \vec{p}_{\text{cms}}(\pi^0) $ [GeV]
10.7985	0.13875	10.8895	0.2482
10.8275	0.1762	10.8975	0.2570
10.8525	0.2062	10.9275	0.2896
10.8675	0.2235	10.9575	0.3214
10.871	0.2275	10.9875	0.3526
10.8825	0.2404	11.0175	0.3834

Table 3.5.: Constraints of the π^0 momenta due to limited phase space.

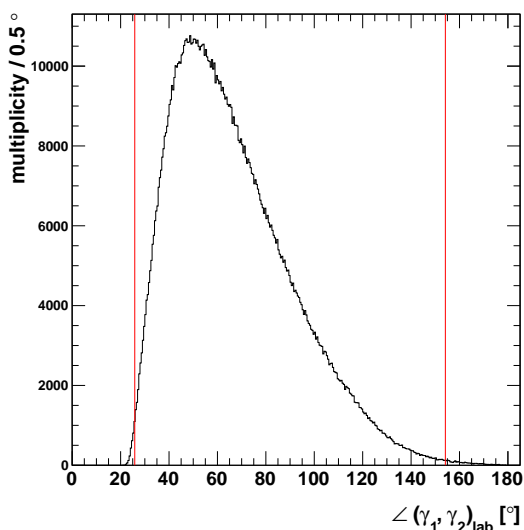


Figure 3.20.: $\angle(\gamma_1, \gamma_2)_{\text{LAB}}$ from π^0 candidates, the red lines indicate the allowed angle regions

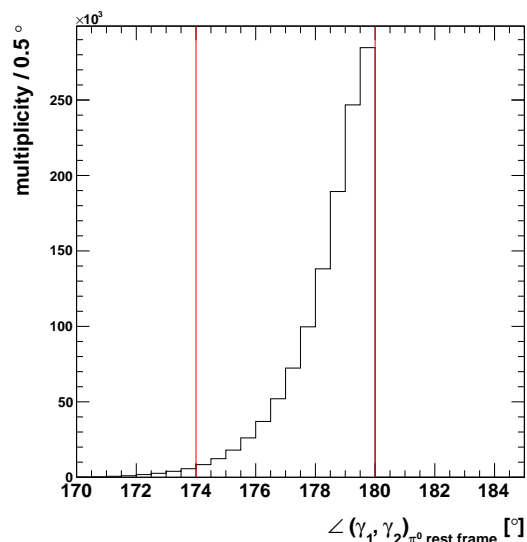


Figure 3.21.: Distribution of the angle between the photons from π^0 candidates in the π^0 rest frame

The threshold for $B^0 \bar{B}^{*0} \pi^0$ lies at $m_1 + m_2 = 10.739 \text{ GeV}$. The calculated upper limits on the π^0 momentum are listed in Tab. 3.5. For a fixed mass of the X_b the kinematics is also fixed, but since m_{X_b} is not known, these constraints build an upper limit for the π^0 momentum, the heavier the X_b is, the smaller the π^0 momentum will

¹**Note:** A binding energy in the $B^0 \bar{B}^{*0}$ system could lower the mass of a bound $B^0 \bar{B}^{*0}$ state, this is not considered in the calculation since the uncertainty on the π^0 energy is in the region of a possible binding energy ($\mathcal{O}(\text{MeV})$), see also Fig. 3.25.

be. The lower limit reads zero in case the X_b is so heavy that both particles (X_b and π^0) are created at rest.

In order to understand the low momentum π^0 background from secondary particle decays, Monte Carlo studies of the $|\vec{p}_{\text{cms}}(\pi^0)|$ distribution from K^* , ρ and D decays were made. Additionally the momenta from primary pions from $\Upsilon(5S) \rightarrow B^0\bar{B}^0\pi^0$ were plotted for comparison. These distributions of the low momentum pions can be seen in Fig. 3.22. The plots all look quite alike, which confirms that one cannot distinguish primary from secondary pions. The upper limit of the primary π^0 momentum from $B^0\bar{B}^0\pi^0$ events due to limited phase space is conspicuous.

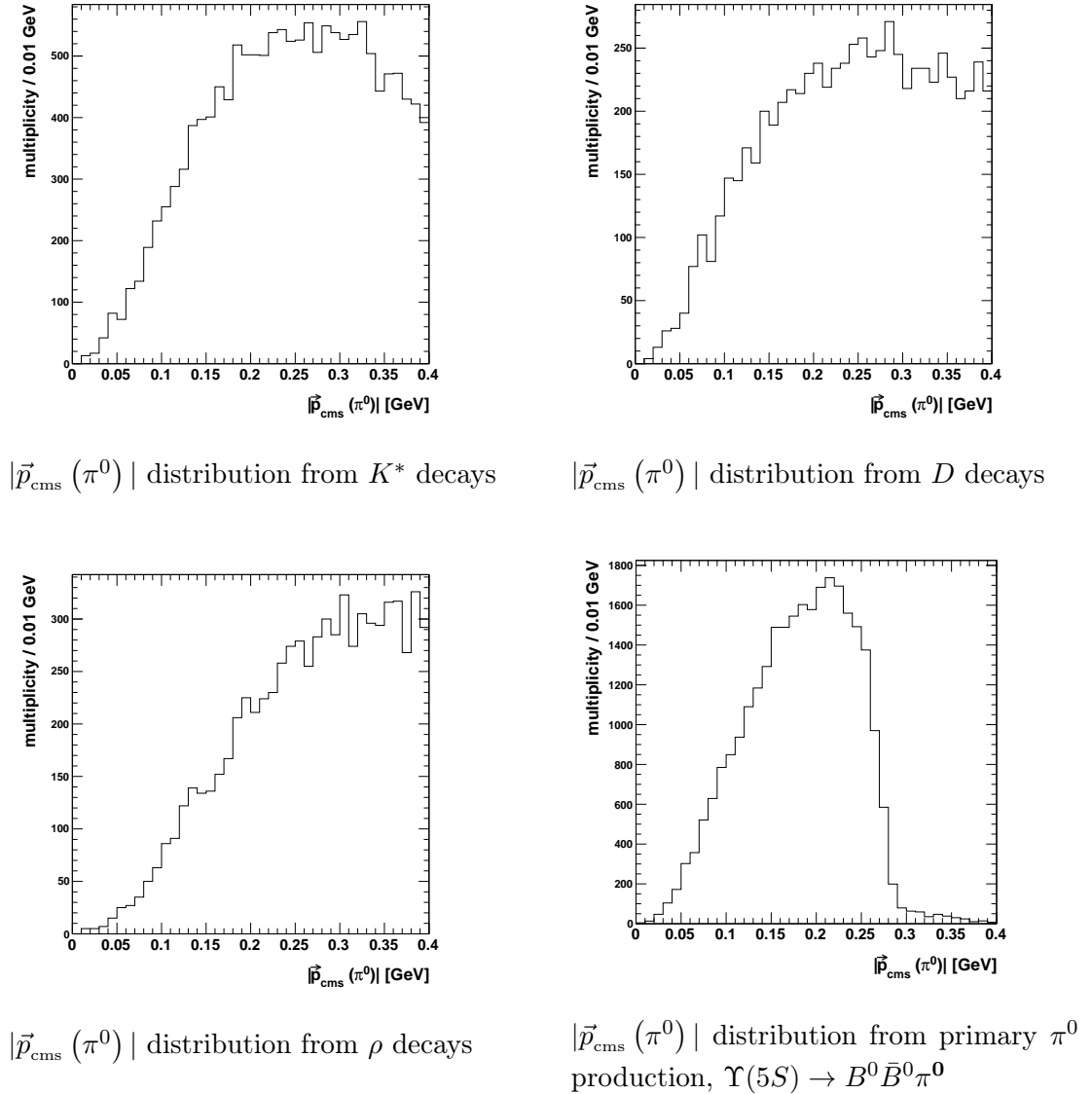


Figure 3.22.: Monte Carlo simulations: Low momentum π^0 distribution from K^* (upper left), ρ (lower left) and D decays (upper right). All distributions look similar. The plot on the lower right shows the primary π^0 momentum distribution from $B\bar{B}\pi^0$ events.

3.3.2. Results on $B^{(*)}\bar{B}^{(*)}\pi^0$ events

After examining the pions in detail one comes to the question how to search for new states with such an highly inclusive analysis. One could examine the number of signal pions which meet all the criteria mentioned in 3.3.1 under the condition that a dilepton signal as described in section 3.2.1 is found. Such a spectrum should be dominated by $B^{*0}\bar{B}^{*0}\pi^0$ (threshold energy: 10.7852 GeV) and $B_s^*\bar{B}_s^*\pi^0$ (threshold energy: 10.9606 GeV) signals, since $\Upsilon(5S)$ decays are dominated by $B^{*0}\bar{B}^{*0}$ ($f_{B^{*0}\bar{B}^{*0}} \approx 37\%$ [40]) and $B_s^*\bar{B}_s^*$ ($f_{B_s^*\bar{B}_s^*} \approx 90\%$ [41]) production. Such an analysis can be seen in Fig. 3.23. The contributions from the dominating $B^{*0}\bar{B}^{*0}\pi^0$ and $B_s^*\bar{B}_s^*\pi^0$ processes were fitted with an exponential function of the form

$$\begin{aligned}
 f = & A \cdot \left(1 - \exp \left[-B \cdot \left(\sqrt{s} - m(B^{*0}\bar{B}^{*0}\pi^0) \right) \right] \right) \Theta \left(\sqrt{s} - m(B^{*0}\bar{B}^{*0}\pi^0) \right) \\
 & + C \cdot \left(1 - \exp \left[-D \cdot \left(\sqrt{s} - m(B_s^*\bar{B}_s^*\pi^0) \right) \right] \right) \Theta \left(\sqrt{s} - m(B_s^*\bar{B}_s^*\pi^0) \right) ,
 \end{aligned}
 \tag{3.3.2}$$

with $\Theta(\sqrt{s})$ being the theta step function and A , B , C and D being the fit parameters. Such a fit function was also used in [42] and is based on experience mainly. The deviation from the fit around $\sqrt{s} = 10.88$ GeV can be explained by the high B meson production rates around the $\Upsilon(5S)$ resonance (see also Fig. 3.19). The fit results are given in Tab. 3.6.

parameter	fit result
A	0.8 ± 0.00018
B	27 ± 0.024
C	0.7298 ± 0.052
D	25 ± 12.61

Table 3.6.: Fit results from the fit in Fig. 3.23.

Unfortunately this method has a problem: with rising \sqrt{s} the constraints for the π^0 momenta get looser and more and more secondary pions lie inside the allowed momentum range, an analysis with such a method is therefore not significant for searching new states.

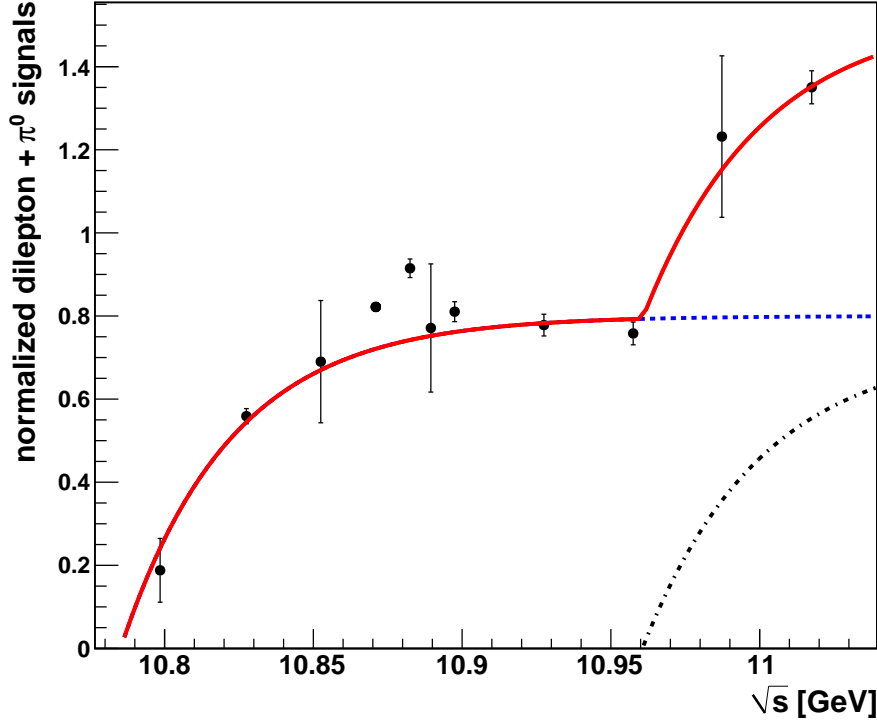


Figure 3.23.: Fit of the dilepton + π^0 signals in dependence of \sqrt{s} . The complete fit is drawn in red, the dashed blue line represents the contribution from $B^{*0}\bar{B}^{*0}\pi^0$ events and the black dashed-dotted line shows the contribution from $B_s^*\bar{B}_s^*\pi^0$ production.

The only way to analyze such events with significant results is to examine the recoilmass of the π^0 . The recoilmass is defined as

$$m_r = \sqrt{\left(\sum_{\text{initial}} E - \sum_{\text{final}} E\right)^2 - \left(\sum_{\text{final}} \vec{p}\right)^2} . \quad (3.3.3)$$

The dilepton signal is used as an indicator for $B\bar{B}$ production only, the energy of the leptons is not taken into account. Therefore Eq. (3.3.3) simplifies to

$$m_r(\pi^0) = \sqrt{\left(\sqrt{s} - E_{\text{cms}}(\pi^0)\right)^2 - \left(\vec{p}_{\text{cms}}(\pi^0)\right)^2} . \quad (3.3.4)$$

Secondary pions should have a relatively flat recoilmass distribution, but the primary pions should have a peak if there is a new state which decays into B mesons. The results of a Monte Carlo simulation of the π^0 recoilmass distribution without a new state (**a**) and with the assumption there was a new particle with an arbitrarily chosen mass of 10.65 GeV (**b** and **c**) can be seen in Fig. 3.24. The new state is clearly visible in the π^0 recoilmass, therefore such an analysis is a powerful tool for discovering new states.

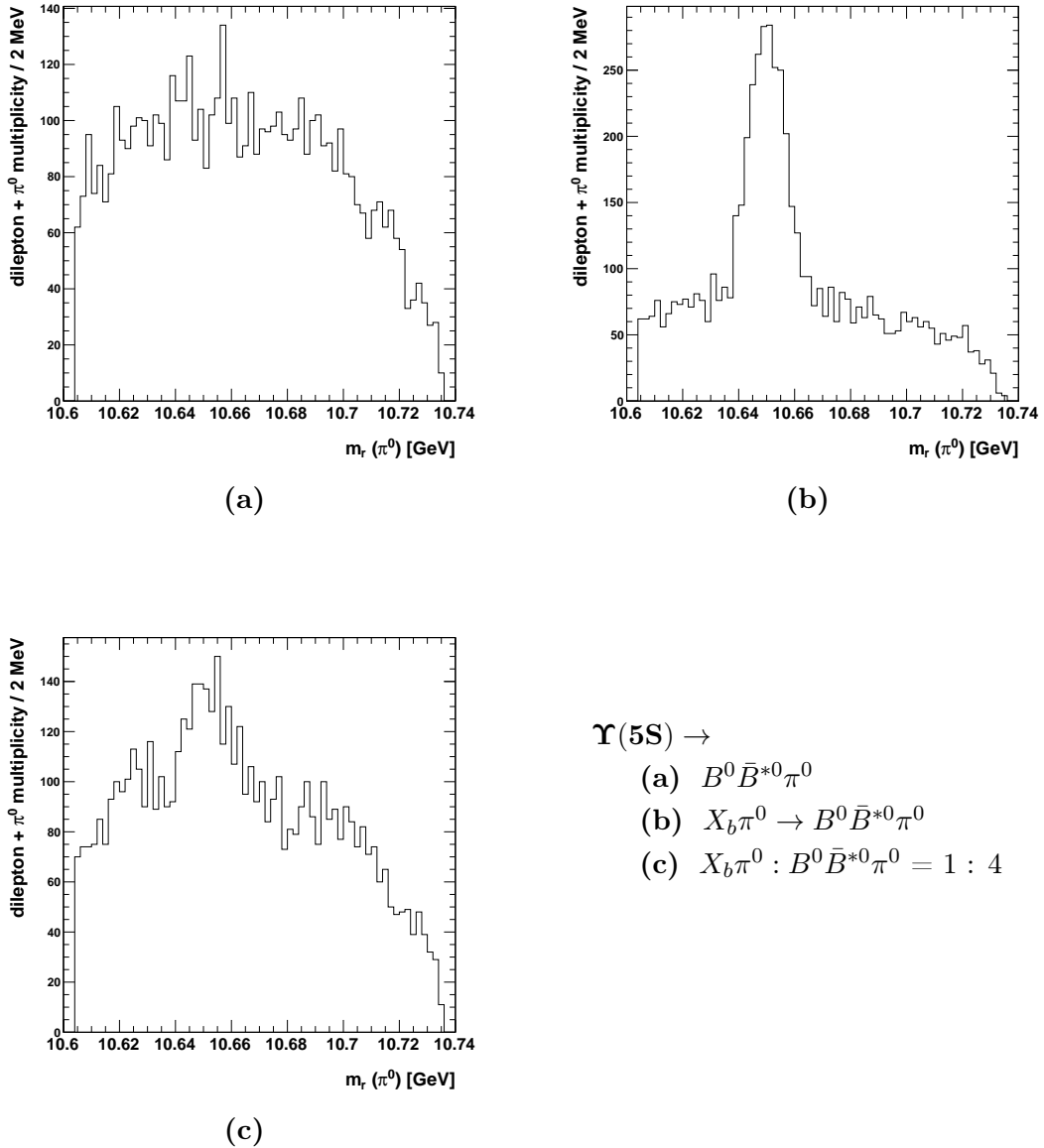


Figure 3.24.: Plot (a) shows a simulation of the π^0 recoilmass distribution if there are no undiscovered states ($\Upsilon(5S) \rightarrow B^0 \bar{B}^{*0} \pi^0$). If there was a new state with mass 10.65 GeV which decays into B mesons recoiling against the π^0 , the π^0 recoilmass distribution would look like plot (b), channel $\Upsilon(5S) \rightarrow X_b \pi^0 \rightarrow B^0 \bar{B}^{*0} \pi^0$. (c) shows the distribution of the π^0 recoilmass, if the branching fraction ($\Upsilon(5S) \rightarrow X_b \pi^0$)/($\Upsilon(5S) \rightarrow B^0 \bar{B}^{*0} \pi^0$) would be 1 : 4. Even in such a dirty environment an enhancement of the count rate at the X_b mass (10.65 GeV) can be seen.

The resolution of the recoilmass is limited by the resolution of the π^0 energy, which is again determined by the photon energy resolution of the electromagnetic calorimeter,

see Eq. (2.4.2). Since a π^0 has two daughter photons, the energy resolution of the π^0 reads

$$\begin{aligned}\Delta E(\pi^0) &= \sqrt{\Delta E(\gamma_1)^2 + \Delta E(\gamma_2)^2} \\ &= \sqrt{\left(0.013 \cdot \sqrt{E(\gamma_1)[GeV]}\right)^2 + \left(0.013 \cdot \sqrt{E(\gamma_2)[GeV]}\right)^2} .\end{aligned}\quad (3.3.5)$$

Fig. 3.25 shows the two-dimensional correlation between $E(\pi^0)$ and $\Delta E(\pi^0)$.

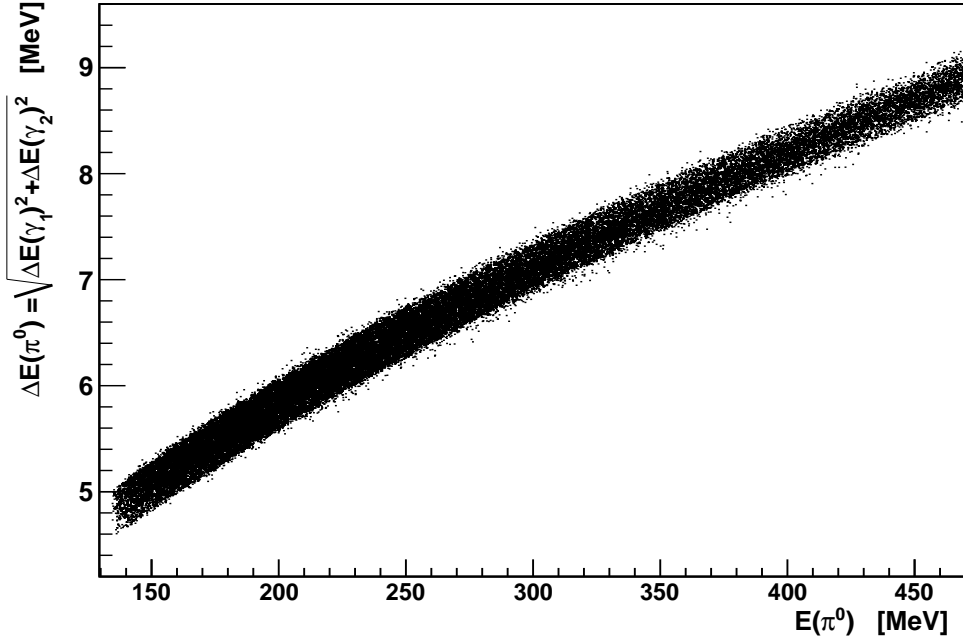
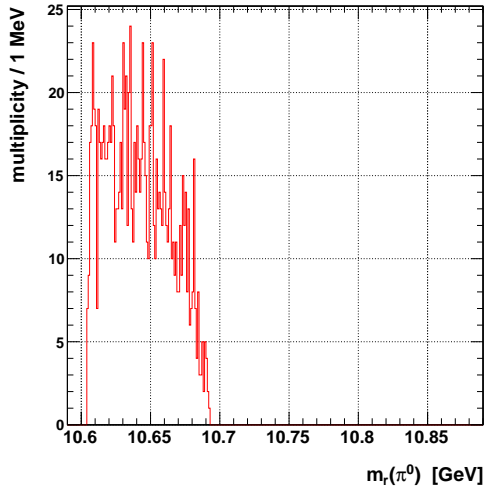


Figure 3.25.: Correlation between $E(\pi^0)$ and $\Delta E(\pi^0)$.

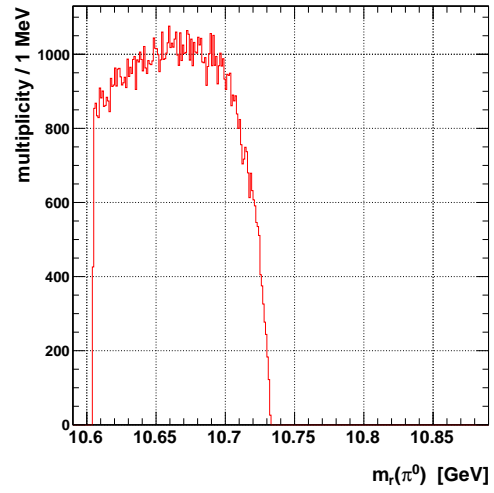
For the purpose of getting significant results the bin resolution has to be adjusted to the resolution of the π^0 recoil mass somehow. In order to avoid signal artifacts the bin resolution has to be finer-grained than the actual detector resolution for π^0 detection. A resolution of 1 MeV per bin is used for that purpose, which is approximately five times more accurate than the smallest value of $\Delta E(\pi^0)$, which is ≈ 5 MeV (see Fig. 3.25). If there was a new state with a sufficient production cross section and a significant branching fraction into $B^{(*)}\bar{B}^{(*)}$ it should be seen in all data points above the production threshold.

Figures 3.26 and 3.27 show the π^0 recoil mass distributions for scan points with different \sqrt{s} . As one can see there are no structures with statistical significance. Neglecting statistical fluctuations, all recoil mass distributions look relatively flat. The edges are explained by the π^0 momentum constraints and the limitation of the phase

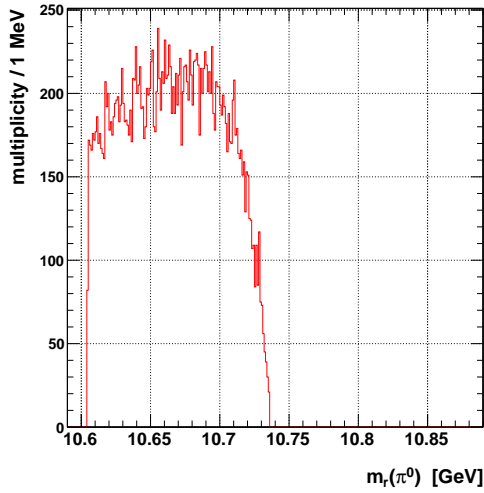
space of each scan point. The broadening of the distributions with \sqrt{s} is also explained by the π^0 momentum constraints which get looser with rising \sqrt{s} .



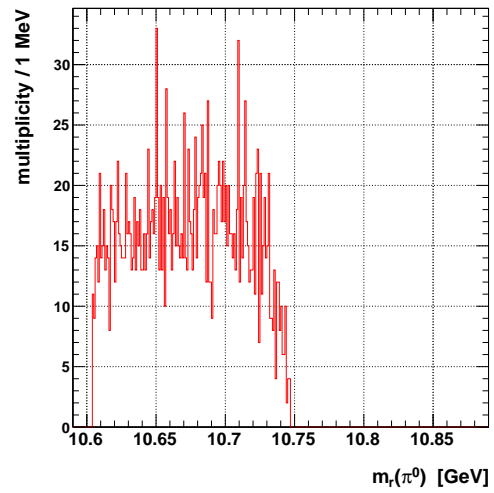
$$\sqrt{s} = 10.8275 \text{ GeV}$$



$$\sqrt{s} = 10.8675 \text{ GeV}$$



$$\sqrt{s} = 10.871 \text{ GeV}$$



$$\sqrt{s} = 10.8825 \text{ GeV}$$

Figure 3.26.: π^0 recoilmass distributions for the energy values $\sqrt{s} = 10.8275, 10.8675, 10.871$ and 10.8825 GeV

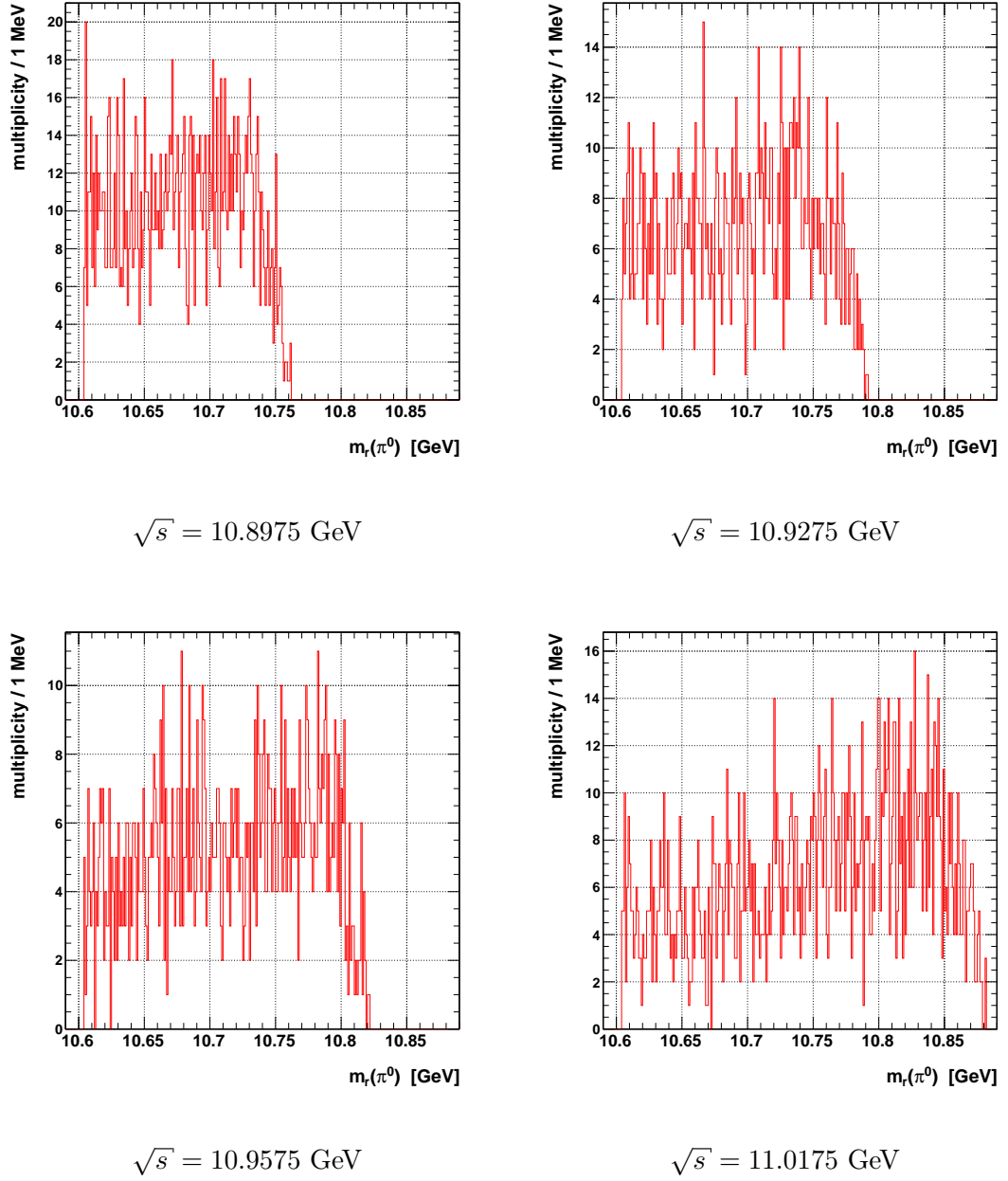


Figure 3.27.: π^0 recoilmass distributions for the energy values $\sqrt{s} = 10.8975$, 10.9275 , 10.9575 and 11.0175 GeV

Fig. 3.28 shows the luminosity weighted sum of all recoilmass distributions from Fig. 3.26 and Fig. 3.27, no evidence for new states decaying into $B^{(*)}\bar{B}^{(*)}$ can be found. This plot contains an additional systematical error, since the constraints for the π^0 momenta are changing with each scan point and therefore each scan point contains different contributions from non primary pions.

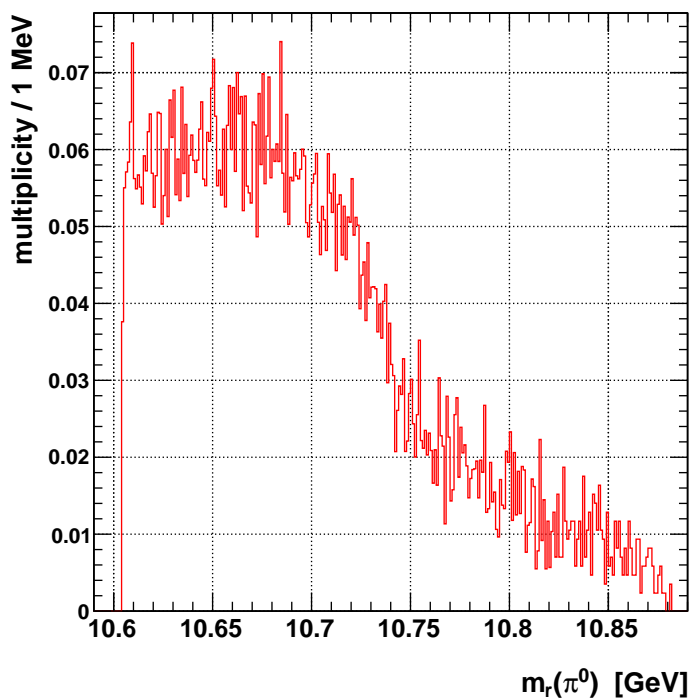


Figure 3.28.: Sum of all luminosity weighted π^0 recoil mass distributions from Fig. 3.26 and Fig. 3.27

In order to get an estimate for the upper limit of the branching fraction $e^+e^- \rightarrow X_b + \pi^0$, the small enhancement around $\sqrt{s} = 10.69$ GeV in the $\int \mathcal{L} dt = 98.087 \text{ fb}^{-1}$ $\Upsilon(5S)$ data sample ($\sqrt{s} = 10.8675$ GeV) in Fig. 3.26 was interpreted as a Gaussian signal $A \cdot \exp\left[-\frac{(x-\mu)^2}{2\Gamma^2}\right]$ with the fixed values $\mu = 10.69$ GeV (mean) and $\Gamma = 0.006$ GeV being the width of the gaussian curve, which corresponds to the average detector resolution for neutral pions. Fitting a background distribution is nontrivial, since it's choice is ambiguous and has an impact on the signal yield. To minimize the number of parameters a second order polynomial $f(x) = p_0 + p_1 \cdot x + p_2 \cdot x^2$ was used to fit the background distribution. The fit region was limited to the interval $[10.61; 10.71]$ to neglect the precipitous edges at ≈ 10.6 GeV and ≈ 10.71 GeV coming from π^0 momentum constraints and phase space limitations.

In order to obtain the signal yield that gives us 90% C.L., the amplitude of the Gaussian was forced to increase in such a way that the χ^2 of the fit will increase by 1.64 units. This procedure was also used in [43] to determine an upper limit for $\Omega^- \rightarrow \Xi^- \gamma$ radiative decays. The fit results were stable and insensitive to start vector variations, the results of the fit and of the upper limit calculations can be seen in Tab. 3.7 and Fig. 3.29.

parameter	signal + background fit result	upper limit results
A	33.839	46.195
μ	10.69 GeV (fixed)	10.69 GeV (fixed)
Γ	0.006 GeV (fixed)	0.006 GeV (fixed)
p_0	$-7.09272 \cdot 10^6$	$-7.09272 \cdot 10^6$ (fixed)
p_1	$1.33080 \cdot 10^6$	$1.33080 \cdot 10^6$ (fixed)
p_2	$-6.24153 \cdot 10^4$	$-6.24153 \cdot 10^4$ (fixed)
χ^2	106.299	107.939

Table 3.7.: Fit results for the π^0 recoilmass distribution from the large $\Upsilon(5S)$ data sample. The right column represents the parameter values for the upper limit at 90% confidence level.

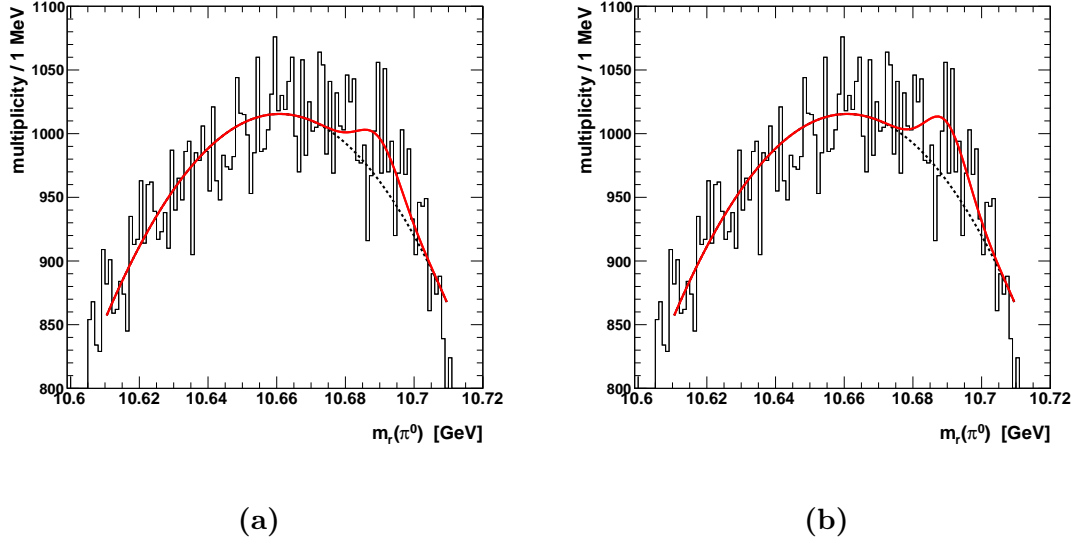


Figure 3.29.: Plot (a) shows the fit of the gaussian signal plus the second order polynomial background distribution. Actually there is a nonzero signal yield, but it is not convincing and also depending on the choice of the background function. Plot (b) shows the fitted curve of the upper limit calculations. The complete fit functions are drawn in red, the black dashed lines represent the background distributions.

More than 99.95% of the signal yield lies inside the interval $[10.67; 10.71]$. Hence the signal and background yield is calculated in that region only. The fit function can be used to calculate the integrated signal yield I_s , the integrals were numerically

calculated by Mathematica:

$$\begin{aligned} I_s &= \int_{10.67}^{10.71} \text{upper limit signal} + \text{background} - \int_{10.67}^{10.71} \text{background} \\ &= 38.1016 - 37.4074 = 0.6942 \quad . \end{aligned}$$

This is **not** the yield one can use for calculating the upper limit, since the values of the integrals depend on the bin resolution. The total number of counts in the region $[10.67; 10.71]$ equals 38825. This number will not vary with the bin resolution, therefore the integral for the signal+background yield corresponds to 38825 counts. The relations between the signal and the background integrated yield can be transformed into a true signal count rate by applying these relations to the total number of counts, which is 38825. These calculations lead to upper limit count rates of

$$\begin{aligned} \text{signal: } 707.38 \text{ counts} &:= N \quad \text{and} \\ \text{background: } 38117.62 \text{ counts} &:= N_b \quad . \end{aligned}$$

An upper limit for the branching fraction $\mathcal{B}(\Upsilon(5S) \rightarrow X_b \pi^0 (\gamma) \rightarrow B^{(*)0} \bar{B}^{(*)0} \pi^0 (\gamma)) =: \mathcal{B}_1$ can then be calculated by

$$\mathcal{B}_1 \leq \frac{N}{\int \mathcal{L} dt \cdot \sigma(e^+e^- \rightarrow \Upsilon(5S)) \cdot \mathcal{B}(\Upsilon(5S) \rightarrow B^{(*)0} \bar{B}^{(*)0} X) \cdot \left(\mathcal{B}(B^0 \rightarrow l^+ \nu_l X)\right)^2 \cdot \varepsilon_1 \cdot \varepsilon_2} \quad (3.3.6)$$

with

$$\begin{aligned} \int \mathcal{L} dt &= 98.087 \text{ fb}^{-1} = 9.8087 \cdot 10^7 \text{ nb}^{-1} \\ \sigma(e^+e^- \rightarrow \Upsilon(5S)) &= 0.3 \text{ nb} \quad [44] \\ \mathcal{B}(\Upsilon(5S) \rightarrow B^{(*)0} \bar{B}^{(*)0} X) &= 59\% \quad [15] \\ \mathcal{B}(B^0 \rightarrow l^+ \nu_l X) &= 10.33\% \quad [15] \end{aligned}$$

and $\varepsilon_1 = \varepsilon(B^0 \bar{B}^0 \pi^0) \approx 0.28$ (see Tab. A.1) being the lower limit for the reconstruction efficiency regarding dilepton momentum cuts, particle identification efficiency and detector acceptance and $\varepsilon_2 = \varepsilon(\pi^0) \approx 0.27$ being the π^0 detection efficiency, which comes from MC data (13837 of 50000 neutral pions were accepted after the cuts). Inserting these values into Eq. (3.3.6) yields

$$\mathcal{B}_1 \leq \frac{707.38}{9.8087 \cdot 10^7 \text{ nb}^{-1} \cdot 0.3 \text{ nb} \cdot 0.59 \cdot 0.1033^2 \cdot 0.28 \cdot 0.27} \approx 0.0505 = 5.05 \%$$

for the upper limit for the branching fraction \mathcal{B}_1 at 90% confidence level.

To account for the systematic error due to the choice of the background function, the described procedure was also accomplished using a fourth order and sixth order polynomial for the background. This causes modifications in the signal and background

yield and therefore changes the total number of “signal” events. The fit results (see Tab. C.1) were transformed into a true signal rate, both yields were averaged and inserted into Eq. (3.3.6), the deviation from 5.05% is the systematic error of the fit procedure. The final value of the upper limit including the systematic error of the fit procedure resulted in $\mathcal{B}_1 \leq 5.05 \pm 0.14$ % at 90% confidence level.

3.4. $B^{(*)}\bar{B}^{(*)}\pi^+\pi^-$ events

An extensive analysis of $B^*\bar{B}^{(*)}\pi^+\pi^-$ events is not possible in this energy region, since the production threshold does not open before $\sqrt{s} = m(B\bar{B}\pi^+\pi^-) = 10.837$ GeV. To calculate constraints for the $\pi^+\pi^-$ pair one has to use three-body kinematics. In three-body decays the decay products can carry any energy value below the upper limit which is set by the available phase space. The $\pi^+\pi^-$ carry their maximum energy, if all the kinematic energy $E_{\text{kin}} = \sqrt{s} - m(B\bar{B}^*\pi^+\pi^-)$ is shared by the pions and the bound $B\bar{B}^*$ pair is created at rest. Since positive pions have the same mass as negative pions they both carry half of the available kinetic energy. Tab. 3.8 shows the upper limits of the $\pi^+\pi^-$ energies in the CM frame.

\sqrt{s} [GeV]	$E_{\text{kin}}^{\pi^+\pi^-} = \sqrt{s} - m(B\bar{B}^*\pi^+\pi^-)$ [GeV]	$E(\pi^+\pi^-)$ [GeV]
< 10.883	–	–
10.8895	0.00636	0.2855
10.8975	0.00718	0.2935
10.9275	0.02218	0.3235
10.9575	0.03718	0.3535
10.9875	0.05218	0.3825
11.0175	0.06718	0.4135

Table 3.8.: Upper limits on the energy of the $\pi^+\pi^-$ pair created in $B\bar{B}^*\pi^+\pi^-$ events.

As one can see the overall maximum energy of one pion is 0.4135 GeV/2 = 0.20675 GeV. A pion with $p_z = 0$ has the maximum transverse momentum $|\vec{p}_T| = \sqrt{p_x^2 + p_y^2} = |\vec{p}|$. Knowing that charged particles have a bending inside the magnetic field of the detector ($B = 1.5$ T) due to the Lorentz force, one can calculate the maximum radius of such a π^\pm track with $p_z = 0$:

$$\begin{aligned}
 \text{centripetal force} &= \text{Lorentz force} \\
 \frac{2 \cdot E_{\text{kin}}}{r} &= q v B \\
 \frac{2 \cdot (E - m)}{r} &= \frac{q p c B}{E} \\
 \Rightarrow r &= \frac{2 \cdot (E - m) \cdot E}{q p c B} \approx 0.405 \text{ m} \quad , \quad (3.4.1)
 \end{aligned}$$

with p being the pion momentum $p = \sqrt{E^2 - m^2}$, q being the charge ($= 1e$) and c being the velocity of light. Although this is the maximum radius in the CM frame, this is also the maximum radius in the LAB frame, since a Lorentz boost in the z -direction has no impact on transversal momentum components which are perpendicular to that direction. Such a maximum energy pion with a track radius of approximately 40 cm curls up inside the inner part of the drift chamber and is only measured by the silicon vertex detector and the inner part of the drift chamber, therefore particle identification and the measurement of particle properties cannot be done accurately. Fig 3.30 shows the very few signal counts for such events, confirming that an extensive analysis is not possible in this energy region.

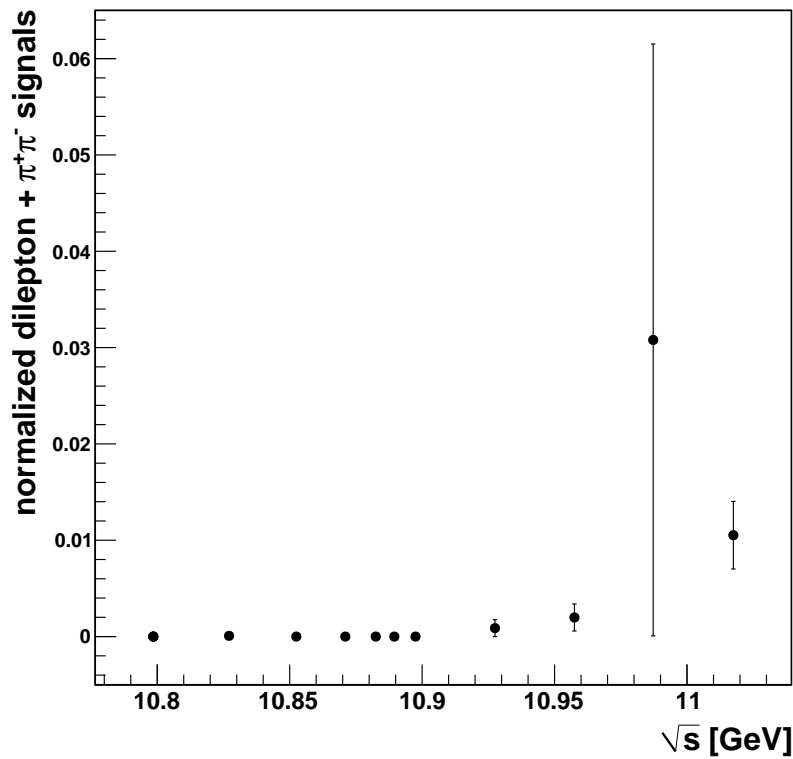


Figure 3.30.: Normalized dilepton + $\pi^+\pi^-$ counts in dependence of \sqrt{s} . As the available phase space is increasing with \sqrt{s} , the probability that low energy pion pairs are measured accurately enough is increasing.

Summary and Conclusion

And it shall be, when thou hast made an end of reading this book, that thou shalt bind a stone to it, and cast it into the midst of Euphrates.

Jeremiah 51, 63

This work dealt with the search for new bottomonium(-like) states in the $e^+e^- \rightarrow B^{(*)}\bar{B}^{(*)}(\pi)(\pi)$ channel in order to find a bottom counter part of the $X(3872)$. Energy scan data between $\Upsilon(4S)$ and $\Upsilon(6S)$ collected at the BELLE experiment was used for the analysis. To account for the relatively small integrated luminosities in the energy scan, a highly inclusive dilepton approach was chosen to tag B mesons. The dilepton was required to consist of the two leptons with the highest energy in this event and was additionally cleaned up by momentum cuts to reduce background contributions. The observation of B oscillation in $\Upsilon(4S)$ decays proved the efficiency of the B meson tagging using dileptons. In order to compare the results of the energy scan points, the obtained values were normalized to the integrated luminosity of the data point. An investigation of the normalized dilepton signal yield in dependence of \sqrt{s} was used to fit the lineshape of the $\Upsilon(5S)$, with $\phi_{\Upsilon 5S} = -1.512 \pm 0.066$, $\mu_{\Upsilon 5S} = 10.838 \pm 0.067$ GeV and $\Gamma_{\Upsilon 5S} = 0.106 \pm 0.0087$ GeV being the results of the fit, which differ from the recent BaBar results. The fit also revealed evidence for B meson production in $\Upsilon(6S)$ decays.

An additional neutral pion together with the B mesons tagged by the dilepton signal was required to investigate states with quantum numbers $J^{PC} = 1^{+\pm}$ in e^+e^- annihilation, the limited phase space was used to set limits on the π^0 momentum. The signal yield in dependence of \sqrt{s} showed the domination of $B^{*0}\bar{B}^{*0}\pi^0$ and $B_s^*\bar{B}_s^*\pi^0$ production, which is confirmed by several BELLE studies. The π^0 recoil mass method was used to find and to weigh new $1^{+\pm}$ states, but no significant signal could be seen in the recoil mass distributions of the different energy data points, showing that either

there are no new $J^{PC} = 1^{+\pm}$ states which decay into $B\bar{B}$ or the branching fractions are too small to see a primary π^0 signal in this large π^0 background environment. An upper limit on $\mathcal{B}(\Upsilon(5S) \rightarrow X_b \pi^0 (\gamma))$ could be determined to 5.05 ± 0.14 % at 90% confidence level.

An analysis in the $B\bar{B}\pi^+\pi^-$ channel turned out to be not accomplishable due to the very limited phase space, leading to a pion track upcurling in the magnetic field of the detector and therefore leading to an improper particle identification and unaccurate measurements of the particle's properties.

If such an energy scan could be accomplished with much larger statistics one could use a more promising and complex semi-exclusive recoilmass method to search for $J^{PC} = 1^{+\pm}$ states: One B meson is exclusively reconstructed. The recoilmass of this B meson is then required to allow another B meson plus an additional π^0 . The π^0 could then not only be chosen by momentum constraints but also by constraints on the recoilmass of the system of the exclusively reconstructed B meson and the π^0 . One could also reduce the π^0 background by rejecting all low energy pions which can be combined in a way to form other mesons (K^{*0} , ρ , D , ...). Such an analysis would lead to much cleaner results than the results presented in this thesis, but due to the small branching fractions of exclusively reconstructable B meson decay channels ($\sim 10^{-4}$) such an approach is not possible for energy scans with as small statistics as it is in the energy scan used for this analysis.

The question about the undiscovered bottomonium states is still open. Can we expect any surprises in the bottom region like those found in the charm region with the discoveries of $X(3872)$ and $X(4260)$ at the B factories? Will the high luminosity super B factory BELLE II discover such new states? What is the inner structure of the $X(3872)$? Do theoretically predicted exotic particles like hybrids, tetraquarks, molecules or glueballs exist? Of what kind is physics beyond the Standard Model? Only patient research in this field can shed light on the issue. However, as it turned out many times, a lot of answers lead to even more questions. Will there be a point where we finally understand all structures of the universe or is this the attempt to drink up the sea? Whatever the answer will be, I personally think that it will be fascinating and worth the research efforts and, most of all, it will magnify the glory of the one, who "was, is and is to come" (Revelation 4,8).

Deutsche Zusammenfassung

Da es viele theoretisch vorhergesagte, aber bisher experimentell nicht nachgewiesene Bottomonium Zustände gibt, beschäftigt diese Arbeit sich mit der Suche nach neuen Bottomonium(-artigen) Zuständen in e^+e^- Reaktionen mit Endzustand $B^{(*)}\bar{B}^{(*)}(\pi)(\pi)$. Schwere Quarkonia, also Mesonen, die aus einem c oder b Quark und ihrem entsprechenden Antiquark bestehen, lassen sich theoretisch mithilfe von Potentialmodellen beschreiben. Hervorzuheben ist an dieser Stelle das sog. Cornell-Potential, welches aus einem perturbativen $1/r$ Anteil und einem phänomenologischen, in r linearen Anteil aufgebaut ist. Aufgrund der schweren Quarkmassen von c und b Quark ($m_c \approx 1.27$ GeV und $m_b \approx 4.20$ GeV [15]) liefert bereits die nichtrelativistische Schrödingergleichung unter Einsetzen des Cornell-Potentials akzeptable Resultate bei der Vorhersage von $c\bar{c}$ und $b\bar{b}$ Massenspektren.

Die Datengrundlage der Analyse bildet ein Energiescan zwischen der $\Upsilon(4S)$ und der $\Upsilon(6S)$ Resonanz, welcher am BELLE Experiment in Japan durchgeführt wurde. Um den relativ geringen integrierten Luminositäten des Energiescans Rechnung zu tragen, wurde ein inklusiver Dileptonenansatz gewählt um B -Mesonen Zerfälle zu taggen. Außerdem wurden Impulscuts und ein J/ψ Veto verwendet um den Signaluntergrund zu minimieren. Über das Vorzeichen des gemessenen Leptons kann auf die Ladung des schwach zerfallenen bottom Quarks geschlossen werden. Die Beobachtung von B Oszillationen in $\Upsilon(4S)$ Zerfällen durch Analyse der Dileptonenvorzeichen bestätigt die Effizienz der Dileptonenauswahlkriterien. Um die Daten des Energiescans miteinander vergleichen zu können, wurde die Anzahl der Signale auf die integrierte Luminosität des Scanpunktes normiert. Eine Darstellung der Dileptonensignalrate in Abhängigkeit von \sqrt{s} zeigt die Beiträge von $\Upsilon(4S)$, $\Upsilon(5S)$ und $\Upsilon(6S)$ Zerfällen. Um diese Abhängigkeit im Detail zu verstehen, wurden drei Breit-Wigner Funktionen für die drei Resonanzen an die Datenpunkte gefittet. Die Kurvenparameter der $\Upsilon(4S)$ Resonanz wurden [15] entnommen, die der $\Upsilon(6S)$ Resonanz wurden an neue BaBar Messungen [38] angepasst, da die Anzahl der Datenpunkte für diese beiden Zustände nicht ausreicht um deren Kurvenparameter zu bestimmen. Der Fit für die $\Upsilon(5S)$ Resonanz

erbrachte folgende Kurvenparameter: $\phi_{\Upsilon_{5S}} = -1.512 \pm 0.066$, $\mu_{\Upsilon_{5S}} = 10.838 \pm 0.067$ GeV und $\Gamma_{\Upsilon_{5S}} = 0.106 \pm 0.0087$ GeV. Diese Ergebnisse unterscheiden sich von kürzlich veröffentlichten BaBar Resultaten. Aus dem Fit ergeben sich erste Hinweise auf B Mesonen Produktion in $\Upsilon(6S)$ Zerfällen.

Um nach Zuständen mit den Quantenzahlen $J^{PC} = 1^{+\pm}$ suchen zu können, wurde ein zusätzliches π^0 in die Analyse einbezogen. Da eine prinzipielle Unterscheidung zwischen $B\bar{B}$ und $B\bar{B}\pi^0$ Ereignissen nicht möglich ist, wurden Bedingungen für den Impuls des Pions aus dem vorhandenen Phasenraum berechnet. Dennoch ist die π^0 Untergrundrate relativ hoch, da sekundäre, niederenergetische Pionen aus Mesonenzerfällen nicht von den primären Pionen aus dem direkten $\Upsilon(5S) \rightarrow X_B\pi^0(\gamma)$ Zerfall unterschieden werden können. Die Signalrate, wo sowohl zwei B Mesonen als auch ein π^0 mit erlaubtem Impuls gefunden wurde, wurde gegen \sqrt{s} aufgetragen. An diese Darstellung ließen sich zwei Exponentialkurven für die Beiträge von $B^{*0}\bar{B}^{*0}\pi^0$ und von $B_s^{*0}\bar{B}_s^{*0}\pi^0$ anpassen, was jüngste Ergebnisse von BELLE bestätigt, die ebenfalls eine Dominanz von $B^{*0}\bar{B}^{*0}\pi^0$ und $B_s^{*0}\bar{B}_s^{*0}\pi^0$ Produktion in $\Upsilon(5S)$ Zerfällen feststellen konnten.

Um mit einer derart inklusiven Analyse die Masse eines möglichen X_b Zustandes bestimmen zu können, wurde die Methode der Rückstossmasse verwendet. Dabei wurde die Rückstossmasse der Pionen bei Ereignissen mit zwei durch Leptonen getaggte B Mesonen analysiert. Diese Analyse brachte jedoch keine Hinweise auf bisher ungedeckte Zustände mit Quantenzahlen $J^{PC} = 1^{+\pm}$. Eine obere Grenze für das $\Upsilon(5S)$ Verzweungsverhältnis nach $X_b\pi^0(\gamma)$ konnte zu 5.05 ± 0.14 % im 90% Konfidenzintervall bestimmt werden.

Die Analyse von $B^{(*)0}\bar{B}^{(*)0}\pi^+\pi^-$ Endzuständen brachte keine neuen Erkenntnisse, da der Phasenraum für die Pionen derart beschränkt ist, dass diese durch das Magnetfeld schon im inneren Teil des Detektors aufcurlen und deshalb nicht präzise gemessen werden können. Die erhaltene Signalrate ließ keine weiteren Analysen dieser Ereignisse zu.

Appendix



Monte Carlo Data

A.1. Efficiencies of the Momentum Cuts

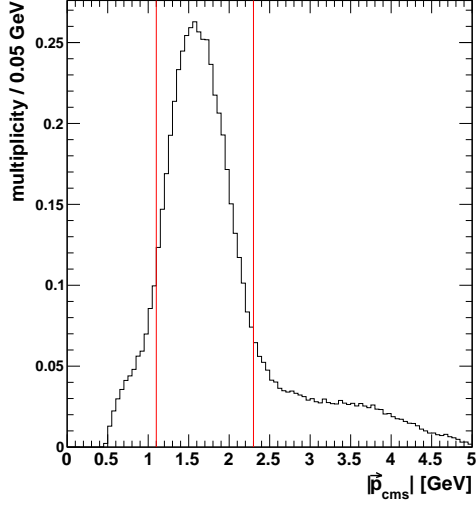
decay channel $\Upsilon(5S) \rightarrow$	efficiency of $ \vec{p}_{\text{cms}} $ cuts [%]	efficiency normalized to $B^0\bar{B}^0$
$B^0\bar{B}^0$	25.925	1
$B^0\bar{B}^{*0}$	26.4525	1.020
$B^{*0}\bar{B}^{*0}$	26.73	1.031
$B_s^0\bar{B}_s^0$	26.56	1.024
$B_s^0\bar{B}_s^{*0}$	27.7675	1.071
$B_s^{*0}\bar{B}_s^{*0}$	28.5825	1.103
$B^0\bar{B}^0\pi^0$	28.3675	1.094
$B^0\bar{B}^{*0}\pi^0$	28.89	1.114
$B^{*0}\bar{B}^{*0}\pi^0$	29.2175	1.127
$B_s^0\bar{B}_s^0\pi^0$	29.02	1.119
$B^0\bar{B}^0\pi^+\pi^-$	29.8	1.149

Table A.1.: Monte Carlo efficiencies of the lepton momentum cuts from semileptonic B^0 (B_s^0) decays in dependence of different $\Upsilon(5S)$ decay channels. A significant efficiency dependence on the $\Upsilon(5S)$ decay channel cannot be seen. BELLE detector acceptance and particle identification efficiency is included.

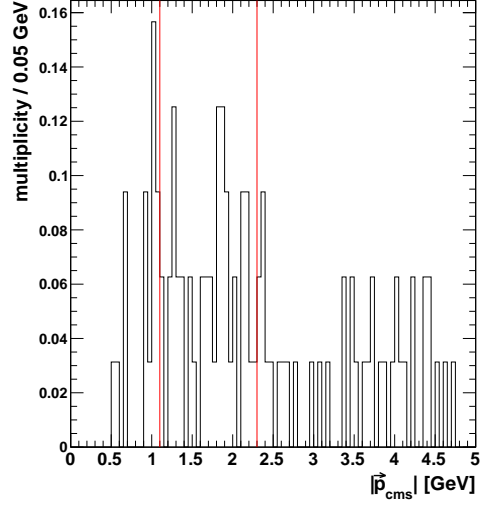
A.2. J/ψ lepton momenta

As mentioned in section 3.2.2, the J/ψ leptons lie directly in the allowed momentum range for the leptons from B decays, therefore an adjustment of the momentum cuts to account for rising \sqrt{s} could be done by an investigation of the \sqrt{s} dependence of the lepton momenta from J/ψ decays. Figures A.1, A.2 and A.3 show the results of

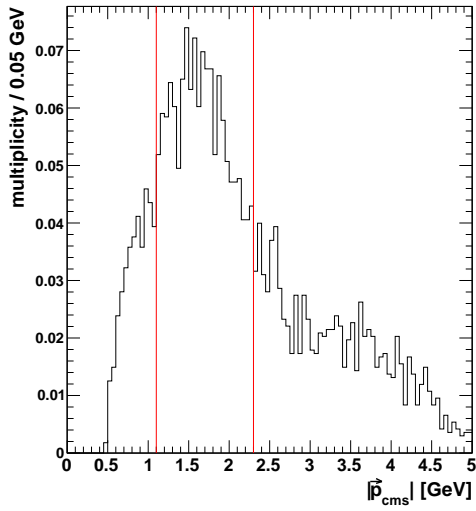
this investigation and show no evidence for a change of the lepton momenta.



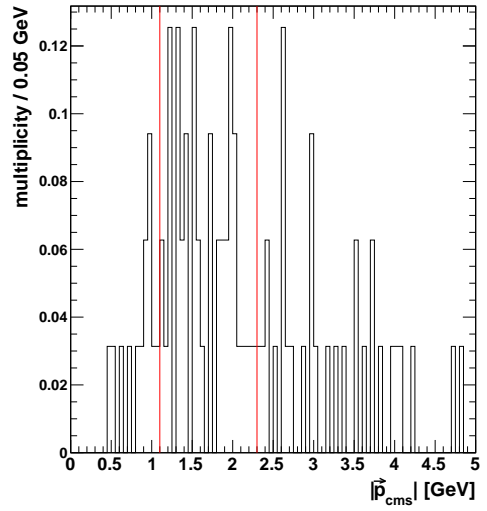
$\Upsilon(4S)$ ($\sqrt{s} = 10.5779$ GeV)



$\sqrt{s} = 10.7985$ GeV

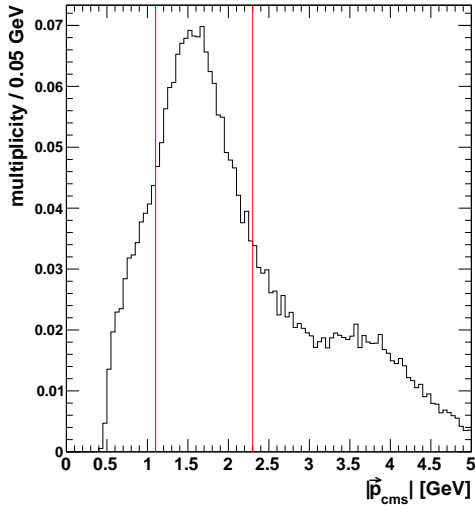


$\sqrt{s} = 10.8275$ GeV

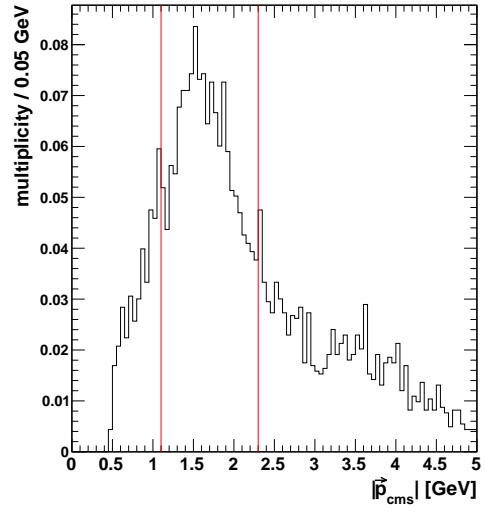


$\sqrt{s} = 10.8525$ GeV

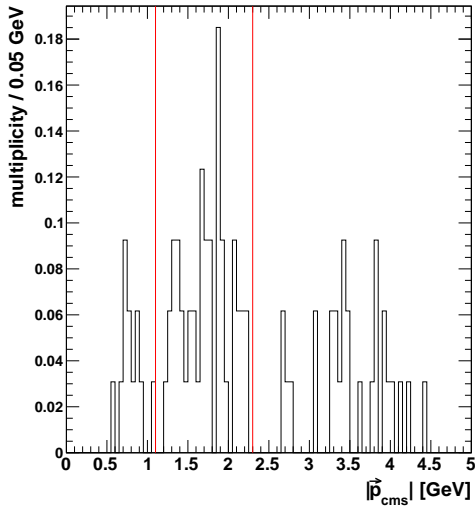
Figure A.1.: Lepton momenta from J/ψ decays in dependence of \sqrt{s} , $\sqrt{s} = 10.5779$ GeV to $\sqrt{s} = 10.8525$ GeV



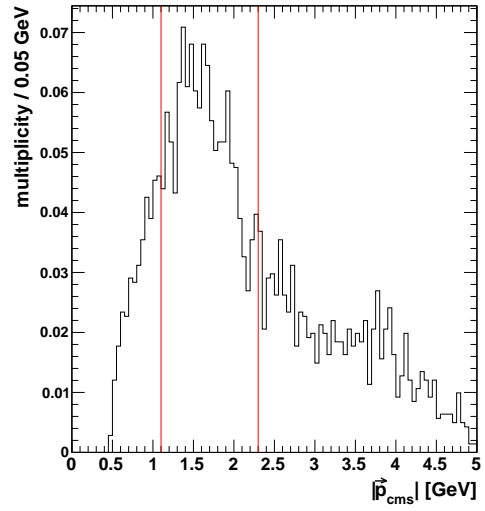
$\Upsilon(5S)$ ($\sqrt{s} = 10.871$ GeV)



$\sqrt{s} = 10.8825$ GeV

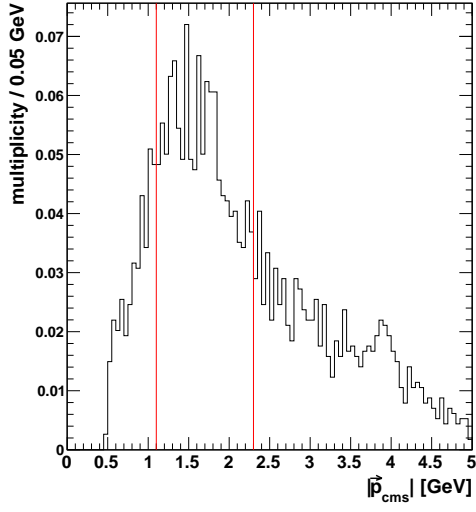


$\sqrt{s} = 10.8895$ GeV

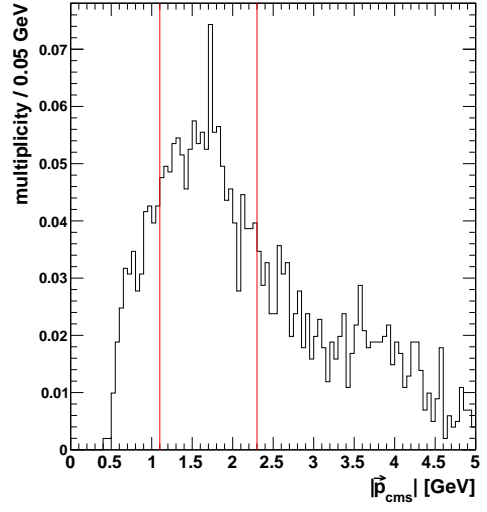


$\sqrt{s} = 10.8975$ GeV

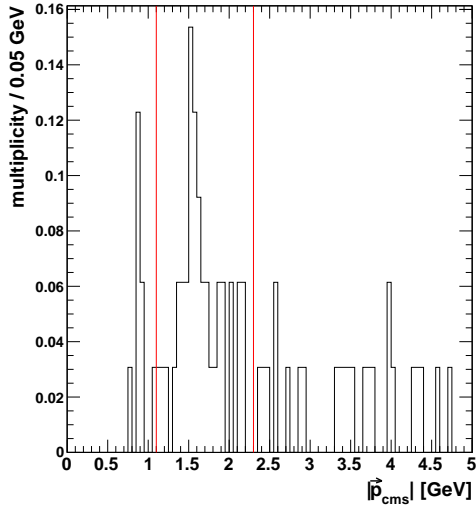
Figure A.2.: Lepton momenta from J/ψ decays in dependence of \sqrt{s} , $\sqrt{s} = 10.8525$ GeV to $\sqrt{s} = 10.8975$ GeV



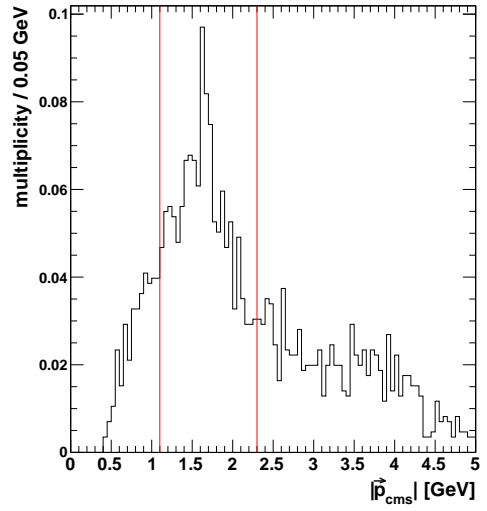
$$\sqrt{s} = 10.9275 \text{ GeV}$$



$$\sqrt{s} = 10.9575 \text{ GeV}$$



$$\sqrt{s} = 10.9875 \text{ GeV}$$



$$\sqrt{s} = 11.0175 \text{ GeV}$$

Figure A.3.: Lepton momenta from J/ψ decays in dependence of \sqrt{s} , $\sqrt{s} = 10.9275$ GeV to $\sqrt{s} = 11.0175$ GeV

A.3. Determination of the Correction Factors

As mentioned in chapter 3 the momentum cuts are not adjusted to account for rising $|\vec{p}_{\text{cms}}|$ of the leptons. A correction factor Ξ was introduced to correct this systematic error. A Monte Carlo simulation based on 40000 semileptonically decaying $B^0\bar{B}^0$ pairs at five energy values of the scan was analyzed, figures A.4 - A.8 show the outcoming spectra of the two leptons.

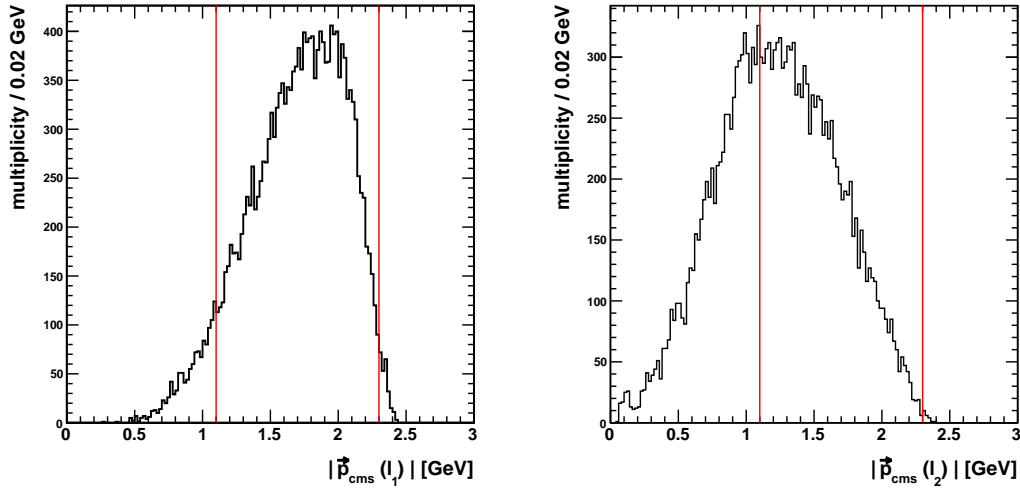


Figure A.4.: $|\vec{p}_{\text{cms}}|$ spectra of lepton l_1 (left) and lepton l_2 (right) from semileptonic $B^0\bar{B}^0$ decays at $\sqrt{s} = 10.5779$ GeV

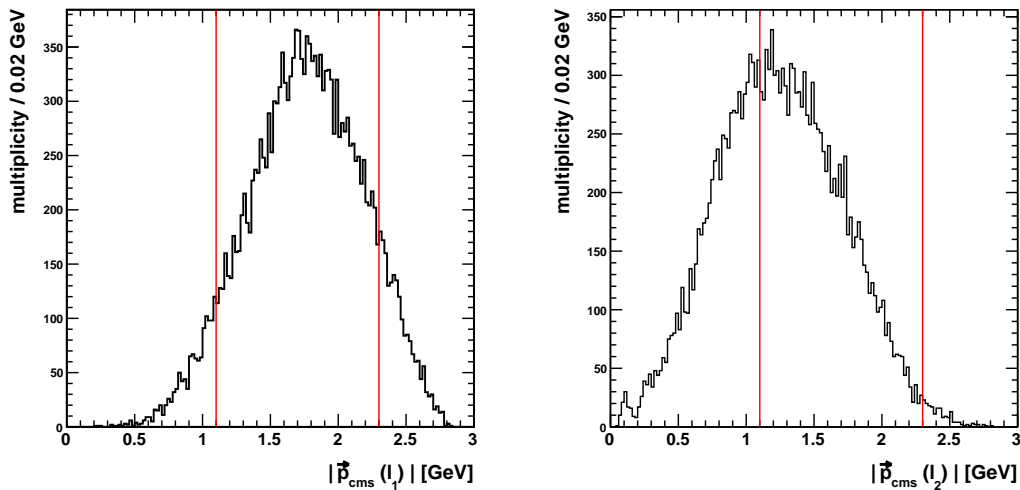


Figure A.5.: $|\vec{p}_{\text{cms}}|$ spectra of lepton l_1 (left) and lepton l_2 (right) from semileptonic $B^0\bar{B}^0$ decays at $\sqrt{s} = 10.7985$ GeV

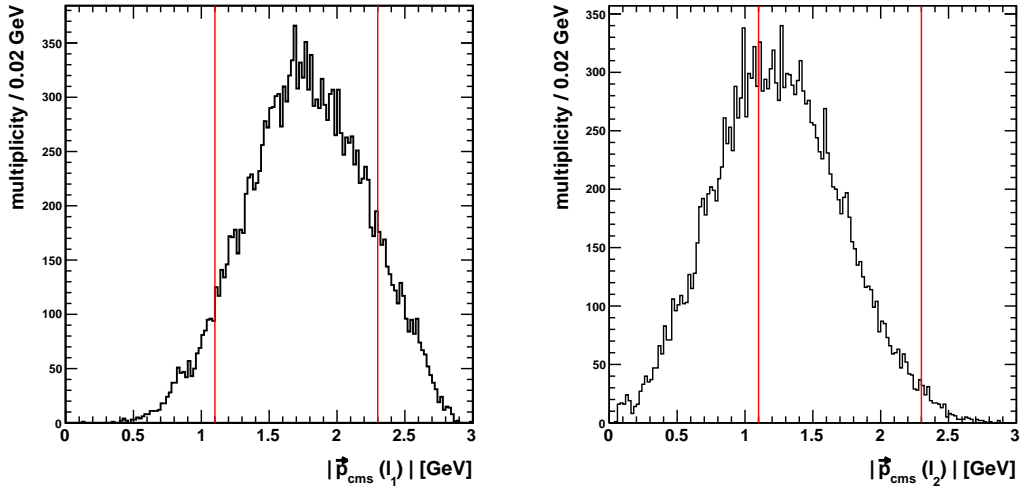


Figure A.6.: $|\vec{p}_{\text{cms}}|$ spectra of lepton l_1 (left) and lepton l_2 (right) from semileptonic $B^0\bar{B}^0$ decays at $\sqrt{s} = 10.871$ GeV

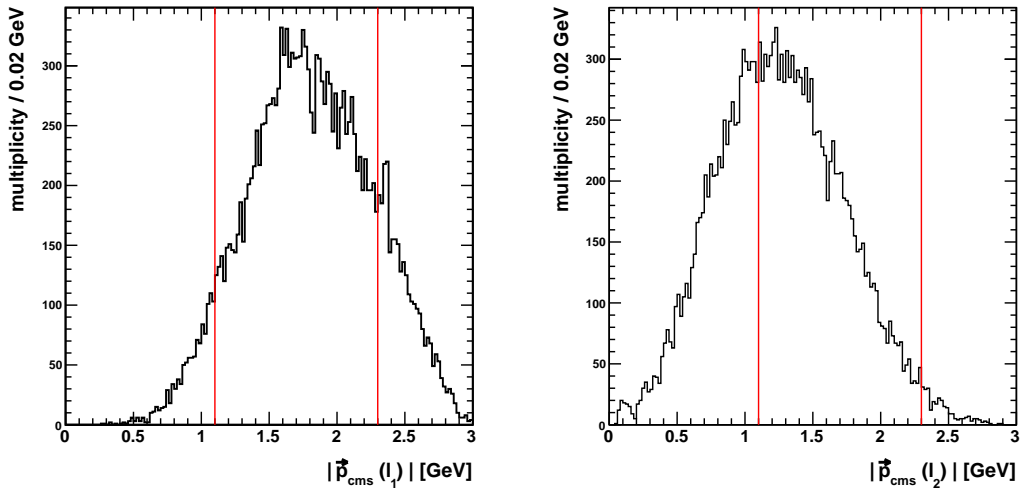


Figure A.7.: $|\vec{p}_{\text{cms}}|$ spectra of lepton l_1 (left) and lepton l_2 (right) from semileptonic $B^0\bar{B}^0$ decays at $\sqrt{s} = 10.9575$ GeV

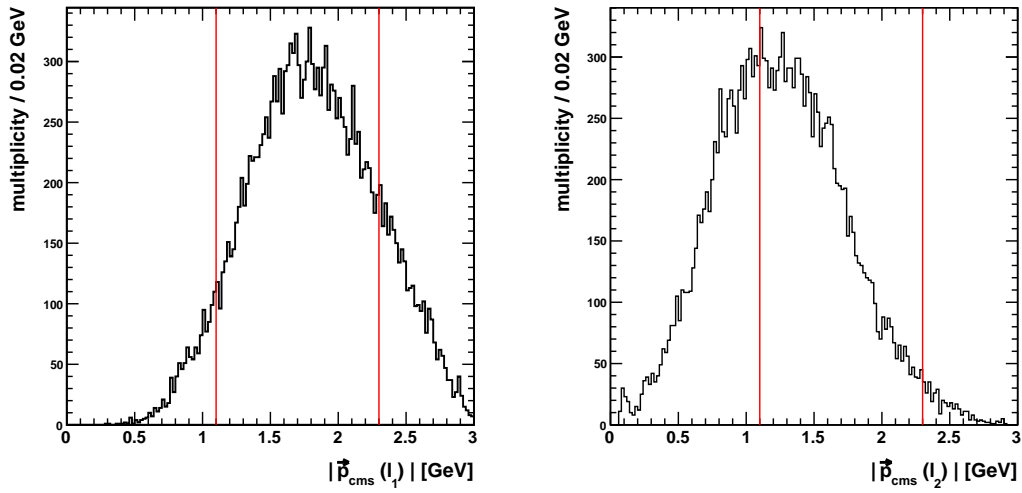


Figure A.8.: $|\vec{p}_{\text{cms}}|$ spectra of lepton l_1 (left) and lepton l_2 (right) from semileptonic $B^0\bar{B}^0$ decays at $\sqrt{s} = 11.0175$ GeV

\sqrt{s} [GeV]	dilepton signals without cut	dilepton signals after cuts
$\Upsilon(4S)(10.5779)$	18502	10727
10.7985	18745	9564
$\Upsilon(5S)(10.871)$	18549	9191
10.9575	18528	8799
$\Upsilon(6S)(11.0175)$	18636	8562

Table A.2.: Monte Carlo results based on 40000 simulated $B^0\bar{B}^0$ pairs, which decay semileptonically.

B

Energy Scan Datasets

energy [GeV]	exp.	runs	$\int \mathcal{L} dt$ [fb ⁻¹]		
$\Upsilon(1S)$ (9.4600)	65	1040-1102	2.360		
		1143-1232	3.351		
$\Upsilon(2S)$ (10.0218)	67	1016-1123	6.517		
$\Upsilon(3S)$ (10.3547)	49	1060-1185	1.813		
$\Upsilon(4S)$ (10.5779)	51	5-1267	22.153		
		10.7985	61	1314	0.03192
		10.8275	61	1270-1293	1.67651
		10.8525	61	1312	0.03188
$\Upsilon(5S)$ (10.871)	53	1-272	21.513		
		10.8825	61	1294-1310	1.83090
		10.8895	61	1311	0.03242
		10.8975	61	1210-1235	1.41047
		10.9275	61	1249-1269	1.13865
		10.9575	61	1239-1248	1.00918
		10.9875	61	1313	0.03255
		11.0175	61	1315-1339	0.85534
		$\Upsilon(5S)$ (10.8675)*	67	98 - 696	27.32
				69	12 - 819
892 - 1309	19.229				
71	27 - 221			8.111	
2001 - 2185	11.537				
		2194 - 2244	3.29		

Table B.1.: Data used for the analysis and the integrated luminosity for each data point

* **Note:** This data was used in the π^0 recoilmass analysis only in order to enhance the statistics.

C

Mathematics

C.1. Kinematics

Two body decays played an important role in the calculation of the constraints for the neutral pions, since three body decays allow to create one particle at rest whereas the other two particles behave as in a two body decay. The derivation of the used formulas is shown here.

Energy is conserved in all physics experiments. Starting from the relativistic expression for the energy $E = \sqrt{\vec{p}^2 + m^2}$, the energy balance for a two-body decay of a particle with mass M into two lighter particles with masses m_1 and m_2 in the M rest frame is given by

$$E_1 + E_2 = \sqrt{\vec{p}_1^2 + m_1^2} + \sqrt{\vec{p}_2^2 + m_2^2} = M \quad . \quad (\text{C.1.1})$$

Knowing that in the M rest frame the sum over the momenta \vec{p}_1 and \vec{p}_2 is equal zero, yields $|\vec{p}_1| = |\vec{p}_2| = p$. Expressing E_2 in terms of E_1 using the addition of 0 brings us to

$$E_1 + E_2 = E_1 + \sqrt{p^2 + m_1^2 - m_1^2 + m_2^2} = E_1 + \sqrt{E_1^2 - m_1^2 + m_2^2} = M \quad (\text{C.1.2})$$

and solving equation (C.1.2) for E_1 gives us the final equation for the energy E_1 in the M rest frame

$$E_1 = \frac{M^2 + m_1^2 - m_2^2}{2M} \quad (\text{C.1.3})$$

E_2 yields

$$E_2 = \frac{M^2 + m_2^2 - m_1^2}{2M} \quad (\text{C.1.4})$$

respectively.

The expression for $|\vec{p}_1| = |\vec{p}_2| = p$ can be obtained by using Eq. (C.1.1) and solving it for p :

$$\begin{aligned}
 \sqrt{p^2 + m_1^2} + \sqrt{p^2 + m_2^2} &= M & \Big| \uparrow^2 \\
 p^2 + m_1^2 + 2 \cdot \sqrt{(p^2 + m_1^2)(p^2 + m_2^2)} + p^2 + m_2^2 &= M^2 \\
 \sqrt{p^4 + p^2 \cdot (m_1^2 + m_2^2) + m_1^2 m_2^2} &= \frac{M^2 - m_1^2 - m_2^2 - 2p^2}{2} & \Big| \uparrow^2 \\
 & \vdots \\
 \frac{M^4 - 2M^2 \cdot (m_1^2 + m_2^2) - 2m_1^2 m_2^2 + m_1^4 + m_2^4}{4M^2} &= p^2 \\
 \frac{\sqrt{(M^2 - (m_1 + m_2)^2) (M^2 - (m_1 - m_2)^2)}}{2M} &= p & \text{(C.1.5)}
 \end{aligned}$$

C.2. Calculation Of The Complex Fit Function

The fit function from 3.2.2 has complex functions since the Υ resonances can have a coupled phase. In order to obtain real values for the fit one has to calculate the absolute value of the fit function, which can be done by separating the equation into real and imaginary part.

$$\begin{aligned}
 f = |A_{nr}|^2 + \xi^2 &= \left| A_{nr} \right|^2 + \left| A_0 + A_{\Upsilon 4S} \exp [i\phi_{\Upsilon 4S}] \cdot \frac{1}{(E^2 - \mu_{\Upsilon 4S}^2) + i\mu_{\Upsilon 4S} \Gamma_{\Upsilon 4S}} \right. \\
 & \quad + A_{\Upsilon 5S} \exp [i\phi_{\Upsilon 5S}] \cdot \frac{1}{(E^2 - \mu_{\Upsilon 5S}^2) + i\mu_{\Upsilon 5S} \Gamma_{\Upsilon 5S}} \\
 & \quad \left. + A_{\Upsilon 6S} \exp [i\phi_{\Upsilon 6S}] \cdot \frac{1}{(E^2 - \mu_{\Upsilon 6S}^2) + i\mu_{\Upsilon 6S} \Gamma_{\Upsilon 6S}} \right|^2 & \text{(C.2.1)}
 \end{aligned}$$

Since $\exp [i\phi] = \cos \phi + i \sin \phi$ it follows

$$\begin{aligned}
 \xi_{\text{real}} &= A_0 + \frac{A_{\Upsilon 4S} \left(\cos \phi_{\Upsilon 4S} \cdot (E^2 - \mu_{\Upsilon 4S}^2) + \sin \phi_{\Upsilon 4S} \cdot \mu_{\Upsilon 4S} \Gamma_{\Upsilon 4S} \right)}{(E^2 - \mu_{\Upsilon 4S}^2)^2 + \mu_{\Upsilon 4S}^2 \Gamma_{\Upsilon 4S}^2} \\
 & \quad + \frac{A_{\Upsilon 5S} \left(\cos \phi_{\Upsilon 5S} \cdot (E^2 - \mu_{\Upsilon 5S}^2) + \sin \phi_{\Upsilon 5S} \cdot \mu_{\Upsilon 5S} \Gamma_{\Upsilon 5S} \right)}{(E^2 - \mu_{\Upsilon 5S}^2)^2 + \mu_{\Upsilon 5S}^2 \Gamma_{\Upsilon 5S}^2} \\
 & \quad + \frac{A_{\Upsilon 6S} \left(\cos \phi_{\Upsilon 6S} \cdot (E^2 - \mu_{\Upsilon 6S}^2) + \sin \phi_{\Upsilon 6S} \cdot \mu_{\Upsilon 6S} \Gamma_{\Upsilon 6S} \right)}{(E^2 - \mu_{\Upsilon 6S}^2)^2 + \mu_{\Upsilon 6S}^2 \Gamma_{\Upsilon 6S}^2} & \text{(C.2.2)}
 \end{aligned}$$

$$\xi_{\text{imaginary}} = i \cdot \left(\frac{A_{\Upsilon 4S} \left(\sin \phi_{\Upsilon 4S} \cdot (E^2 - \mu_{\Upsilon 4S}^2) - \cos \phi_{\Upsilon 4S} \cdot \mu_{\Upsilon 4S} \Gamma_{\Upsilon 4S} \right)}{(E^2 - \mu_{\Upsilon 4S}^2)^2 + \mu_{\Upsilon 4S}^2 \Gamma_{\Upsilon 4S}^2} + \frac{A_{\Upsilon 5S} \left(\sin \phi_{\Upsilon 5S} \cdot (E^2 - \mu_{\Upsilon 5S}^2) - \cos \phi_{\Upsilon 5S} \cdot \mu_{\Upsilon 5S} \Gamma_{\Upsilon 5S} \right)}{(E^2 - \mu_{\Upsilon 5S}^2)^2 + \mu_{\Upsilon 5S}^2 \Gamma_{\Upsilon 5S}^2} + \frac{A_{\Upsilon 6S} \left(\sin \phi_{\Upsilon 6S} \cdot (E^2 - \mu_{\Upsilon 6S}^2) - \cos \phi_{\Upsilon 6S} \cdot \mu_{\Upsilon 6S} \Gamma_{\Upsilon 6S} \right)}{(E^2 - \mu_{\Upsilon 6S}^2)^2 + \mu_{\Upsilon 6S}^2 \Gamma_{\Upsilon 6S}^2} \right) \quad (\text{C.2.3})$$

The final value for the expression C.2.1 can be obtained by calculating

$$f = |A_{nr}|^2 + \xi^2 = \left| A_{nr} \right|^2 + \left(\xi_{\text{real}} + \xi_{\text{imaginary}} \right)^2 = |A_{nr}|^2 + \xi_{\text{real}}^2 + \xi_{\text{imaginary}} \cdot \xi_{\text{imaginary}}^* \quad (\text{C.2.4})$$

C.3. π^0 Recoilmass Background Fit Using Higher Order Polynomials

Parameter	4th order polynomial	6th order polynomial
A	45.9695	45.716
μ	10.69 GeV (fixed)	10.69 GeV (fixed)
Γ	0.006 GeV (fixed)	0.006 GeV (fixed)
p_0	$-2.02673 \cdot 10^6$	$-8.44451 \cdot 10^5$
p_1	$9.50820 \cdot 10^4$	12.7953
p_2	$1.78420 \cdot 10^4$	$4.46201 \cdot 10^3$
p_3	$8.37120 \cdot 10^2$	$5.58121 \cdot 10^2$
p_4	$-1.57001 \cdot 10^2$	39.2724
p_5	–	$7.13486 \cdot 10^{-4}$
p_6	–	$-5.7587 \cdot 10^{-1}$
χ^2	107.775	107.614

Table C.1.: Upper limit (90% C.L.) fit results for the π^0 recoilmass fit using a fourth order and a sixth order polynomial for background fitting.

Acknowledgements

The heavens declare the glory of
God; the skies proclaim the work of
his hands.

Psalm 19,1

First of all I would like to thank my Lord and savior Jesus Christ for his love and for magnifying his majesty in the beauty of the universe and its laws.

It is an honor for me to be part of the working group of Prof. Dr. Wolfgang Kühn, whom I hold in high esteem and whom I thank for the opportunity to work on such a fascinating and interesting topic.

I owe my deepest gratitude to Dr. Jens Sören Lange, who was the supervisor of this work and who had many great ideas concerning the analysis – thanks for the continuous guidance, encouragement and your support, your door was open for any question and you always had the ability to captivate me for the subject, it was a pleasure to work with you!

I would also like to express my thanks to all the members of the Kühn group especially to my co-workers Milan Wagner and Matthias Ullrich, who is not only a good friend but also helped me to get into the Belle analysis stuff. I really appreciated the time as your colleague.

I am much obliged to Dr. Alexander Theis and Julian Werner for proofreading this thesis.

Big thanks to my parents, Elfriede and Joachim Werner – without your parental support my studies and therefore this work would never have been possible.

Last, but far from least, I want to thank my beautiful wife Stefanie for always being the wind at my back - you are the living proof God blessed his daughters...

List of Figures

1.1.	Difference between QED and QCD forces	13
1.2.	One-gluon exchange s-channel diagram for $q\bar{q}$ -annihilation	17
1.3.	One-gluon exchange t-channel diagram for $q\bar{q}$ -scattering	17
1.4.	S-wave reduced radial wave functions of $b\bar{b}$ -states	23
1.5.	P-wave reduced radial wave functions of $b\bar{b}$ -states	24
1.6.	D-wave reduced radial wave functions of $b\bar{b}$ -states	24
1.7.	Theoretical predictions for $b\bar{b}$ -states in comparison with experimental data	25
1.8.	Radial densities of $b\bar{b}$ plotted together with the used Cornell potential	25
1.9.	Theoretical predictions from Breit interaction for the $c\bar{c}$ -spectrum in comparison with experimental data	30
2.1.	Typical pp event (left) compared to typical e^+e^- event (right).	35
2.2.	Configuration of the KEKB accelerator system.	37
2.3.	Bunch rotating through crab cavities in order to get head-on collisions.	38
2.4.	Schematic overview of the BELLE detector	38
2.5.	Schematic view of the SVD2 at BELLE. The four layers have the radii $r_1 = 20.0$ mm, $r_2 = 43.5$ mm, $r_3 = 70.0$ mm, $r_4 = 88.0$ mm	39
2.6.	Arrangement of the Belle aerogel cherenkov counters.	40
2.7.	Configuration of the Belle electromagnetic calorimeter	41
2.8.	Profile view of a resistive plate counter	42
3.1.	Feynman diagrams for semileptonic B/\bar{B} decays	44
3.2.	Dilepton invariant mass spectrum of the $\Upsilon(4S)$ ($\sqrt{s} = 10.5779$ GeV) data sample	45
3.3.	Dilepton invariant mass spectrum of the $\sqrt{s} = 10.8275$ GeV data sample	46

3.4. Dilepton invariant mass spectrum of the $\Upsilon(5S)$ ($\sqrt{s} = 10.871$) GeV data sample	46
3.5. Dilepton invariant mass spectrum of the $\sqrt{s} = 10.8825$ GeV data sample	47
3.6. Dilepton invariant mass spectrum of the $\sqrt{s} = 10.8975$ GeV data sample	47
3.7. Dilepton invariant mass spectrum of the $\sqrt{s} = 10.9275$ GeV data sample	48
3.8. Dilepton invariant mass spectrum of the $\sqrt{s} = 10.9575$ GeV data sample	48
3.9. Dilepton invariant mass spectrum of the $\sqrt{s} = 11.0175$ GeV data sample	49
3.10. Plot (a) shows the distribution of the lepton momenta from $\Upsilon(4S)$ data, plot (b) shows the momentum spectrum plotted against the invariant mass $m_{ll'}$ of the dilepton. The red lines indicate the edges of the momentum cuts. Plot (b) clearly points out the need for a J/ψ veto, since leptons from J/ψ decays lie directly in the allowed momentum range.	50
3.11. The plot on the left shows the asymmetric J/ψ rejection region for e^+e^- pairs, the plot on the right shows the symmetric J/ψ veto in the $\mu^+\mu^-$ channel.	50
3.12. $B - \bar{B}$ oscillation scheme	51
3.13. Plot (a) shows $(OS-SS)/(OS+SS)$ plotted in dependence of Δz before the application of the cuts, no oscillation occurs. After the application of the cuts, plot (b) reveals a significant oscillation in B/\bar{B} meson decays.	52
3.14. A linear fit to obtain the values for Ξ	54
3.15. Normalized dilepton counts as a function of \sqrt{s}	55
3.16. Zoom into the data points between $\sqrt{s} = 10.7985$ GeV and $\sqrt{s} = 11.0175$ GeV (ll' channel)	56
3.17. Zoom into the data points between $\sqrt{s} = 10.7985$ GeV and $\sqrt{s} = 11.0175$ GeV ($e\mu$ channel)	56
3.18. Fit results for the normalized dilepton signal	57
3.19. Fit results zoomed into the region between $\sqrt{s} = 10.7985$ GeV and $\sqrt{s} = 11.0175$ GeV	57
3.20. $\langle (\gamma_1, \gamma_2)_{\text{LAB}}$ from π^0 candidates, the red lines indicate the allowed angle regions	60
3.21. Distribution of the angle between the photons from π^0 candidates in the π^0 rest frame	60
3.22. Monte Carlo simulations: Low momentum π^0 distribution from K^* (upper left), ρ (lower left) and D decays (upper right). All distributions look similar. The plot on the lower right shows the primary π^0 momentum distribution from $B\bar{B}\pi^0$ events.	61
3.23. Fit of the dilepton + π^0 signals in dependence of \sqrt{s} . The complete fit is drawn in red, the dashed blue line represents the contribution from $B^{*0}\bar{B}^{*0}\pi^0$ events and the black dashed-dotted line shows the contribution from $B_s^*\bar{B}_s^*\pi^0$ production.	63

3.24. Plot (a) shows a simulation of the π^0 recoilmass distribution if there are no undiscovered states ($\Upsilon(5S) \rightarrow B^0 \bar{B}^{*0} \pi^0$). If there was a new state with mass 10.65 GeV which decays into B mesons recoiling against the π^0 , the π^0 recoilmass distribution would look like plot (b), channel $\Upsilon(5S) \rightarrow X_b \pi^0 \rightarrow B^0 \bar{B}^{*0} \pi^0$. (c) shows the distribution of the π^0 recoilmass, if the branching fraction $(\Upsilon(5S) \rightarrow X_b \pi^0)/(\Upsilon(5S) \rightarrow B^0 \bar{B}^{*0} \pi^0)$ would be 1 : 4. Even in such a dirty environment an enhancement of the count rate at the X_b mass (10.65 GeV) can be seen.	64
3.25. Correlation between $E(\pi^0)$ and $\Delta E(\pi^0)$	65
3.26. π^0 recoilmass distributions for the energy values $\sqrt{s} = 10.8275, 10.8675, 10.871$ and 10.8825 GeV	66
3.27. π^0 recoilmass distributions for the energy values $\sqrt{s} = 10.8975, 10.9275, 10.9575$ and 11.0175 GeV	67
3.28. Sum of all lumionsity weighted π^0 recoilmass distributions from Fig. 3.26 and Fig. 3.27	68
3.29. Plot (a) shows the fit of the gaussian signal plus the second order polynomial background distribution. Actually there is a nonzero signal yield, but it is not convincing and also depending on the choice of the background function. Plot (b) shows the fitted curve of the upper limit calculations. The complete fit functions are drawn in red, the black dashed lines represent the background distributions.	69
3.30. Normalized dilepton + $\pi^+ \pi^-$ counts in dependence of \sqrt{s} . As the available phase space is increasing with \sqrt{s} , the probability that low energy pion pairs are measured accurately enough is increasing.	72
A.1. Lepton momenta from J/ψ decays in dependence of \sqrt{s} , $\sqrt{s} = 10.5779$ GeV to $\sqrt{s} = 10.8525$ GeV	79
A.2. Lepton momenta from J/ψ decays in dependence of \sqrt{s} , $\sqrt{s} = 10.8525$ GeV to $\sqrt{s} = 10.8975$ GeV	80
A.3. Lepton momenta from J/ψ decays in dependence of \sqrt{s} , $\sqrt{s} = 10.9275$ GeV to $\sqrt{s} = 11.0175$ GeV	81
A.4. $ \vec{p}_{\text{cms}} $ spectra of lepton l_1 (left) and lepton l_2 (right) from semileptonic $B^0 \bar{B}^0$ decays at $\sqrt{s} = 10.5779$ GeV	82
A.5. $ \vec{p}_{\text{cms}} $ spectra of lepton l_1 (left) and lepton l_2 (right) from semileptonic $B^0 \bar{B}^0$ decays at $\sqrt{s} = 10.7985$ GeV	82
A.6. $ \vec{p}_{\text{cms}} $ spectra of lepton l_1 (left) and lepton l_2 (right) from semileptonic $B^0 \bar{B}^0$ decays at $\sqrt{s} = 10.871$ GeV	83
A.7. $ \vec{p}_{\text{cms}} $ spectra of lepton l_1 (left) and lepton l_2 (right) from semileptonic $B^0 \bar{B}^0$ decays at $\sqrt{s} = 10.9575$ GeV	83

A.8. $|\vec{p}_{\text{cms}}|$ spectra of lepton l_1 (left) and lepton l_2 (right) from semileptonic
 $B^0\bar{B}^0$ decays at $\sqrt{s} = 11.0175$ GeV 84

List of Tables

1.1.	Fundamental fermions in the SM	12
1.2.	Spin-orbit coupling for $l \neq 0$ and $S = 1$	20
1.3.	Non-vanishing diagonal elements of S_{12}	21
1.4.	$b\bar{b}$ -states from theory and experiment in comparison	26
1.5.	Overview of important masses concerning the $X(3872)$ [15]	28
1.6.	Quantum numbers of the charmonium states, which are possible candidates for the $X(3872)$	29
1.7.	Possible weakly-bound states of charmed mesons coming from an one-pion exchange potential	31
3.1.	MC results for the correction factor Ξ	53
3.2.	Final values for the correction factor Ξ	54
3.3.	Fit results and parameter constraints	58
3.4.	Comparison of the obtained $\Upsilon(5S)$ fit results with measurements from BaBar and with the value from the particle data group	58
3.5.	Constraints of the π^0 momenta due to limited phase space.	60
3.6.	Fit results from the fit in Fig. 3.23.	62
3.7.	Fit results for the π^0 recoilmass distribution from the large $\Upsilon(5S)$ data sample	69
3.8.	Upper limits on the energy of the $\pi^+\pi^-$ pair created in $B\bar{B}^*\pi^+\pi^-$ events.	71
A.1.	Monte Carlo efficiencies of the lepton momentum cuts from semileptonic B^0 (B_s^0) decays in dependence of different $\Upsilon(5S)$ decay channels. A significant efficiency dependence on the $\Upsilon(5S)$ decay channel cannot be seen. BELLE detector acceptance and particle identification efficiency is included.	78

A.2. Monte Carlo results based on 40000 simulated $B^0\bar{B}^0$ pairs, which decay semileptonically.	84
B.1. Data used for the analysis and the integrated luminosity for each data point	85
C.1. Upper limit (90% C.L.) fit results for the π^0 recoilmass fit using a fourth order and a sixth order polynomial for background fitting.	88

Bibliography

- [1] J.J. Aubert et al., *EXPERIMENTAL OBSERVATION OF A HEAVY PARTICLE J*, Phys. Rev. Lett. **33** (1974), 1404-1406
- [2] J.E. Augustin et al., *DISCOVERY OF A NARROW RESONANCE IN e^+e^- ANNIHILATION*, Phys. Rev. Lett. **33**(1974), 1406-1408
- [3] S.W. Herb et al., *Observation of a dimuon resonance at 9.5-GeV in 400-GeV proton-nucleus collisions*, Phys. Rev. Lett. **30** (1973), 1343-1346
- [4] The Big Bang Theory, *The Big Bran Hypothesis*, Episode 1, Series 2 (2008)
- [5] Richard Feynman, *Feynman lectures III*, chapter 16-5
- [6] J. Eiglsperger, *Quarkonium Spectroscopy: Beyond One-Gluon Exchange*, Diploma Thesis, January 2007, arxiv:0707.1269v1
- [7] Gregory Breit, *The effect of retardation on the interaction of two electrons*, Physical Review **34** (1929), 553
- [8] Gregory Breit, *The fine structure of He as a test of the spin interactions of two electrons*, Physical Review **36** (1930), 383
- [9] Gregory Breit, *Dirac's equation and the spin-spin interactions of two electrons*, Physical Review **39** (1932), 616
- [10] M. Werner, *Heavy Quarkonium Spectroscopy: Schroedinger Equation For Charmonium And Bottomonium Eigenstates*, Workout for Module MP-28 C (2009)
- [11] S. K. Choi et al. , *Observation of a narrow charmonium-like state in exclusive $B^+ \rightarrow K^+\pi^+\pi^- J/\psi$ decays*, Phys. Rev. Lett. **91**, 262001 (2003), hep-ex/0309032

-
- [12] D. Acosta et al., *Observation of the Narrow State $X(3872) \rightarrow J/\psi \pi^+\pi^-$ in $\bar{p}p$ Collisions at $\sqrt{s} = 1.96 \text{ TeV}$* , Phys. Rev. Lett. **93**, 072001 (2004), hep-ex/0312021
- [13] V. M. Abazov, *Observation and Properties of the $X(3872)$ Decaying to $J/\psi \pi^+\pi^-$ in $p\bar{p}$ Collisions at $\sqrt{s} = 1.96 \text{ TeV}$* , Phys. Rev. Lett. **93**, 162002 (2004), hep-ex/0405004
- [14] B. Aubert et al., *Study of the $B^- \rightarrow J/\psi K^- \pi^+ \pi^-$ Decay and Measurement of the $B^- \rightarrow X(3872) K^-$ Branching Fraction*, Phys. Rev. **D71**, 071103 (2005), hep-ex/0406022
- [15] C. Amsler et al., *Physics Letters B* **667**, 1 (2008)
- [16] K. Abe et al., *Evidence for $X(3872) \rightarrow \gamma J/\psi$ and the sub-threshold decay $X(3872) \rightarrow \omega J/\psi$* , (2005), hep-ex/0505037
- [17] K. Abe et al., *Experimental constraints on the possible J^{PC} quantum numbers of the $X(3872)$* , (2005), hep-ex/0505038
- [18] Belle, S. L. Olsen, Int. J. Mod. Phys. **A20**, 240 (2005), hep-ex/0407033
- [19] T. Barnes and S. Godfrey, Phys. Rev. **D69**, 054008 (2004), hep-ph/0311162
- [20] E. K. Eichten, K. Lane, C. Quigg, Phys. Rev. **D69**, 094019 (2004), hep-ph/0401210
- [21] M. Kusunoki, *Charm Meson Molecules and the $X(3872)$* , Dissertation, Ohio State University (2005)
- [22] N. A. Tornqvist, *Isospin breaking of the narrow charmonium state of Belle at 3872 MeV as a deuson*, Z. Phys. **C61**, 525 (1994), hep-ph/0402237
- [23] E. S. Swanson, *Short Range Structure in the $X(3872)$* , Phys. Lett. **B588**, 198 (2004), hep-ph/0311229
- [24] E. Braaten, M. Kusunoki, *Low-energy Universality and the New Charmonium Resonance at 3870 MeV*, Phys. Rev. **D69**, 074005 (2004), hep-ph/0311147
- [25] E. Braaten, H. W. Hammer, *Universality in Few-body Systems with Large Scattering Length*, (2004) cond-mat/0410417
- [26] F. E. Close, S. Godfrey, *Charmonium Hybrid Production in Exclusive B Meson Decays*, Phys. Lett. **B574**, 210 (2003), hep-ph/0305285
- [27] B. A. Li, *Is $X(3872)$ a possible candidate of hybrid meson*, Phys. Lett. **B605**, 306 (2005), hep-ph/0410264

- [28] K. K. Seth, *An Alternative Interpretation of $X(3872)$* , Phys. Lett. **B612**, 1 (2005), hep-ph/0411122
- [29] J. Vijande, F. Fernandez, A. Valcarce, *Describing non- $q\bar{q}$ candidates*, Int. J. Mod. Phys. **A20**, 702 (2005), hep-ph/0407136
- [30] L. Maiani, F. Piccinini, A. D. Polosa, V. Riquer, *Diquark-Antidiquarks with Hidden or Open Charm and the Nature of $X(3872)$* , Phys. Rev. **D71**, 014028 (2005), hep-ph/0412098
- [31] W.S. Hou, *Searching for the bottom counterparts of $X(3872)$ and $Y(4260)$ via $\pi^+\pi^-\Upsilon$* , Phys. Rev. D **64**, 017504 (2006)
- [32] The Big Bang Theory, *The Pork Chop Indeterminacy*, Episode 15, Series 1 (2008)
- [33] S. Kurokawa, E. Kikutani, *Overview of the KEKB Accelerators*, Nucl. Inst. Meth. **A**, **499**(1):1-7 (2003)
- [34] K. Akai et al., *Commissioning of KEKB*, Nucl. Inst. Meth. **A**, **499**(1):192-227 (2003)
- [35] The Big Bang Theory, *The Griffin Equivalency*, Episode 4, Series 2 (2008)
- [36] C. Kiesling, *QED Background Event Generators*, DEPFET-PXD Meeting, Prague, Jan. 25-27, 2010
- [37] N. Hastings, *Neutral B meson mixing and CPT violation with the Belle Experiment*, PhD Thesis, University of Melbourne, September 2002
- [38] B. Aubert et al., *Measurement of the $e^+e^- \rightarrow b\bar{b}$ Cross Section between $\sqrt{s} = 10.54$ and 11.20 GeV*, Phys. Rev. Lett. **102**, 012001 (2009)
- [39] C. Y. Lin, *Relative π^0 efficiency using $D^0 \rightarrow K\pi$ and $D^0 \rightarrow K\pi\pi^0$* , Belle Note #916, 2006
- [40] A. Drutskoy et al., *Measurement of $\Upsilon(5S)$ decays to B^0 and B^+ mesons*, Phys. Rev. D **81**, 112003 (2010)
- [41] R. Louvot et al., *Measurement of the Decays $B_s^0 \rightarrow D_s^- \pi^+$ and Evidence for $B_s^0 \rightarrow D_s^\pm K^\pm$ in e^+e^- Annihilation at $\sqrt{s} \approx 10.87$ GeV*, Phys. Rev. Lett. **102** 021801 (2009)
- [42] B. Aubert et al. *Study of resonances in exclusive B decays to $\bar{D}^{(*)}D^{(*)}K$* , Phys. Rev. D **77**, 011102(R) (2008)
- [43] I.F. Albuquerque et al., *New upper limit for the branching ratio of the $\Omega^- \rightarrow \Xi^- \gamma$ radiative decay*, Phys. Rev. **D50** 18-20 (1994) hep-ph/9404340v1

- [44] A. Schwartz, *CKM'06, Belle physics results at the $\Upsilon(5S)$* , Nagoya Daigaku (2006), <http://belle.kek.jp/belle/talks/CKM06/Schwartz.pdf>

Eidesstattliche Versicherung

Hiermit versichere ich, dass ich die vorliegende Arbeit selbstständig und ohne unerlaubte Hilfe angefertigt habe. Außer der angegebenen Literatur habe ich keine weiteren Hilfsmittel verwendet.

Gießen,

Marcel Werner